TAMPEREEN TEKNILLINEN YLIOPISTO
TAMPERE UNIVERSITY OF TECHNOLOGY

JONAS BARTH

INTRINSIC STRESS IN THIN METALLIC MULTILAYERS

Master of Science Thesis

Examiner: Prof. Dr. Petri Vuoristo
Supervisor: Dr. Arnd Müller

Examiner and topic approved
by the Council of the Faculty
of Engineering Sciences on
26th April 2017

ABSTRACT

JONAS BARTH: Intrinsic Stress in Thin Metallic Multilayers
Tampere University of Technology
Master of Science Thesis, 91 pages, 12 Appendix pages
February 2018
Master's Degree Programme in Material Science
Major: Metallic and Ceramic materials
Examiner: Professor Dr. Petri Vuoristo

Keywords: Magnetron Sputtering, Chromium, Zirconium, Residual Stress, Substrate Curvature, X-ray Diffraction, Thin Film, sin2ψ,

The ePD™ process (embedded PVD for Design Parts) by Oerlikon Balzers combines a magnetron sputtering metallization process with a UV (Ultraviolet) lacquer painting, to replace electroplating as a metallization process for decorative interiors and exterior car parts. Since most sputtered films exhibit residual stress, understanding the origin of this stress is very important. High residual stresses in the ePD™ systems can have a detrimental effect on its appearance due to the emergence of cracks, as well as on the loss of adhesion to the substrate.

In this thesis the residual stress and film structure of chromium (Cr) and zirconium (Zr) are studied as a function of (1) sputtering time, (2) target current, (3) sputtering pressure, (4) substrate rotation and (5) interrupted deposition. Additionally, existing models are tested which allow to predict the residual stress and therefore to deposit a stress designed layer stack. Lastly, the connection of UV lacquer thickness and residual stress is investigated.

Glass substrates have been coated in a research batch coater and afterward analyzed. The residual stress was determined by means of substrate curvature method as well as by X-ray diffraction (XRD). The latter was also used to evaluate the phase, texture and crystalline size. The development of the film surface morphology and film structure was investigated with the scanning electron microscope (SEM). Finally, Young's modulus and hardness of the PVD films were determined.

The experiments revealed a strong connection of residual stress, texture, phase, surface morphology and film structure with the thickness of both materials. Tensile stress was observed for Cr, which also showed a rotationally random oriented (110)-out of plane fiber texture for thinner films and a single crystal-like structure for thicker films. Zirconium, always exhibiting compressive stress, showed an amorphous structure for the thin films which changes to a more crystalline structure with an increasing film thickness or by increasing the sputtering pressure. Raising the target power lead to an increase in tensile stress for Cr and an increase in compressive stress for Zr. Increasing the sputtering pressure decreased the tensile stress in Cr and increased the compressive stress for Zr. The interruption of the deposition process caused a change in the observed stress for only the thick Zr films. The existing theoretical models were able to explain the observed results and allowed to predict the overall residual stress in a Cr-Zr-Cr layer stack.

The results suggest that it is possible to tailor and predict the residual stresses in PVD single films and layer stacks if the connection between process parameters and film structure evolution as well as the stress generating mechanism are known.

PREFACE

This Master Thesis was carried out in between June 2017 and January 2018 at the Analytic Laboratory of the Oerlikon Surface Solutions AG in the Principality of Liechtenstein.

I would like first to thank Dr. Arnd Müller to whom I am deeply grateful for facilitating this Master Thesis. His continued support, encouragement, readiness to discuss and his valuable advice during the course of the thesis work contributed considerably to the success of this Master Thesis.

I am also grateful to Professor Petri Vuoristo to give me the opportunity to pursue this thesis topic and to advise me during the thesis work.

Dr. Ievlev Dmitrij deserves my special gratitude for his assistance to define suitable process parameters for my research. I also want to thank Mr. Mathias Maier for helping me to get started with the sample preparations and for designing the sample holders. Dr. Kumar Yalamanchili and Dr. Doris Fopp-Spori are greatly acknowledged for their interests and lively discussions about my research.

Mr. Klaus Hippedinger deserves my special thanks for helping me with designing and building the fixtures for my samples, quite often even on a very short notice during the experimental phase.

To the staff and colleagues at the Balzers R&D Analytics Department, I would like to express my special appreciation for the help with getting all the training at the measurement devices and for the amazing work environment, in which it has been a great pleasure to carry out this thesis work.

Finally, I wish to thank my family, friends and fellow students for their support during my studies.

Tampere, 19.02.2018

Jonas Barth

CONTENTS

LIST OF TABLES

LIST OF SYMBOLS AND ABBREVIATIONS

Symbol	Meaning	Unit
<σ>	Average Stress	[MPa]
1/2s2	X-Ray Elastic Constant	[MPa^{-1}]
B	Constant for describing deformation in relation to film thickness	[-]
A	Constant for describing deformation in relation to film thickness	[-]
ABS	Acrylonitrile Butadiene Styrene	[-]
A_P	Projected contact area between the Indenter and the measured material	[mm^2]
$\vec{B}$	Magnetic Field	[N/Am]
BC	Basecoat	[-]
bcc	Body centered cubic	[-]
Cr	Chromium	[-]
$Cr6^+$	Hexavalent chromium, Chromium(VI)	[-]
CTE	Coefficient of thermal expansion	[10^{-6}/K]
D_s	Diameter of the substrate	[mm]
D	Crystalline size in the Scherrer equation	[nm]
d_0	Inter-planar spacing of an unstrained lattice	[Å]
DC	Direct current	[-]
d_{hkl}	Plane spacing of the lattice plane with the Miller index hkl	[Å]
d_n	Inter-planar spacing of an unstrained lattice	[Å]
d_ψ	Inter-planar spacing in measured at tilting angle ψ	[Å]
$\vec{E}$	Electric field vector	[V/m]
E	Young's modulus, Elastic modulus	[GPa]
ECHA	European Chemicals Agency	[-]
E_{FD}	Elastic Modulus obtained by Substarte corretion via Filmdoctor Software	[GPa]
E_{IT}	Indentation modulus	[GPa]
E_{OP}	Elastic Modulus obtained by classic Oliver& Pharr Method	[GPa]
ePD™	embedded PVD Design, by Oerlikon Balzers	[-]
eV	Electron Volt	[-]
f	Interface stress	[MPa]
F/w	Force per unit width	[N/m]
fcc	Face centered cubic	[-]
F_F	Force exerted by the film	[N]

F_S	Force exerted by the substarte	[N]
FWHM	Full Width at Half Maximum	[deg]
GBR	Grain boundary relaxation model	[-]
GPa	Gigapascal	[N/mm^2]
hcp	Hexagonal closed packed	[-]
H_{FD}	Hardness obtained by substrate correction via Filmdoctor Software	[GPa]
H_{IT}	Indentation hardness	[GPa]
H_{OP}	Hardness obtained by classic Oliver & Pharr method	[GPa]
hs	Thickness of substrate in the Stoney equation	[m]
G	Shape Factor in Scherrer Equation	[-]
k	Substrate bending stiffness in the Stoney equation	[-]
MFP	Mean free path	[mm]
m	Slope of a linear plot	[-]
ML	Multilayer	[-]
MS	Microsope slide	[-]
M	Moment in a film/substrate stack	Nm
MPa	Megapascal	[N/mm^2]
n	Number of layers in a multilayer / layer stack	[-]
N	Number of interfaces	[-]
NCL	Nanostructured compliance layer	[-]
OEM	Original Equipment Manufacturer	[-]
PA	Polyamide	[-]
PDF	Powder Diffraction File	[-]
PBT	Polybutylene terephthalate	[-]
PC	Polycarbonate	[-]
PEI	Polyetherimide	[-]
P_{max}	Maximum testing load during Indentation testing	[N]
PS	Polystyrene	[-]
PVD	Physical Vapor Deposition	[-]
R	Radius of curvature in the Stoney equation	[m]
REACH	Registration, Evaluation, Authorisation and Restriction of Chemicals	[-]
s1	X-Ray elastic constant	[MPa^{-1}]
SEM	Scanning electron microscope	[-]
SMS	Stress measurement sample	[-]
SVHC	Substances of very high concern	[-]
SZD	Structure zone diagram	[-]
T	Temperature	[°C]
t_p	Used penetration depth for calcualting A_P	[µm]
t_f	Film thickness	[nm]
t_s	Thickness of Substrate in the Stoney Equation	[m]
t_c	Critical film thickness	[nm]
TC	Topcoat	[-]

T_{dep}	Deposition temperature	[°C]
t_f	Film thickness	[nm]
t_i	Thickness of an individual layer in a Multilayer system	[nm]
T_m	Melting Temperatur of the element	[°C]
t_{max}	Maximum penetration depth during indentation testing	[µm]
UV	Ultraviolet	[-]
XEC	X-Ray elastic constant	[-]
XRD	X-ray Diffraction	[-]
α_F	Coefficient thermal expansion of the film	10^{-6}/K
α_S	Coefficient thermal expansion of the substrate	10^{-6}/K
α_R	Radial pole figure angle	[deg]
α	Meassuring angle in grazing incidence setup	[deg]
β_s	Instrumental Influence on peak broadening in Scherrer Equation	[deg]
β	Azimuthal pole figure angle	[deg]
χ	Tilting angle Chi for the texture measurement	[deg]
φ	Rotation angle Phi for the texture measurement	[deg]
γ	Grazing incidence angle	[deg]
Δh	Substratedeformation in the Stoney equation	[µm]
ψ	Titling angle Psi on the Eulerian cradle	[MPa]
$\varepsilon(\Psi,\varphi)$	Strain in realtion to the tilting angles Ψ and φ	%
θ	Diffraction angle	[deg]
λ	Wavelength	[Å]
$\sigma_{1,2,...n}$	Stress in a whole mulitlayer system	[MPa]
σ_I	Intrinsic stress	[MPa]
σ^I	Residual stresses of type one	[MPa]
σ_i	Stress in a monolayer	[MPa]
σ^{II}	Residual stresses of type two	[MPa]
σ^{III}	Residual stresses of type three	[MPa]
σ_R	Residual stress	[MPa]
σ_T	Thermal stress	[MPa]
σ_z	Stress in the z-direction of the film	[MPa]
σf	Stress in the film by the Stoney equation	[MPa]
σ_ϕ	Stress in relation to rotation angle φ	[deg]
ν_E	Poisson ratio of the indenter	[-]
νs	Poisson ratio of the substrate	[-]
ν	Poisson ratio	[-]
Zr	Zirconium	[-]

1. INTRODUCTION

Decorative electroplated coatings on polymer substrates have been used in the automotive, home appliance as well as home interior decoration sector for several decades [1][2]. However, due to an increasing environmental awareness, there has been a step away from electroplating, which uses hexavalent chromium ($Cr6^{+}$) containing chrome baths, to less harmful and environmentally friendly alternatives. One of such alternative process, which is already in use for more than 20 years, is a combination of an UV-curable (Ultraviolet) coating with a PVD (Physical Vapor Deposition) metallization process [3]. The drawback of this method was so far the difference of appearance as well as the durability compared to conventional electroplated products. Recent development of UV-coatings however has led to the emergence of several UV/PVD coating systems by numerous manufacturers [2][3].

One of the main advantages of a PVD metallization over chrome plating is its environmental friendliness. The waste disposal of chrome plating lines, including the rinsing water, is heavily regulated due to its hazardous waste character and therefore high caution must be taken during the disposal process [3]. The REACH regulation (Registration, Evaluation, Authorisation and Restriction of Chemicals), which is managed by the European Chemicals Agency (ECHA) in Helsinki, demands a substitution of dangerous chemicals, named substances of very high concern (SVHC), when less harmful alternatives are available. Hexavalent chromium, which is proven to be a human carcinogen, is one of those dangerous chemicals [4][5]. A replacement of the chrome plating process for decorative application by the UV/PVD process is possible and offers additional advantages.

First of all the complex layer system, that is required for good adhesion and durability of the electroplated chrome, can take up to several hours of deposition time [3]. Contrary to this stands the UV/PVD process which allows process times down to 15 minutes [3][6]. This allows for large throughput, which is of high interest in the automotive industry. In the interior usage, features such as capacitive sensing, light transparency as well as laser etching for light emitting buttons, which allow for a Day/Night Design are mentionable advantages for the PVD metallization. In the exterior application the enhanced corrosion resistance, even against highly corrosive salts, and radar transparency, which can be utilized for driving assistant sensor or autonomous driving, is an advantage over conventional chrome plated parts [3][6]. Overall, the UV/PVD process allows coating a larger variety of plastics substrates due to the low temperature process. Possible substrates include acrylonitrile butadiene styrene (ABS) with polycarbonate (PC) blends, polyamide (PA), polyetherimide (PEI), polybutyleneterephthalate (PBT),

polystyrene (PS) and several others, whereas chrome plating is mainly applicable for ABS [1][5].

The drawback of the fast process cycles, which reduce the costs, is however that the chrome needs to be deposited at a high deposition rate, which can result in the cracking of the coating due to the brittle nature of chrome [1]. Those micro cracks can cause "dull colours" and are most probably a result of residual stress in the film/coating system. Another problem is that the stress affects the adhesion of the coating system [7].

Market research predicts a growth trend from currently $91*10^6$ m^2 of plated plastic to $142*10^6$ m^2 in 2023 [8]. Therefore, understanding the mechanism which causes adhesion and cracking problems in the UV/PVD system and preventing those are crucial to pass the tough OEM (Original Equipment Manufacturer) requirements and keep up with this predicted market demand [3].

So far, the research pays great attention to the right formulation of the UV base and topcoat for UV/PVD systems to compensate for stresses originating from the PVD film. Smaller attention is given to the investigation and control of the stress in the PVD film and how it affects the overall stress in this system [3][9]. The typical reported values for residual stress in UV coatings and lacquers are in the range of 3-10 MPa [10][11] whereas for chromium PVD coatings the reported residual stress can be around several GPa [12][13].This suggests a stronger influence of the stress in the PVD coating than the stress of the UV lacquerer on the overall coating system.

The target of this study are ePD™ Technology (ePD=embedded PVD Design, by Oerlikon Balzers) films. Here, thin metallic PVD layers are embedded in between an organic basecoat (BC) and topcoat (TC). A comparison of the ePD™ system to a conventional chrome plating system can be seen in Figure 1.

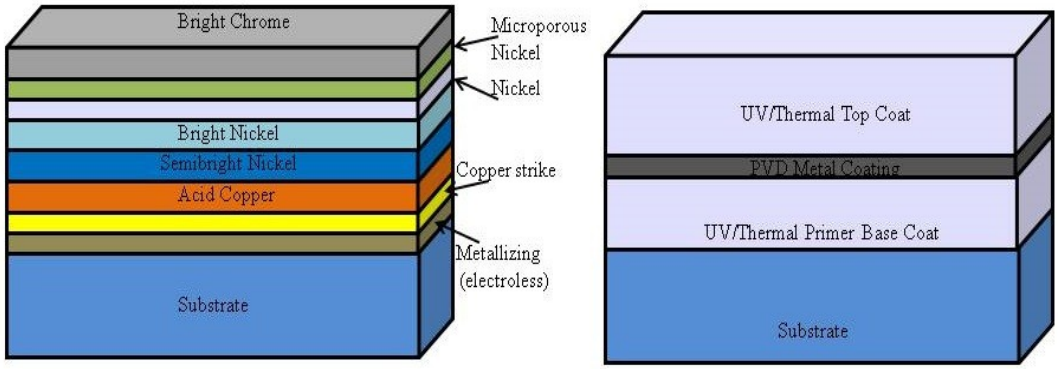

Figure 1. *Structure of a chrome plating system(left) in comparison to a possible ePD™ system(right). Adapted from* [14]

The whole ePD™ Process consists of several steps as can be seen in Figure 2. After loading the substrate holder, the parts are cleaned by a CO_2 cleaning process. This is followed by a spray painting process which applies a basecoat with a thickness of around 20 µm. This basecoat allows for a smoothening of the substrate surface irregularities, which often stem from the injection moulding process [9]. After painting, the lacquer is cured via a UV-curing process. In the following step, a metal or a metal-ceramic PVD coating is applied by a DC Magnetron (DC=Direct Current) sputtering process. After the PVD coating step follows another spray painting step to apply the topcoat and an additional UV-curing step before the parts are finished. The cycle time of the single process steps can be under 45 seconds [6].

Figure 2. *Process steps for the ePD™ process. The PVD step, as part of investigation in this thesis is highlighted in red.*[6]

This study focuses on investigating the influence of various deposition parameters on the film microstructure, surface morphology and phase, with a primary focus on the development of the residual stress in single Cr and Zr PVD layer. To do this, an XRD method and a substrate bending methods for measuring stress need to be established first and require a short examination for their feasibility and reliability. With the obtained results from the conducted parameter trails, it will be checked if the stress in the PVD films can be predicted with the available understandings and models. As a final step concerning the PVD layers, it will be checked if it is possible to design stress the by combining Cr and Zr in a layer stack. The intention of using glass substrate is to be able to isolate any substrate structure effects on the growth of the film to purely focus on effect of the process parameters on the properties. Additionally, the stress of both UV lacquers will be measured in relation to the lacquer thickness.

The thesis starts with the theoretical aspects of the PVD process as well as a short review of the UV coating process. Then the theory about how residual stresses are developed in those coating systems and ways to control them are reviewed. This is followed by the theory about the used testing methods and the actually used setup of the experiments and measurements. Finally, the obtained results are presented and discussed separately. At the end, a conclusion from the research is drawn and possible further research is suggested.

2. THEORETICAL BACKGROUND

The following chapter provides a brief introduction of the general physical and technical aspects of the sputtering as well as the UV lacquer coating process. This is followed by an explanation of residual stresses and how different process parameters influence structure and the stress in the PVD films. The chapter is finished with a short explanation of the used measuring techniques.

2.1 Deposition of thin films by sputtering

A sputtering deposition process is a form of Physical Vapor Deposition during which particles from the target are vaporized ("sputtered") by a physical sputtering process. This process is non-thermal and the target surface atoms are only ejected by a momentum transfer from the incoming working gas ions. The energetic working gas ions originate from the plasma, which is formed by noble gases such as argon or xenon. The sputtering can be done in a low-pressure plasma environment (< 7.0 x 10^{-3} mbar), where the sputtered particles only collide with some or no working gas particle on the way from the target to the substrate. This process can also be carried out in a high plasma pressure environment (7.0 x 10^{-3} mbar – 4.0 x 10^{-2} mbar). Here the particles can be thermalized by the working gas particles on the way to the substrate. The used plasma either occupies the room in between the target and the substrate surface or is confined near the target.[15]

The sputtering process allows deposition of elements, alloys or compounds. A benefit of sputtering over evaporation is that the material in the vaporized states still exhibits the same composition as the target material. Using reactive gas, which is activated by the plasma, allows for deposition of compound materials such as oxides, carbides and nitrides.[15]

The sputtering process can be divided into 3 main phases:

1. In the first phase, sputter gas ions from the plasma eject atoms from the target due to their high kinetic energy upon impact. Those sputtered target atoms usually exhibit energy between 10-40 eV, which is higher than the energy of a conventional evaporation deposition process. The sputtering yield of the target can be influenced by either using higher energy ions for sputtering or using ions with a difference mass for example, xenon instead of argon ions.[16]

2. During the transportation phase, the emitted ions and atoms from the target surface will be transported through the chamber to the substrate. During this phase, the ionized and neutral particles collide with the particles of the working gas or with the chamber walls. In both cases, the kinetic energy of the atoms and ions will be degraded. The emitted electrons from the target also collide with the working gas particles, which leads to ionization of those particles and eventually to the formation of a plasma. The amount of those collisions increases with the chamber pressure and therefore with the quantity of gas particles. This relationship can be described with the mean free path (MFP).[16]

3. The last step includes the condensation of the particles on the substrate surface and the resulting formation of the film. Some of the adsorbed atoms (adatoms) form nuclei, from which subsequently the formation of crystalline starts. Those crystalline form small islands. Those islands eventually grow together and form the film. This island growth mode is also called Vollmer-Weber growth mode and is characterized by the fact that the island boundaries represent barriers for the diffusing atoms. This leads to a growth mode of high islands after the substrate surface is covered with some initial monolayer. The formation of the film structure and the grain size depends on the homologous temperature (quotient of Substrate temperature and melting point of coating material in Kelvin) and the kinetic energy of the incident species [17]. The kinetic energy can be tuned by substrate bias or the working gas pressure. The latter dependence is visualized by the structure zone diagram (SZD) from Thornton. A more detailed discussion on how the parameters influence the film structure and the film properties can be found in chapter 2.4. [16][17]

2.2 Deposition of thin films by magnetron sputtering

The difference from magnetron sputtering to conventional sputtering methods is that a large volume of plasma is confined next to the target surface by utilizing a strong magnetic field. The DC magnetron produces an electric ($\vec{E}$, vector) and magnetic ($\vec{B}$, vector) field which influences the trajectory of the secondary electrons emitted from the target surface upon bombardment by argon ions. If the magnetic field lines are closed, electrons with a velocity component perpendicular to the field lines will be bend in a spiral-like trajectory close to the surface. This increases the ionization probability of the working gas and hence the plasma density in the target surface region, even at a lower working gas pressures. Advantages of the confined plasma are an increase in the deposition rate, a reduction of substrate and chamber wall sputtering as well as a reduction in substrate heating [15][18].
On the other hand, the non-uniformity of the magnetic field lines leads to a non-uniform plasma distribution over the target surface. This results in an uneven sputtering of the target and erosion in a “racetrack” like fashion, which results in a bad utilization of the

target material. Furthermore, the atom density of the sputtered material shows a circular distribution over the target surface. [15][18][19] To increase the uniformity of the plasma, several magnet arrangements and target geometries are available.[18]

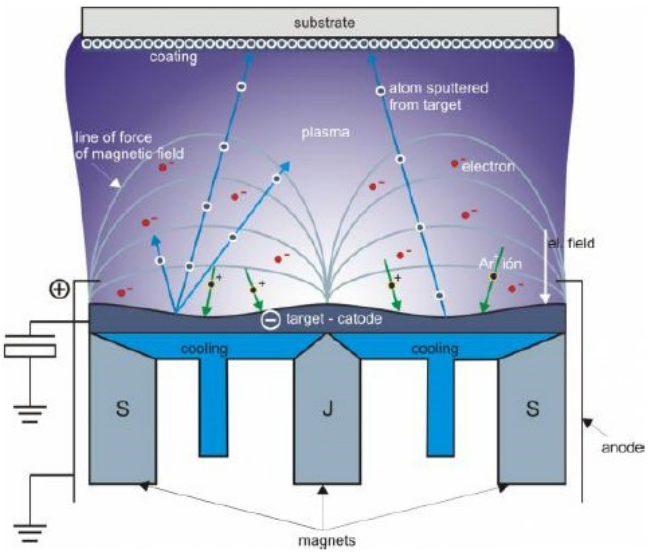

Figure 3. *Schematic representation of the working principle of a DC magnetron sputtering system. Also included are the magnetic field lines and the argon ions and electron involved in the sputtering process* [20]

2.3 UV coating

The polymer substrates which are metallized by the PVD process are often produced by a high volumes injection moulding process. Unless the moulding form possesses a high-quality polished surface finish, a smoothening of the substrate surface is needed to achieve an ornate and lustrous surface appearance [9]. To provide such a smooth and continuous surface for the PVD coating, a basecoat is applied to even out the surface and help to achieve the desired brightness of the metallization [3][9]. To protect the metallic PVD film a UV curable topcoat is applied, which also allows for adjusting the appearance between a satin and low gloss finish [2].

2.3.1 Deposition and curing of UV coatings

Typical processes to apply UV coatings are either by a flow or spray-coat process. Here, the parts are either carried by a conveyor belt system through a constant flow of paint in the first setup or painted directly with a spray gun. This spray gun in the spray-coat process can be carried by a skilled human worker or by a programmable industrial robot.

After the coating is applied, the solvent is usually evaporated by a mix of infrared and hot air in the so-called “flash off” step. This results in a solid coating which is dry to the

touch. However to fully develop its mechanical properties, the lacquer needs to undergo a polymerization process to fully crosslink and form a dense film. This is achieved by a final curing step using UV light. A schematic drawing of those steps is shown in the picture below. Typical UV sources are mercury-vapour lamps which emit the light to the surface. Using a rather complex mirror and reflector system allows curing the lacquer on complexly shaped surfaces.[21]

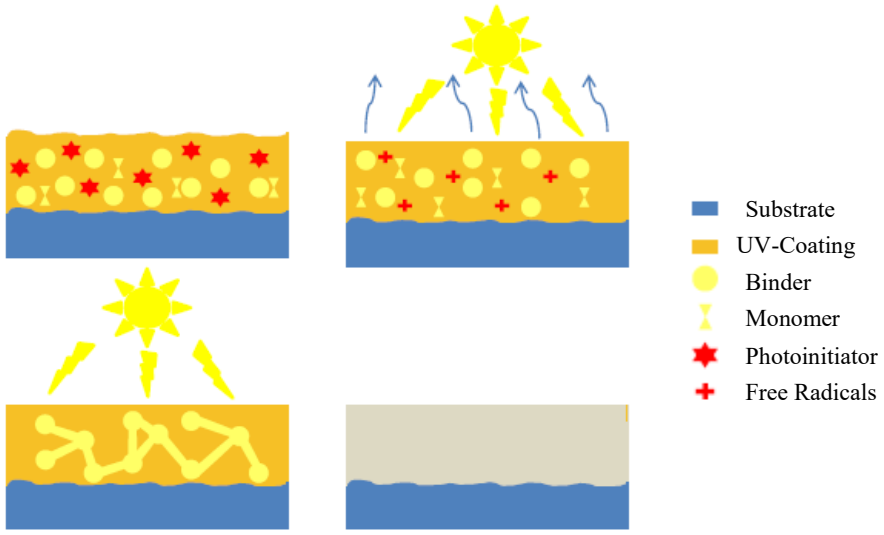

Figure 4. *Schematic representation of the curing process of UV coatings, from top left to bottom left the steps are: 1. Wet coating after spray application. 2. Flash off by hot air and IR. 3. UV Radiation which for cross-linking initiation and curing. 4. Fully cured lacquer. Adapted from* [22].

2.4 General Theory of Residual Stress in PVD Coating Systems

To be able to adjust the residual stress in a PVD film, one first need to understand how the residual stress is formed and what are the underlying forming mechanisms. This chapter therefore will provide a short theoretical background about residual stress in thin films.

2.4.1 Definition of residual stress

The stresses in thin films have three primary origins and can therefore be separated into

1- Intrinsic stresses
2- Thermal stresses
3- Mechanical stresses

The sum of intrinsic (σ_I) and thermal stress (σ_T) are often referred as residual stresses (σ_R) and can be expressed by the following formula[23]

$$\sigma_R = \sigma_T + \sigma_I \quad (1)$$

The mechanisms for the development of mechanical stresses are external loads and are not influenced by coating deposition [24].

The intrinsic stresses in the thin film layer result from the growth mechanism and build-in crystallographic flaws. Those factors can mostly be controlled by processing parameters. Some of those factors are surface diffusion controlled by substrate temperature. Other important parameters are film thickness, deposition rate, working gas pressure and substrate bias to name a few. The amount of the build-in intrinsic stress is connected to the film-microstructure, which itself depends on the kinetic energy of the sputtered target and impinging working gas atoms, as well as substrate temperature. A change in the microstructure often causes a volume or structural change which produces stresses due to a constraint of the film by the substrate. The intrinsic stresses itself can vary and become tensile or compressive. [19][24]

A SZD for magnetron sputtered metallic films is displayed in Figure 5. Based on experimental data, the SZD visualizes the expected film structure for different argon pressures and substrate temperatures. The effect of the temperature is expressed as the homologous temperature, which is an indicator for the diffusivity of the adatoms.[25][26]

The SZD shows four zones which can be well distinguished from each other. For polymer metallization, zone 1 and zone T are of most interest due to the limit in substrate temperature. The structure in Zone 1 is characterized by conic crystals and is generally a more open structure. A high working gas pressure favors the formation of this structure,

as it can be seen in the diagram. The formation mechanism of the structure itself is understood as a shadowing effect of the incoming atom flux for valley regions by already higher grown areas of the coating [19]. Additionally, a low adatom and grain boundary mobility at this temperature zone favors the formation of the columnar-like structure [13][27]. Coatings deposited in the Zone 1 process window usually show tensile stresses [19]. The structure of Zone T exhibits dense and fibrous V-shaped grains with a microstructure variation along the film thickness. The top exhibits usually a smooth and highly reflective surface. This structure development can be explained by an increased surface diffusivity in this region without any grain boundary diffusion. This results in low surface diffusivity grains overgrowing high surface diffusivity grains.[27]

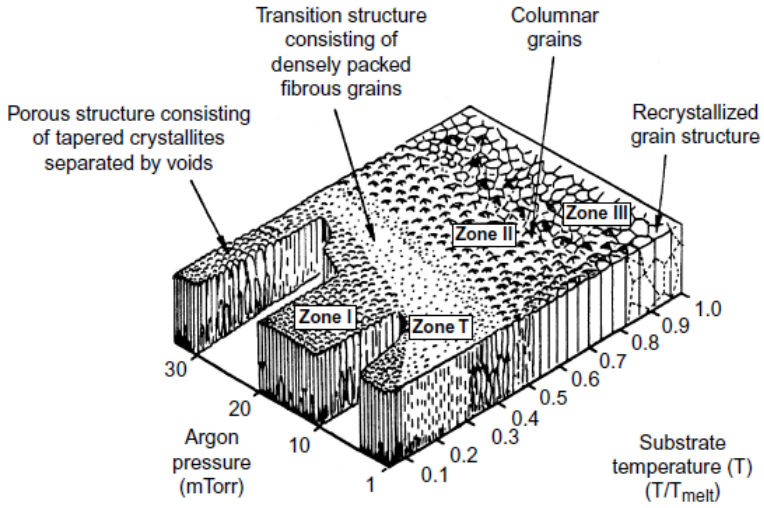

Figure 5. *. Schematic representation of the Structure Zone Diagram proposed by Thornton, which shows the change of the film structure in relation of the sputtering pressure and the homologous temperature.* [15]

The thermal stress arises from the mismatch of the coefficient thermal expansion (CTE) for film (α_F) and substrate (α_S). The temperature changes from room temperature to deposition temperature and cooling down after the deposition process causes this stress. The thermal stress can be calculated with the following formula [23]. Here E and ν denotes the Elastic modulus and Poisson's ratio of the thin film respectively. The operating temperature is given by T and the deposition temperature by $T_{dep.}$ [23][24]

$$\sigma_T = -E * (\alpha_F - \alpha_S) * \frac{(T - T_{dep})}{1-\nu} \qquad (2)$$

If high melting point metals, such as chromium (T_m =1907 °C) and zirconium (T_m= 1857 °C) are deposited at low temperatures, it is assumed that the intrinsic stress has a

higher contribution to the residual stress than the thermal stress component. This is attributed to the fact that, at low temperatures, the bulk diffusion for high melting point materials is low and flaws, which cause intrinsic stress and cannot be healed by diffusion and therefore can accumulate [19]. Additionally, the stress contribution caused by the mismatch of the CTE of the substrate and the film can be neglected, unless the differences are in different orders of magnitude.

Residual stress is usually defined as a location dependent function of stress in a material which is free from external factors such as forces, temperature and moments. The location dependences originate from the resolution of the used measuring method as well as from the size of the investigative material volume [28].

The distortion of the lattice is caused by dislocations, vacancies, interstitial and substitutional atoms as well as stacking errors. The obstruction of adjacent and differently oriented grains additionally leads to forces between those grains in polycrystalline materials.[28] Such forces are labeled residual stress and are of great importance for the coating durability. The problem however, with thin films, the substrate is most of the thicker than the film. This leads to a condition where the film needs to compensate the volume and dimensional changes of the substrate which leads to a rise in residual stress. The resulting stress often causes loss of adhesion or cracks in the film. Compressive residual stress for example, can prevent the emergence of cracks at the surface but can also lead to blistering of the film. The presence of tensile stress on the other side often results in cracking.[15]

Depending on the size of the volume, over which the residual stress is constant, the residual stress can be divided into 3 categories.

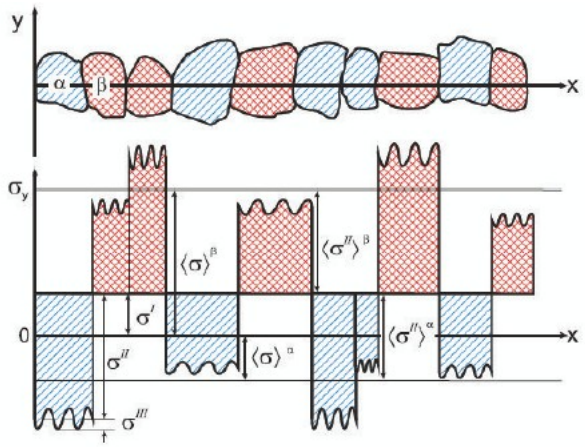

Figure 6. *Classification for residual stress type I, II and III in relation to the material volume range the stresses are detected* [29]

The type one residual stresses (σ^{I}) are homogenous over several grains and are therefore considered as an average stress value, which is representative for the specified material volume. The forces and moments, related to those stresses, are in equilibrium over a big material volume. A deviation from the equilibrium condition causes geometrical and

dimensional change on a macroscopic level. Because of the latter, residual stresses of type one are also called macroscopic residual stress. The type one residual stresses are measurable by the shift in the X-ray diffraction peak.[28][29]

Type two (σ^{II}) and type three (σ^{III}) residual stress are often summarized as microscopic residual stress. Type two residual stresses are homogenous within a grain and the attributed forces and moments are therefore in equilibrium over one or several grains. They arise due to anisotropic deformation behavior of the grains. A deviation from the equilibrium causes dimensional changes. The type two residual stresses are measurable by the shift in the X-ray diffraction peak. [28][29]

Residual stress of type three has its origin often in an inhomogeneous dislocation arrangement, vacancies or lattice defects, which cause an inhomogeneous stress distribution over several atoms within a grain. A deviation from the stress equilibrium does not cause any dimensional changes. The type three residual stresses do not cause a shift in the X-ray diffraction peak. However, they influence the peak shape. [28][29].

2.4.2 Residual stress development in PVD coatings

Residual stress which arises from the thin film growth process can have different sources. Several models to explain the emergence of residual stresses have been published over the years and will be shortly reviewed hereafter.

Residual stress models

An explanation for the occurrence of tensile in chromium films is given by Janssen [13]. He mentioned that the origin of the tensile stress is found at the grain boundaries, by stretching the film in the in-plane direction and contracting it along the normal axis. The correspondence between the micro structural evolution and stress, which stretches the film, was first introduced by Hoffmann [30] and is since then widely accepted as the main cause for tensile stress [31][32]. The base of his model is the assumption that neighboring islands can reduce their interfacial energy by forming new grain boundaries. During the film growth, such isolated islands grow into a continuous film. In this stage, an elastic deformation of the grain walls is imposed on the adjacent grain by attractive interatomic forces. Intragrain tensile forces, which arise due to adhesion of the film to the substrate, act as a counterbalance to those interatomic forces to maintain the mechanical equilibrium. The underlying assumption of this model is that the adhesion forces at the substrate/coating interface exceed the arising interatomic attractive forces.[19][30-32]

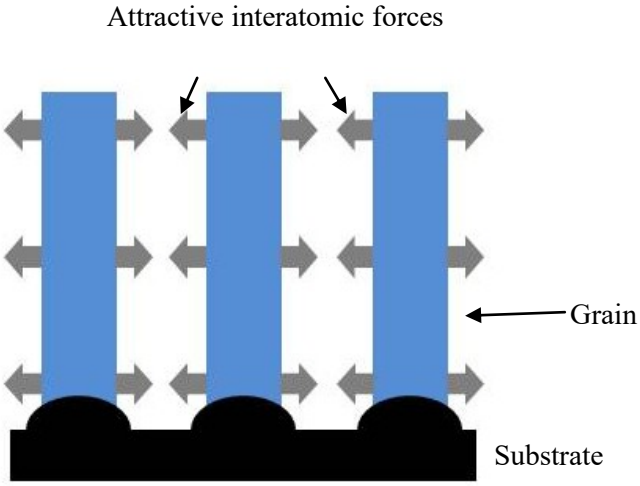

Figure 7. *Visualization showing the stress inducing mechanism of the Grain Boundary Model. Adapted from* [33]

Contrary to the tensile stress generating mechanism, the mechanism for compressive stress generation is more unclear and under constant debate. [30-32] One mechanisms which is often referred to is a model proposed by Chason [31]. He suggested that due to the non-equilibrium nature of the deposition process the chemical potential of surface atoms is raised. This offers the necessary driving force for the atoms to flow into the grain boundaries and induce compressive stress by insertion into them. [30-32]. Also Spaepen [34] named grain boundaries as a main contributor for the stress development.

He suggested that grain boundaries can act as sinks for vacancies or reduce the grain boundaries volume by grain growth. This can lead to the generation of tensile stress. In addition, they accommodate a stress relaxation by plastic flow [34].

Another factor for the occurrence of compressive stress is attributed to atomic and/or ion peening. During this process the film is densified by the bombardment of the incoming atoms and sputtering gas ions. This can great defects if ions/atoms arrive at energies above the lattice displacement energies of 10-30 eV [13]. For sputtered films, argon atoms from the sputtering gas, which can get entrapped in the film, are also considered as a contribution to the increase in intrinsic compressive stress. However, they are not considered to play a major role in the stress generating mechanism for compressive stress.[35]

Influence of Film Thickness

For magnetron sputtered chromium films Janssen [13] found a dependence of the stress on the thickness. On the basis of the previously mentioned GBR model, it is assumed that, since for T-zone films the grain structure and the grain size is a function of the film thickness, the stress is also a function of the film thickness. Janssen found a stress gradient which showed higher average tensile stress for thin films than for thicker films. He correlated this decrease of tensile stress during the increase in film thickness with a decrease in the amount stress causing grain boundaries [13]. In the results summarized by Ohring [16] a decrease of tensile stress for chromium films was observed in between a thickness of 20 to 80 nm. After this, the stress stayed on the same level. At the same time, an almost linear behavior of the relationship F/w vs. thickness (force per unit width) was observed between 20 to 160 nm. The range in which this relationship can be observed coincides with the formative stages of the film, namely the coalescence and channel stage of the film growth, which finally leads to a continuous film [16][36]. Additionally the low mobility Volmer-Weber growth mode which causes a columnar structure, generates stress at the grain boundaries an can also be attributed to the linear rise of the F/w with the film thickness of chromium.[16]

An opposite behavior in relation to development of stress with the film thickness was observed by Perry [19] for Tantalum films. He found a change from compressive to tensile stress with increasing film thickness. This behavior was explained with the Grain Boundary Relaxation model, which was mentioned above. The initial forming grains are small and as the deposition continuous those grains change their growth to columnar grains, which increase the tensile stress.

The results by Perry [19] show that, even though Cr, Zr and Ta are in the group of low mobility metals, it cannot be assumed that they also behave the same. This was confirmed by a study done by Abadias and his colleagues [37]. In their work, they found

that the structural and stress development largely depend on surface kinetics limitations and interfacial effects. This results in an interfacial energy contribution which favors a stable phase for W and Mo and the growth of a metastable phase in Ta.

For zirconium it is known that in an equilibrium condition it exhibits a hexagonal closed packed (hcp) crystal structure at room temperature. Upon increase of temperature, this structure undergoes a transition to body-centered cubic (bcc) at 863 °C[38]. Dolgusheva and his colleague [39] conducted calculations on the phase stability of zirconium thin films and found a dependence of structural transformations on the film thickness, with a critical film thickness of 6.1 nm. At room temperature, they found the presence of a face-centered cubic (fcc) phase due to this phenomena, which they said was also reported by other authors.[39] The occurrence of a cubic and a hexagonal phase in zirconium thin films was also reported by Usmani et al. [40]. This phenomenon has been pointed also out by Girardeau et al.[41] who reported that the phase of zirconium strongly depends on the deposition condition and can even occur as an amorphous film. Work published by Drese et al. [42] show also a crystalline structure which is strongly influenced by the oxygen content. Furthermore, they found a decrease in tensile stress /increase of compressive stress with the film thickness. A small amounts of oxygen however hamper the formation of crystalline metallic zirconium and lead to nanocrystalline/ amorphous like ZrO_2 [42]. This changes the stress evolution to an initial compressive state to an increase in tensile stress with the thickness, which is opposite to the evolution observed for pure metallic zirconium.

This rather unclear knowledge about the evolution of stress and structure of zirconium can be attributed to the limited amount of published data on properties of metallic Zr thin film as already pointed out by several authors [41][43].

Influence of Target Current/ Target Power

Several authors report a significant influence of the target power on the coating properties for magnetron sputtered films. Since the deposition rate scales linearly with the target power, it is considered an important parameter to investigate for achieving a fast process cycle time.[44] One important factor to keep in mind is that with an increase in target current the sputtered atoms show an higher excess in thermal energy, which can contribute to the heating of the film and therefore can cause changes the film microstructure [18]

Vergason and his colleague [1] for example reported that, by lowering the power of the sputtering target, fewer cracks can be observed for a chromium coating with a thickness of 300 nm [1]. Even though it was not specified if the coating exhibited tensile or compressive stress, cracks are usually attributed to tensile stress in the coating as mentioned above.

In a study conducted by Jörg et al.[44] molybdenum films were deposited with a wide range of target power while keeping the film thickens and pressure constant. The results indicated tensile stress for the low end of the investigated target power range and compressive stress for the high end of the target power range. A similar increase of compressive stress with an increase in target power was obtained by Chiang et al.[45] for Tantalum films.

Besides the stress, the texture of the films is also influenced by the target power as has been shown for relative thick chromium films by Moore et al.[46]. They found a preferred orientation of <110> for target powers 1 to 2 kW, which changed to a <200> orientation, for a power higher than 3 kW. At the same power threshold a significant increase in the grain size was observed also [46]. The authors explained that with an increase in target power, the energy of the particle increases whereas a decrease in ion to neutral ratio can be observed. This decrease in the ion to neutral ratio lowers the energy/atom which is deposited on the growing film. The resulting change in growth kinetics was considered a contributing factor for the grain growth of the <200> orientation.[46].

Perry pointed out in his work [19] that if one operates the target at a set power and lets the voltage vary, the stress levels of the film will change over time. He assumed that a reduction in current, hence an increase in voltage for a fixed target power, reduces the number of ions which strike on the target. This leads to a reduction in neutrals which impinge on the coating. For low deposition pressures, this results in less atomic peening and therefore, less compressive stress. For high deposition pressures, this results in a lower shadowing effect, resulting in lower tensile stress. To adjust the process and take into account the target aging, he concludes that for controlling the stress, the coating should be sputtered at a constant voltage and not at a floating voltage with a constant target power.[19]

Substrate Rotation

Since the PVD process is considered a line of sight deposition process at chamber pressures lower than 0.01 mbar, the substrate rotation as a process parameter has an effect on the resulting microstructure of the thin film [20].

An explanation for this was given by Panjan and his colleagues [47] with the different trajectories of the sample for different rotation modes. When mounted on either a one-fold, two-fold or three-fold rotation, the trajectory is either circular, helical or in form of a double helix for the different modes, respectively. This result in different durations the sample spends next to the dense plasma region of the target. If the substrate in one-fold rotation passes the target, the orientation, as well as the distance to the target, is kept constant. When the substrate faces away from the target the plasma density drops drasti-

cally. This results in a very fast directional growth mode which abruptly changes to a complete stand still when facing away from the target. In a two and three-fold rotation setup, the target distance as well as the orientation changes. The latter makes shadowing an important factor for growth in two- and three-fold rotation, while it is not present in a one-fold rotation. [47] During shadowing, protrude areas hinder incoming particle of reaching those shadowed areas. This leads to a formation of voids between the columns and fibers [20]. Another aspect, which however is not considered a major factor, is that the constant flux of incoming particles changes, resulting in heating up of the substrate [20].

Eriksson and his colleagues [48] argued that substrate rotation is beneficial to equally expose all areas of the substrate to a deposition flux, especially when the substrates are large. However, the rotation could cause an artificial layer due to anisotropic growth conditions which changes the mechanical properties of the coating [48]. Panich and his colleague [49] found a substrate rotation induced change in mechanical properties, structure and orientation for magnetron sputtered TiB_2. This was ascribed to the alteration of adatom energy, which is influenced by a rotation-induced change in substrate-to-target distance.

Varying Sputtering Gas Pressure

An approach of varying the working pressure for adjusting the stress in sputtered films is presented in [35]. It is pointed out that there is a transition from compressive to tensile stress at a certain argon working pressure. This critical gas pressure point, at which this change occurs, increases for the elements as a function of the atomic mass, as can be seen in the following picture with critical gas pressure point for Cr, and Zr are indicated by the horizontal lines. Results published in [16] show a transition of stress for chromium at around 5.0 x 10^{-4} mbar from compressive to tensile and reversal from tensile to compressive at 1.0 x 10^{-2} mbar. It was pointed out by Ohring [16] that each of the sputtering parameter sets probably has his own reversal point. Considering the relationship of the atomic mass of chromium with the stress transition point, it is evident that chromium often shows tensile stress due to its low gas pressure at which a transition from compressive to tensile stress occurs.

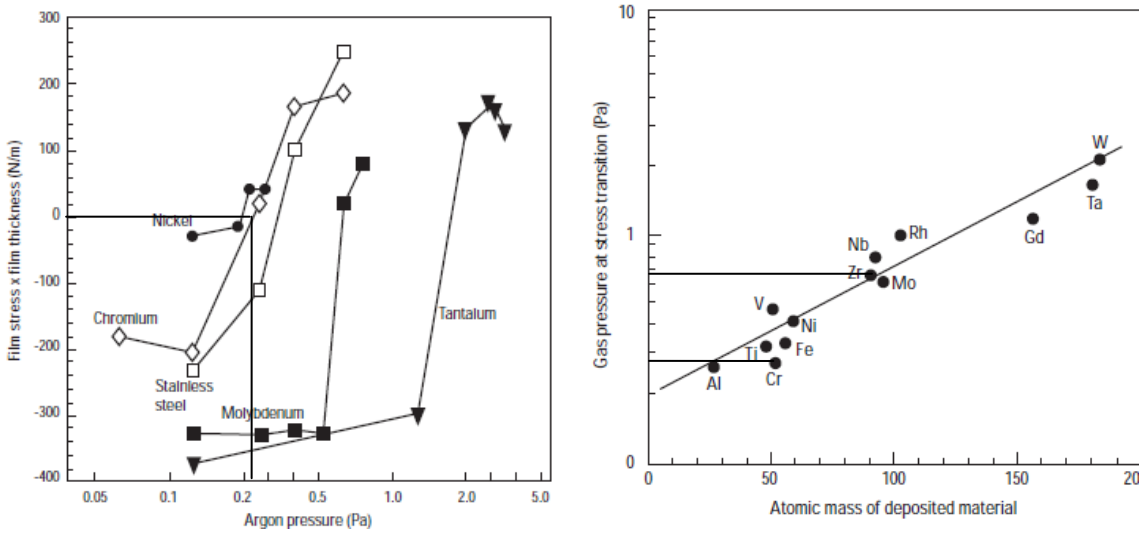

Figure 8. *Dependence of the threshold for the gas pressure at which a change from intrinsic compressive to intrinsic tensile stress occurs.*[35] *The results are originally from the works of Thornton and Hoffman (1977)*

A similar dependence of low working gas pressure and low deposition rate resulting in compressive stress and an increase in those leading to high tensile stress was also found by Hoffman and his colleague [50]. Suominen et al. [51] found that sputtered chromium films show inherently tensile stress and suggested also that this is controlled by adjusting the argon pressure, as well as controlling the deposition temperature. The latter is not an option in this case due to the thermal sensibility of the polymer substrates.

An explanation for the occurrence of higher compressive stress with lower argon pressure was given in [35] with the fact that, less argon gas atoms hinder the flight of the atoms from the target on the way to the substrate. This results in less energy loss by collisions, and overall the target atoms arriving the substrate then have a higher energy.[35]

Karabacak et al. [52] used a slightly different approach by depositing a nanostructured compliance layer (NCL) by alternating the working gas pressure. The NCL is deposited, starting with a high working gas pressure of 15 mTorr to obtain a low stressed NCL tungsten layer and gradually decreasing the working gas to 2 mTorr at the end of each NCL. With the method, they were able to significantly lower the stress in the film and remove any peeling of the thin film.[52].

In literature [15] it is pointed out that ions which bombard the target can be neutralized and backscattered without losing much of their energy. In a low gas pressure environment, those so called high energy reflected neutrals are not thermalized and bombard the growing film and influence the film properties The problem with this process is that it is very hard to control and therefore a very good monitoring of the process pressure is needed. [15]

Multilayer Structures

Tinone et al.[53] achieved a control in stress in a Mo/Si system (molybdenum in a tensile state, silicon in a compressive state) by adjusting the layer thickness of the two materials, and therefore, tailoring the stress of the whole multilayer system. Guo and her colleagues [54] had similar results and showed that the stress of the whole system depends on the film thickness of the single layer and their stress values. They correlate the stress of the single layers to the overall stress via the general rule of mixture, which is applicable to composite materials in material science. This approach will be further discussed in detail later on. The method of adjusting the stress in a multilayer film by combining a layer with compressive and tensile stress is also pointed out in several patents [55][56].

2.4.3 Residual stress development in UV lacquer

One of the challenges of UV curable lacquers is to maintain the desired properties while simultaneously keeping the UV curing process speed high [57]. The whole curing process of UV coating can be divided between a solvent evaporation and a cross-linking part. In both processes, volume contractions take place. Due to the fast cross-linking reaction, residual stress can arise in the coating and impair the adhesion. If good adhesion to the substrate is given, this shrinkage is inhibited, which leads to the rise of intrinsic stress in the coating.[58]

During the flash off step, the solvent is evaporated while simultaneously secondary valence bonds and primary bonds begin to form. Those bonds form in one area of the coating and inhibit neighboring polymer segments to migrate to the holes, which are left by vacant solvents molecules. This causes a locking of free volume and restriction of polymeric mobility, which prevents shrinkage. Additionally, side groups and branches of the molecules obstruct the inter-chain associations in the adjacent volume. Those processes add up to the development of residual stress.[58]

The polymerization process consists of the formation of covalent bonds which causes a shortening of the distance of the final bonds length, compared to the initial bond lengths. As a result of this, the whole polymer matrix is pulled together which causes shrinkage and inevitably stress in the coating.[10][58]

Depending on the properties of the lacquer, the residual stress is either released or stored in the coating. Hard and brittle lacquers with low elongation properties and tensile strength either undergo cracking or delimitation for releasing the stored strain energy. Softer coatings, which exhibit a higher elongation but low tensile strength, will undergo deformation to release the build-up stress. Tough lacquers, with high tensile strength and elongation, are not able to release the stress by either cracking or deformation. Given good adhesive and cohesive strength, those coatings will be strained, which causes internal stress.[10][58]

The amount of stress which is stored in the lacquer dictates the sum of additional stress which can be applied before failure. If a highly stressed film is impacted by an object, the film can chip, whereas a film with lower levels of internal stress will not fail upon impact.[58]

2.4.4 Residual stress in multilayer film systems

To control the stress in a multilayer by its single layers, it is crucial to understand how the monolayer affects the overall system. A method to predict the residual stress in a multilayer system based on measurements on its monolayer was mentioned by Guo and his co-workers [54] as well as by others [59]. The method is based on the contribution of the thickness weighted stress of every single layer to the stress of the whole system. It can be expressed with

$$\sigma_{1,2,\dots n} = \frac{\sum_{i=1}^{n} \sigma_i t_i}{\sum_{i=1}^{n} t_i} \qquad (3)$$

Here $\sigma_{1,2,\dots n}$ is the residual stress of the whole multilayer system that depends on its number of mono-layers *n ((n≥1),* the residual stress of the monolayer σ_i and their individual layer thickness t_i. The authors [54][59] used this relationship to manage the overall stress by adjusting the single layers. The used residual stress of the mono-layers was derived from curvature method which is based on the Stoney formula.

Guo et al. [54] validated their assumption for several coating systems. The found relative error of the calculated and measured value was between 0.2 and 10.7%. This was mostly attributed to the stress which arises at the substrate/ film interface for single layer, or film/film interface for the multilayer system [54]. This so-called interface stress is a known factor for affecting the residual stress in multilayer systems as it has been mentioned by several authors [13][34][60]. Therefore, a direct transfer from the stress measured for the monolayer to multilayers contains some errors.

The force per unit width (*F/w, expressed in N/m)* which is responsible for the bending of on the substrate by a multilayer film, consisting of Material A and B, has three contributing factors. Those contributions are the average stress of layer A times its total layer thickness, the average stress of layer B times its total film thickness and the number of interfaces times the interface stress. Janssen [13] proposed that the contribution of the interface can be isolated by varying the single layer thickness, while keeping the total film thickness constant if no layer thickness dependence for the stress exists.

The ground work for this was done by Spaepen [34]. He derived the following formula

$$\frac{F}{w} = \langle\sigma\rangle * t_f + N * f \qquad (4)$$

Here the *F/w* acting on the substrate, acquired from the Stoney equation, consists of $<\sigma>$ which stands for the average residual stress measured by XRD, t_f the thickness of the film, *N* the number of interfaces and *f* the interface stress.[34]

2.5 Measuring coating properties

In the following section the theoretical background about the used measuring methods is given to provide some understanding about the limitations and assumptions.

2.5.1 Basics of XRD

X-Ray microstructure analysis makes use of the fact that the monochromatic wavefront of the X-Ray beam gets diffracted by the crystal lattice of a crystalline material. Such a crystalline material is made up of atoms, which are arranged in a periodic pattern in all three dimensions. This arrangement leads to either constructive or destructive interference upon diffraction of the X-ray beam. The specific diffraction angle θ for interference can be connected to the wavelength λ of the x-ray beam and the interplanar spacing d_{hkl} by Bragg's law. [28][61]

$$\lambda = 2 * d_{hkl} * sin\,\theta \qquad (5)$$

The inter-planar spacing (d_0) of unstrained lattice planes {hkl} produces a characteristic diffraction pattern, which is independent of the orientation of the grain. Plastic deformation leads to strain, which is on the other hand, orientation dependent. For illustration see Figure 11.[62]

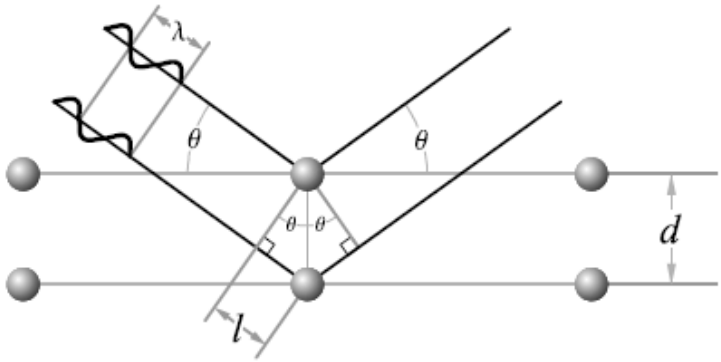

Figure 10. *Illustration of X-Ray diffraction at lattice plane which shows how the recorded angle θ is related to the inter-planar spacing d* [63]

2.5.2 The sin2ψ method

The stress measurement by XRD utilizes the fact, that if the material is strained, the resulting elongations or contraction of the inter-planar spacing will lead to a detectable shift in the diffraction pattern. By measuring the shifts in the diffraction pattern, the induced strain in the lattice, and therefore in the material, can be deduced. From this strain, the associated residual stress can be determined by the help of elastic constants. To be able to calculate the residual stress, a mathematical relationship needs to be estab-

lished which considers the strain in dependence on the peak shift for differently oriented grains. [28],[62]

Tilting the sample by the angle ψ allows measuring strains of planes which are tilted by the same angle (d_ψ) in reference to the surface normal of the sample, and hence are brought into position to fulfill the Bragg's diffraction condition. [28],[62]

$$\varepsilon_\psi = \frac{d_\psi - d_0}{d_0} \qquad (6)$$

By assuming an in-plane biaxial stress state, where the stress component in the z-direction vanishes ($\sigma_z = 0$), and that the XRD signal only comes from the sample surface, the stress can be calculated from the strains acquired by equation (7) utilizing Hooks law.[28][62]

$$\frac{d_\psi - d_0}{d_0} = -\frac{\nu}{E}(\sigma_x - \sigma_y) \qquad (7)$$

Utilizing the sin2ψ method, a linear relationship between inter-planar strain and the tilting angle ψ can be found.

$$\varepsilon(\Psi,\varphi) = \frac{d(\Psi,\varphi) - d_0}{d_0} = {}^1\!/_2\, S_2\sigma_\varphi * sin^2\Psi + S_1 * (\sigma_1 + \sigma_2) \quad (8)$$

Here the measured strain ε depends on the inter-planar spacing d which itself depends on the measuring geometry angles ψ and ϕ. The constants s_1 and ${}^1\!/_2\, s_2$ are material dependent elastic constants.[28]

$$s_1 = \frac{-\nu}{E} \qquad {}^1\!/_2\, s_2 = \frac{\nu+1}{E}$$

Those constants are dependent on the poisson ratio ν and the Young's modulus E of the material. The ½ in front of S_2 is not meant as a multiplier, it is part of the name of the constant. Equation (8) can be simplified to (9a).[28],[62]

(9a) $\sigma_\phi = \frac{E}{(1+\nu)sin^2\psi}(\frac{d_\psi - d_n}{d_n})$ (b) $\sigma_\phi = (\frac{E}{1+\nu})m$ (9b)

The equation allows plotting the inter-planar spacing in dependence of sin2ψ. The y-axis intercept at sin2ψ = 0 for this plot equals to the unstressed lattice d_0 = dn, with d representing the y-axis intercept. From the slope m and the elastic constant the stress can be calculated by equation (9b) [62]. The presented elastic constants are isotropic elastic constants, as they are obtained by the Young's modulus and Poisson's ratio from the bulk material. Those constants however, fall short in taking into account the differences in the stiffness of different lattice planes {hkl}. By using the X-Ray Elastic Constants (XEC) s_1^{hkl} and ${}^1\!/_2\, s_2^{hkl}$, the elastic anisotropy in each spatial direction of the primitive cell is accounted for.[64]

X-Ray Elastic constant can either be determined by measuring the peak shift under a known stress of a sample or by calculation from single crystal datasets. For calculations from single crystal datasets, an assumption regarding the grain coupling induced interaction needs to be made [65]. In this Thesis work, the Program *DECcalc* will be used for calculating the XEC. For further information, the reader is referred to [15].

Common grain interaction models are the Voigt, Reuss, Kröner, Eshelby and Hill model. The Voigt model assumes the same level of strain in all grains, independent of their orientation. This results in an instant rise in stress at the grain boundaries which are not in accordance with the mechanical stress equilibrium. Contrary to this, the Reuss model is based on the assumption, that the stress in all grains is homogenous, which results in a direction depended strain for differently oriented grains. However, this approach leads to strain-incompatibilities, which would result in discontinuities such as pores at the grain boundaries. Hill pointed out, that those two cases are the theoretical limits and chose the average of both for his model, which leads quite often to results that are in accordance with real material behavior. The Kröner model, which was building on the previous work of Eshelby, takes into account the stress and the strain equilibrium conditions, and therefore, describes the interaction of the grains with their surrounding matrix. [64][65] Literature and industry standards suggest relying on X-Ray Elastic constant if accessible and avoid using macro-isotropic elastic constants if possible .However, one need to take caution and considered how these were acquired if the values are used quantitatively rather than qualitatively [66]. Furthermore, it is suggested to use the grain interaction model from Kröner or Hill and avoid the Reuss and Voigt model for the reasons which were mentions before.[62][64]

The biggest drawback of the sin2ψ method is the dependence of the penetration depth on the measuring angles 2θ and ψ. This results in problems if a stress gradient is present as well as in a bad utilization of the available material volume in thin films. To overcome those drawbacks, the grazing angle incidence (so-called GID-sin2ψ method) is often times utilized.[67][68]

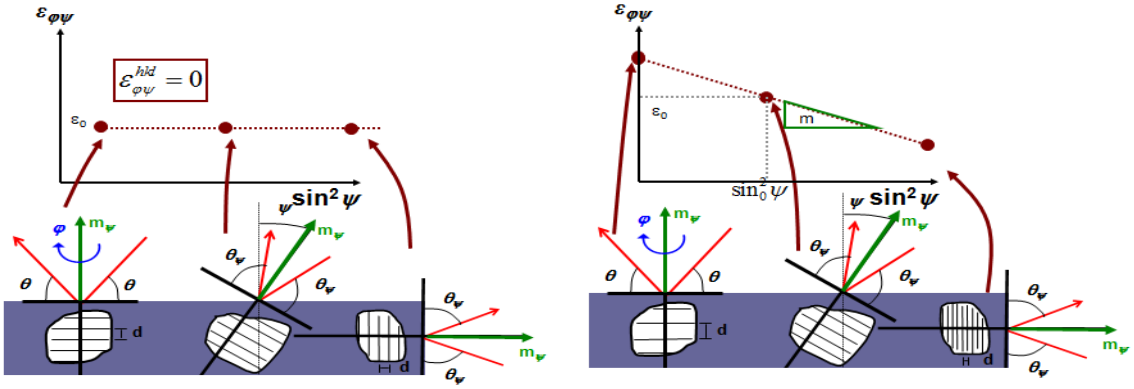

Figure 11. *Principle of the sin2ψ method. Unstrained sample results on a line with the slope = 0 (left). Strained sample results in a line with slope = m (right)*

2.5.3 The cos2αsin2ψ method for thin films

Contrary to the conventional sin2ψ-method, which operates in the symmetrical Bragg Brentano geometry, the cos2αsin2ψ uses asymmetrical diffraction geometry [67]. For this, the incident X-Ray beam is fixed at a grazing angle γ with respect to the sample surface while the angle ψ still represents the sample surface tilting angle like in the conventional sin2ψ-method. The main advantages of this method are the lower influence of inhomogeneous strain on the stress results and the almost constant penetration depth, which increases the utilized effective irradiation volume for thin-film samples [67][68]. The last point increases the intensity of peaks, especially high angle ones, which sometimes do not show up in highly textured or very thin films when using the conventional symmetrical Bragg Brentano setup[67][68].

The underlying measuring mechanisms for the cos2αsin2ψ method rely on the same principles as the sin2ψ method. The main difference lies in the correction factor cos2α which accounts for the asymmetric geometry resulting from the used grazing incidence angle γ. A more in detail explanation of the method is presented in [67][68][69].

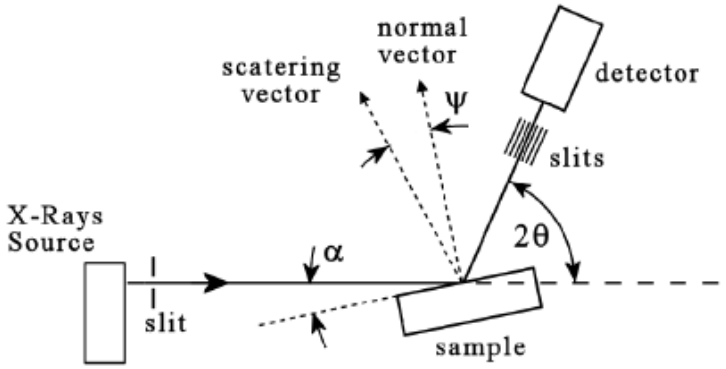

Figure 12. *Schematic representation of the measuring setup of the cos2αsin2ψ-method and the relevant measuring angles α, ψ and θ* [68]

2.5.4 Determination of crystalline size by Debye Scherrer

According to the Debye Scherer equation, the width at half maximum of the peak is inverse to the crystalline size of the investigated material. The crystallite size is represented by D, G is the shape factor of the crystallites which varies between 0.89 for spherical and 0.94 for cubic crystallites. The used wavelength is represented by λ and cosθ is the angular position of the investigated peak. The constant β_s is the difference in measured FWHM (Full Width at Half Maximum) and the peak broadening induced by the measuring setup.[70]

$$D = \frac{G*\lambda}{\beta_s*\cos\theta} \qquad (8)$$

2.5.5 Texture evaluation

The texture of a polycrystalline material is defined by the orientation of a set of lattice planes {hkl} from a specific crystallite in reference to the sample. Fixing the detector and primary beam to a specific 2θ angle only results in a reflection of the X-Ray beam, if the lattice planes lie parallel to the sample surface. To achieve more reflections, the sample needs to be tilted and rotated to make sure, other oriented lattice planes of the family fulfill the Bragg equation (see section 2.5.1) The needed rotation and tilting angles to bring the lattice plane to diffraction are indicative of how the lattice planes in the crystals are oriented in reference external sample frame. [71]

To determine the orientation in a practical manner, the crystallites of a sample need to be rotated (φ) and tilted (χ) in a systematic way to bring the differently oriented planes into diffraction position. Simultaneously the diffracted intensity in relation to those rotation and tilting angles needs to be recorded. The recorded intensity along the measured rotated (φ) and tilted (χ) angles can be directly related to the pole figure angles α_R (radial) and β (azimuthal) as can be seen in Figure 13. For a polycrystalline material, the recorded intensity at a set tilting and rotation angle represents the volume fraction of crystallites which fulfill the reflection condition under those angles. A pole figure therefore is a representation of the distribution of orientations, hence the crystallographic texture of the sample.[71][72] For a more detailed description, the reader is referred to [70-72]

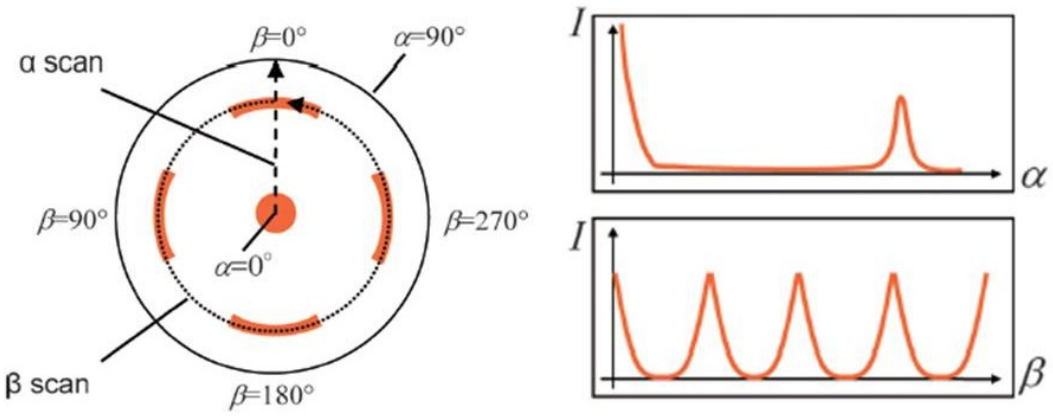

Figure 13. *Example pole figure with the definition of the angles α and β (left.)Scan signal along the angles α and β as they are indicated in the left picture (right)* [72]

2.5.6 Stoney formula for stress determination

The Stoney's Equation is often used to determine the stress in thin films due to its simplicity. The internal stress of a thin film causes its substrate to wrap/ bend to maintain a mechanical equilibrium of the net force *F* and the bending moment *M* of zero, which can be seed in Figure 14

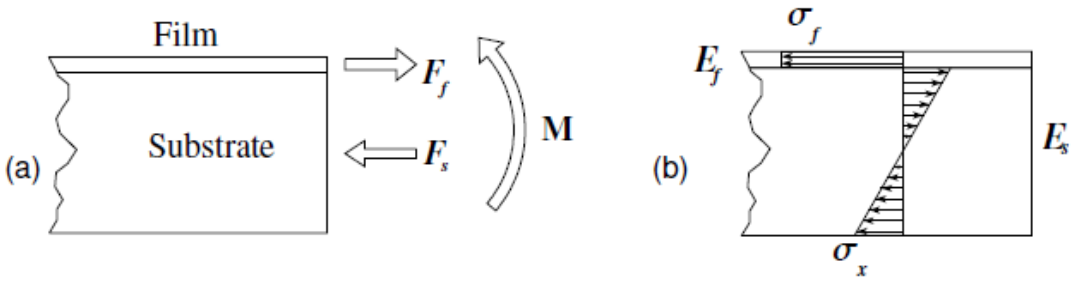

Figure 14. *Forces and Moment resulting from residual stress acting on a cross-section area of the film/substrate composite. This equilibrium conditions is the basis of the Stoney Equation.*[63]

Based on this film induced curvature of the plate-like substrate, the average film stress can be calculated. In case that the substrate thickness is big compared to the thickness of the film, the stress σ^f can be calculated without knowing the mechanical properties of the film. Based on the formula which was published by Stoney in the year 1909 the residual stress can be derived with

$$\sigma^f = E_s \frac{t_s^2}{6(1-\nu_s)*t_f} * \left(\frac{1}{R_2} - \frac{1}{R_1}\right) \qquad (9)$$

Here E_s and ν_s stand for elastic modulus and Poisson's ratio of the substrate respectively. The letter *t* with the subscripts *s* and *f* denote the thickness of the substrate and the film respectively. The curvature radius of the substrate is represented by the letter *R*. The subscripts *2* refers to the radius after deposition, whereas the subscript *1* to the one before deposition [63][73]. The constants belonging to the substrate are often times summarized in the factor *k,* which describes the bending stiffness of the used substrate. For a round disk the formula can be rewritten as displayed equation 13a. Here the radius change is converted into a wafer deformation value Δh. By this formalism it can also be shown that the observed bending depends on the substrates mechanical properties, represented by E_s and ν_s and the substrate geometry, in particular the thickness t_s and the diameter D_s. Those to factors or often conveniently summarized in factor *k* (see equation 10b) which is a measured for the substrate stiffness.

$$\sigma^f = \left(\frac{E_S}{1-\nu_S}\right) * \frac{8t_S^2}{6{D_S}^2} * \frac{\Delta h}{t_f} \qquad (13a) \qquad\qquad \sigma^f = k * \frac{\Delta h}{t_f} \qquad (13b)$$

The approach for predicting the stress in a multilayer in section 2.4.4 is based on the fact that the curvature of each individual layer can be superimposed in the Stoney equation. Each of those curvatures is again induced by the bending moment of the individual layer imposed on the substrate. Since the curvatures can be added up, so can the moments.[16]

There are different ways to measure the curvature of the substrate pre and post deposition. Common methods can be divided into contact and contactless measurements. The contactless measurements category includes optical interferometry, optical profiling and X-ray diffraction, which is used on single crystals. In the contact measurement category falls the mechanical profiling with a profilometer, which will be utilized for curvature measurement in this work. All of those methods have in common that the residual stress induced spherical bending of the substrate will be measured. This curvature is constant over the substrate surface, which allows one to measure it at any point of the surface. However, the displacement will be the highest in the center of the circular substrate and therefore yields the greatest sensitivity to changes in residual stress.[74]

The profilometer uses a stylus with a very sharp tip, which allows to accurately determining the radius of curvature with a very high resolution. For this, the stylus is moved over the surface of the wafer from one edge to the opposite edge while simultaneously recording the height.

2.5.7 Stresses and Forces in the Stoney equation

In his work, Hong [33] showed that by increasing the film thickness the force per unit width (F/w), which represents the total interface-stress force, also increases. He concluded that simultaneously the adhesion between film and substrate might decrease. In relation to that, he presented a term critical film thickness t_c. In the initial film forming phase ($t_f < t_c$), the interfacial force the film induces on the substrate, increases substantially. Whereas in the region ($t_f > t_c$) the change of F/w in relation to the increase in film thickness is low in comparison.[33]

Long and her colleague [75] used the term of a critical interfacial force, above which they were able to observe cracking. Their observation validates what Hong [33] suggested in his work. Furthermore, they made a conclusion that for a fixed critical interfacial force, decreasing the substrate thickness allows increasing the film thickness. This is understood with the fact that a thinner substrate or a substrate with a lower Young's modulus can comply easier than a stiff and thick one. Therefore the force which is used for bending of a complying substrate, can cause film cracking in a stiff, thick one [75].

2.5.8 Nanoindentation

Contrary to the classical micro hardness testing via Vickers, where the hardness is derived from the diagonal of the indentation, the instrumented nanoindentation derives the indentation hardness H_{IT} from the quotient of the maximal measuring force P_{max} and calculated, projected contact area A_P between the indenter and the measured material at the penetration depth $t_{p.}$

$$H_{IT} = \frac{P_{max}}{A_P} \qquad (11)$$

The penetration depth t_p is derived from the maximal penetration depth t_{max} and the intersection of the tangent of the force reduction curve with the penetration-axis (x-axis). The following picture serves as visualization for further clarification. Usually, the tangent is fitted in the upper 80% of the force reduction curve.[61],[76]

$$t_p = t_{max} - 0{,}75 * (t_{max} - t_r) \qquad (12)$$

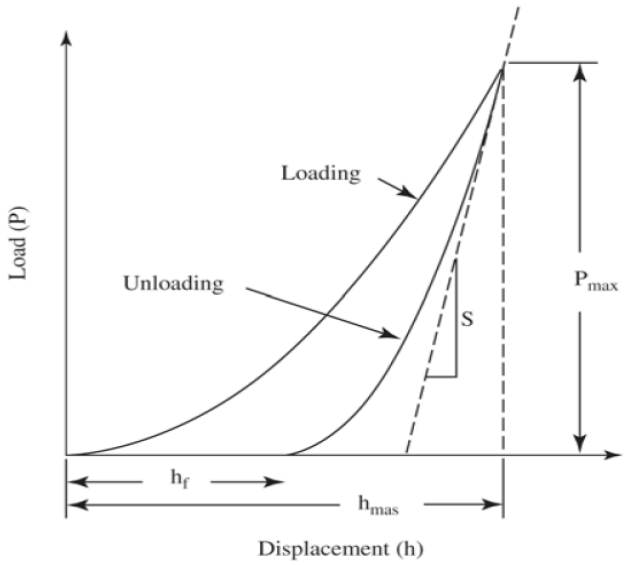

Figure 15. *Schematic drawing of the force-penetration curve in an nanoindentation measurement and the characteristic values which are used to calculate the indentation hardness.*[77]

Based on the theory of the hardness measurement, it is also possible to determine the elastic Indentation modulus E_{IT} with the following equation. Under ideal circumstances, where no pile-up and sink-in occurs, the measured E_{IT} equals to the normal elastic modulus measured under compression. The procedure is similar to the one for the hardness calculation. Furthermore, the Poisson's ratio of the indenter ν_E (for diamond this is 0,07), the Poisson's ratio of the sample ν_P and the Young's modulus of the indenter E_E are needed. [61]

$$E_{IT} = \frac{1-\nu_P{}^2}{\frac{2-C*\sqrt{A_P}}{\sqrt{\pi}} - \frac{1-\nu_E{}^2}{E_E}} \qquad (13)$$

To obtain correct results the Bückle-rule needs to be maintained, which states that, for a result without any influence of the substrate, the penetration depth is not allowed to exceed 10% of the coating thickness. [77]

Substrate Correction with FilmDocotor® Software

To correct the measured hardness and elastic modulus of the thin films for the influence induced by the substrate, an algorithm included in the software *FilmDoctor®,* offered by the company *SIO® Saxonian Institute of Surface Mechanics* was used. The calculation was done with the mechanical properties of the substrates listed in Table 1 of the following section. This allows for obtaining a more accurate hardness value and Young's modulus. The later can then be used to calculate more accurate stress values by using the XRD.

According to the manual provided by the company, the method is described as a closed analytical model for layered materials, without utilizing any form of finite element or boundary element methods. A detailed description is beyond the scope of this thesis and the readers are referred to [78] for more information on the procedure and detailed literature list.

3. RESEARCH METHODOLOGY AND MATERIALS

Even though the ePD™ system is applied on polymer substrates, glass substrates will be used in this thesis. This has its roots in the fact that thin glass wafers can be easily used to measure the stress in the coating. To avoid any substrate influence and being able to compare the film grown on the bending plate with the film used for SEM and XRD measurements, glass microscope slides are used for those measurements.

A detailed description of the experiments and measuring setup of the structural characterization technique is presented hereafter.

3.1 Used substrate materials

To measure the stress with the bending method, very thin glass plates (*MEMpax®*) are used as a stress measurement sample (SMS) to detect even small amounts of bending induced by the film. The plates have diameter of 50 mm and a thickness of 0.2 mm.

Table 1. *Name and properties of the used glass substrates*

Name	Material	Sample abbreviation	CTE [10-6/K]	Elastic Modulus [GPa]	Poisson Ratio	Source
Microscope Slides	Soda-lime glass	MS	9.0	64.0	0.22	[79]
MEMpax®	Borosilicate	SMS	3.3	62.7	0.196.	[80]

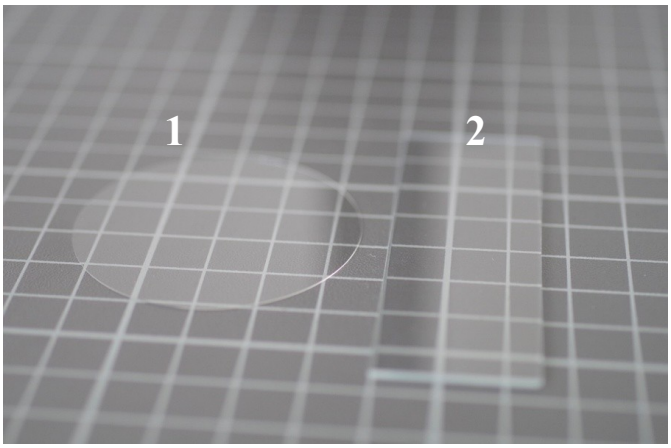

Figure 16. *Pictures of used samples. 1. SMS, 2. Microscope slide*

3.2 Coating deposition

As a part of this Master Thesis, seven test series were conducted to investigate the connection of the PVD process parameters with the residual stress (primary focus) as well as how stress can be managed in the ePD™ Multilayer System (secondary focus). The samples were produced at the Oerlikon Balzers Production facility in Stetten a.k.M. (Germany) on the small research batch machine B23p.

The following experiments, with their different focus in this thesis, to investigate the process parameters were conducted.

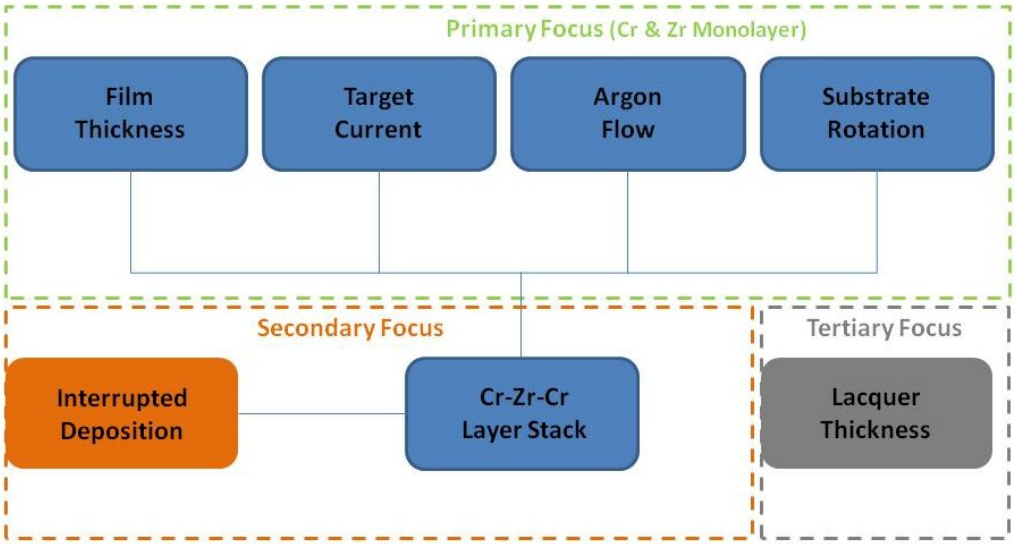

Figure 17. *Research plan scheme which shows the overview of the investigated process parameters with the indicated focus in this thesis.*

Based on a defined standard process setup, which can be seen in the table below, interesting process parameters were developed. The chosen parameter window was restricted so that the processes can be transferred from the research machine to a production coating machine, if wanted.

Standard Setup

Table 2. *Used standard setup for the experiments*

Material	Target Current [A]	Target Voltage [V]	Sputtering Time [s]	Rotation speed [1/min]	Sputtering Pressure [mbar]
Chromium	5	390	152	30.0	≈1.0 x 10^{-3}
Zirconium	8	360	160	30	≈1.0 x 10^{3}

3.2.1 Sample preparation

Cleaning and substrate preparation

The SMS were stored in a ziplock bag and were cleaned by the manufacturer. Therefore, only a simple cleaning by Isopropanol was done beforehand for both SMS and MS. The SMS were measured the day before the coating deposition and marked for identifying the measured side and the curvature measuring points after the coating process.

Charging the coater

A small strip of double-sided adhesive tape was used to glue the already masked microscope slides on the samples holder. For the stress measurement discs, a sample holder was constructed, which allowed free movement and bending of the samples without falling off. After this, the samples were placed in the coater and the process was started.

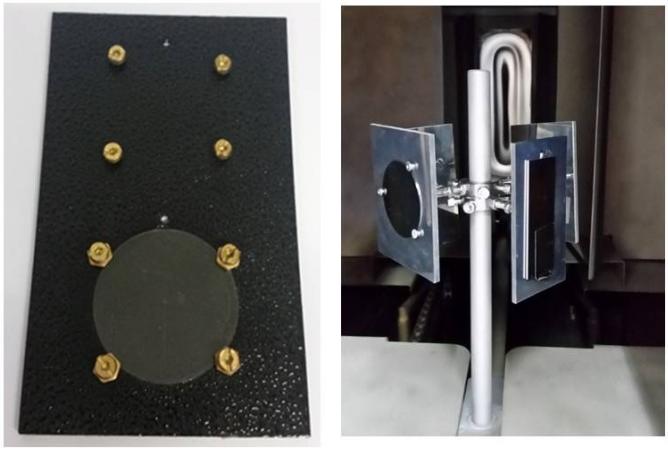

Figure 18. *Picture of the SMS holder (left). And of a loaded carousel with SMS and MS sample (right).*

Pumping

The first pumping step was done by a root pump included evacuating the coater and the turbo pump to a pre-vacuum of around 10.0×10^{-1} mbar. After the pre-vacuum was reached, the turbo pump evacuated the system to a minimum pressure of 8.0×10^{-5} mbar with a minimum pumping time of 600 seconds. The pressure during the process was controlled by adjusting the argon flow.

Coating Deposition

Starting from the standard process setup for chromium and zirconium, which is shown in Table 2, the process was varied according to the outlined research plan. The following list shows all the conducted experiments with its process parameters. For a better guidance the process parameters are paired together and the investigated parameters are highlighted in bold.

Table 3. *Overview of all conducted experiments and the process parameters*

Batch	Variable Parameter	Material	Target Current [A]	Time [s]	Pressure [mbar]	RPM [1/min]	Target Power [W]	Aimed [As]	Realized [As]
#1160	Target Current	Cr	**3**	253	9.4×10^{-4}	30	996	760	734
#1161		Cr	**5**	152	9.8×10^{-4}	30	1950	760	734
#1162		Cr	**8**	95	9.5×10^{-4}	30	3344	760	726
#1169		Zr	**5**	256	9.1×10^{-4}	30	1600	1280	1238
#1170		Zr	**8**	160	9.1×10^{-4}	30	2888	1280	1210
#1171		Zr	**13**	99	9.1×10^{-4}	30	5200	1280	1215
#1163	Film thickness	Cr	5	**1216**	9.7×10^{-4}	30	1895	6080	5845
#1258		Cr	5	**1010**	9.5×10^{-4}	30	1895	5050	4843
#1164		Cr	5	**760**	9.7×10^{-4}	30	1900	3800	3486
#1165		Cr	5	**456**	9.7×10^{-4}	30	1900	2280	2215
#1257		Cr	5	**320**	1.0×10^{-3}	30	1900	1600	1558
#1166		Cr	5	**152**	9.8×10^{-4}	3	1875	760	731
#1168		Cr	5	**76**	9.9×10^{-4}	30	1930	380	363
#1177		Zr	8	**1280**	1.0×10^{-3}	30	2688	10240	9870
#1176		Zr	8	**800**	1.0×10^{-3}	30	2680	6400	4994
#1178		Zr	8	**480**	1.1×10^{-3}	30	2680	3840	3742
#1269		Zr	8	**320**	9.6×10^{-4}	30	2736	2720	2644
#1181		Zr	8	**160**	1.0×10^{-3}	30	2704	1280	1228
#1182		Zr	8	**80**	1.1×10^{-3}	30	2696	640	615
#1189	Rotation Speed	Cr	5	152	9.7×10^{-4}	**10**	1860	760	733
#1190		Cr	5	152	9.8×10^{-4}	**20**	1880	760	731
#1185		Zr	8	160	1.1×10^{-3}	**10**	2712	1280	1232
#1209		Zr	8	160	1.1×10^{-3}	**20**	2680	1280	1238
#1201	Argon Pressure (**55,140,200 sccm**)	Cr	5	152	**1.2×10^{-3}**	30	1705	760	735
#1202		Cr	5	152	**2.8×10^{-3}**	30	1508	760	730
#1260		Cr	5	152	**3.7×10^{-3}**	30	1505	760	736
#1206		Zr	8	160	**1.2×10^{-3}**	30	2584	1280	1236
#1272		Zr	8	160	**2.7×10^{-3}**	30	2200	1280	1231
#1273		Zr	8	160	**3.6×10^{-3}**	30	2200	1280	1234
#1184	Interrupted Deposition	Zr	8	**160**	1.1×10^{-3}	30	2680	1280	1235
#1183		Zr	8	**4x40**	1.1×10^{-3}	30	2696	1280	1189
#1182		Zr	8	**800**	1.0×10^{-3}	30	2672	6400	6178
#1179		Zr	8	**4x200**	1.0×10^{-3}	30	2680	6400	6178

Based on results from previous trails with the used coating machine it is expected that deposition temperature did not exceed 60°C during all of the experiments for this thesis. With the goal to design a stress free layer stack, promising parameter sets from the initial trails for Zr and Cr respectively were combined. The used combination ML 1 and ML 2 can be found in the following table.

Table 4. *Used film combination to produce a nearly stress free layer stack*

Batch	Sample Name	Material	Target Current [A]	Time [s]	Pressure [mbar]	RPM [1/min]	Target Power [W]	Aimed [As]	Realized [As]
#1262	ML 1	Cr	5	76	9.8×10^{-4}	30	1929	**380**	**362**
		Zr	8	6.5x160		30	2800	**8320**	**3860**
		Cr	5	76		30	1930	**380**	**350**
#1267	ML 2	Cr	5	76	9.45×10^{-4}	30	1930	**380**	**362**
		Zr	8	6.5x160		30	2800	**8320**	**5446**
		Cr	5	76		30	1925	**380**	**361**

To also gain knowledge about the influence of the base- and topcoat and their contribution to the residual stress in the whole system, the stress of the two lacquers were also determined. To do this, only the thickness of the base- and topcoat were varied, while all other process parameters were kept constant throughout the experiments.

Table 5. *Investigated thickness of base- and topcoat*

Material	Variable Parameter	Thickness [µm]
BC	Lacquer thickness	**5.8**
		10
		15
		20
		23
TC		**8**
		10
		14
		22
		25

3.3 Coating characterization

In the following section a short overview about the used measuring devices as well as used measuring setup is given.

3.3.1 Coating thickness measurement

For measuring the thickness of the coating in a fast way, one half of the microscope slide was covered with a conventional adhesive tape. Then, the coating was deposited, and the tape was removed after the process. This resulted in a step, which allowed to determining the film thickness.

The step measurement was conducted with the surface profile *Hommel-Etamic T8000 R* by the company *Jenoptik.* For the step measurement, the surface on the high and low ground where levelled. Per sample, a total of three measurements were conducted and the average was calculated.

For a more accurate value, the film thickness values were also measured while investigating the coating structure in the SEM. The used thickness value is the average of three measurements.

The thickness of the lacquer was measured with an optical spectrometer thickness gauge.

3.3.2 Coating hardness measurement

The coating hardness was measured with the *Universal Nanomechanical Tester (UNAT)* of the company *ASMEC* for the thickest samples of Cr and Zr respectively. The used load was 1 mN which was determined as a suitable load for such thin films from previous trails. A total of 30 measurements were conducted per sample. The measurements were analyzed with the software *InspectorX (Ver 3.1)* also from the company *ASMEC.* The used Poisson's ratio can be found in Table 1. The tangent for the force reduction curve was constructed in between 98-40% of the maximum force. To correct the measured hardness and elastic modulus of the thin films for the influence induced by the substrate, an algorithm included in the software *FilmDoctor®,* offered by the company *SIO® Saxonian Institute of Surface Mechanics* was used.

3.3.3 Stress determination by Stoney formula

For determining the coating stress by the Stoney formula, the coating induced curvature of the sample needs to be obtained. Since the delivered glass wafers were not completely flat, the initial curvature prior to coating deposition was determined. Because the

used surface profile measurement only yields a substrate deformation (height), it needed to be converted into a curvature value for determining the internal stress.

The deformation of the sample was measured with *a Hommel-Etamic T8000 R* surface profiler by the company *Jenoptik.* The measuring length was 47 mm and the sample was measured over the diameter under the angle 0°, 45°, 90° and 135°, as illustrated in Figure 19. The measured curve was levelled to zero in between 0-0.5 and 46.5-47.0 mm. The deformation was measured at the peak of the curve. The average of the measured values over the four diagonals was calculated.

After the deposition, the bending was measured along the same previously marked diagonals. The resulting difference in wafer deformation Δh (see figure below) of the pre- and post-deposition state was calculated. With the thickness values from the SEM the stress was calculated.

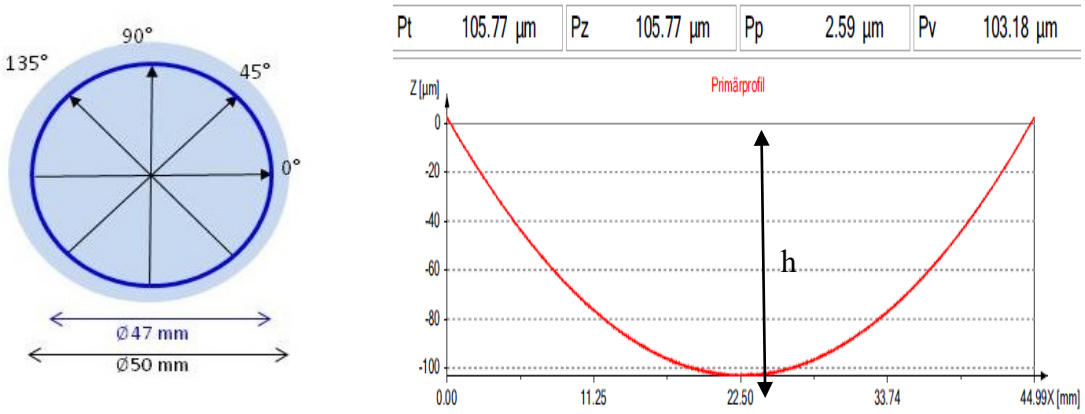

Figure 19. *Measuring routine of the glass stress measurement sample (left). Example of a wafer deformation measurement result conducted with a surface profiler. The letter h represents the used wafer deformation for calculating the stress by the Stoney formula.*

3.3.4 Coating structure investigation SEM

For a more precise determination of the coating thickness and to get an insight into the coating structure, the microscope slides were fractured. This was achieved by creating a crevice using a rotary tool equipped with a cutting disk. The vibrations during the cutting process lead to a sharp and well-defined fracture of the coating.

The samples were investigated with a Scanning Electron Microscope (SEM) *Leo Gemini 1530* from the company *Carl Zeiss.* The coating fracture cross-section to determine the coating thickness and structure, as well as a picture of the surface morphology, were both taken with the *InLens* Detector. The used working distance was between 3 and 5 mm. All pictures were taken with a 5 kV acceleration voltage. Prior of the SEM investigation, the samples were coated with a thin layer of platinum for making them conductive and avoid charged built-up.

3.3.5 XRD analysis

The measurements for lattice parameter, texture and grain size were conducted by X-Ray Diffraction (XRD) in a conventional θ/2θ setup with a scan range of 2θ =30 to 80° with a 0.02° step-size and 2 seconds per step. The used *Bruker D8 Advanced* was set to a cathode voltage of 40 kV and a cathode current of 30 mA. The characteristic K_α X-Ray spectra generated by the Cu Anode contain fractions of $K_{\alpha1}$ and $K_{\alpha2.}$ $K_{\alpha1}$ has twice the intensity than $K_{\alpha2}$ and with 1.5060Å compared to 1.54439Å also a shorter wavelength. The measuring programs were created with *XRD Wizard* (*Ver. 2.9.0.22, Bruker AXS*). The spectra were investigated with the software *DIFFRAC.EVA* (Ver. 4.2.1.10, *Bruker AXS*). For the qualitative phase analysis, the integrated Powder Diffraction File (PDF) Database *PDF-2-2004* and *Crystallography Open Database* (*REV173445 2016.01.04*) was used. Texture analysis was conducted with *DIFFARC.TEXTURE (Ver.3.1.10, Bruker AXS)*

The XRD was equipped with a *Xenocs FOX 2D 12_INF* optics, a parallel plate collimator, an energy dispersive detector and an Eulerian cradle, which allows rotation and titling of the sample. The instrumental aberrations, which is present during sample tilting and interferes with proper diffraction analysis, can be avoided by the two dimensional highly parallel X-rays, provide by the used optics. In order to verify that instrumental aberrations do not occur when tilting of the sample for stress or texture analysis, the strain of a stress-free α-Al_2O_3 plate (*NIST standard reference material SRM 1976a*) was measured. It could be verified that the instrumental aberrations does not have to be considered during the stress measurements (Result of measurement on stress-free Al_2O_3 can be found in the Appendix 1)

The stress measuring programs used a 0.02° step size with a 2 s dwell time per step and a 5° tilting step for the Eulerian cradle. The determination of the peak position and the peak shift was accomplished by fitting the XRD curves with the *Pearson VII* function in the Software *Topas* (*Ver. 5.0, Bruker*). For each fitting procedure, 15 iterations were conducted. If the function converged sooner, the fitting procedure was stopped. The $K_{\alpha2}$ wavelength was subtracted automatically by the software.

Since the film thickness is quite small, additionally to the conventional $\sin^2\psi$ the $\cos^2\alpha\sin^2\psi$ method was applied. This method was not yet established at the analytics laboratory of Oerlikon Blazers and was thus introduced as a part of this thesis. Tests were run for different samples to verify the validity of this method (see Appendix 1 for the stress free Al_2O_3 sample). This technique allows fixing the penetration depth at a certain film thickness with a fixed grazing incident angle. The angle α is the derived from $\alpha = \gamma - \theta_0$ where γ represents the grazing incident angle and θ_0 the diffraction angle. The penetration depth of the film was estimated with the formula (17) presented in [70] with the usage of the linear absorption coefficient for Zr and Cr by the values of

843 cm^{-1} and 1788 cm^{-1} respectively. Those constants were calculated with the datasets of X-Ray Mass Attenuation Coefficients, available from the NIST Webpage [81]

$$\tau_{63} = \frac{1}{\mu k_\alpha} = 1\frac{\sin\alpha \sin(2\theta-\alpha)}{\mu(\sin\alpha+\sin(2\theta-\alpha))} \qquad (14)$$

The used grazing incident angle of 2°results in a penetration depth of 200 nm when measuring at the (110) Peak at of chromium (PDF-85-1336 [82]) and 400 nm when measuring at the (100) peak of zirconium(PDF-34-0657 [83])

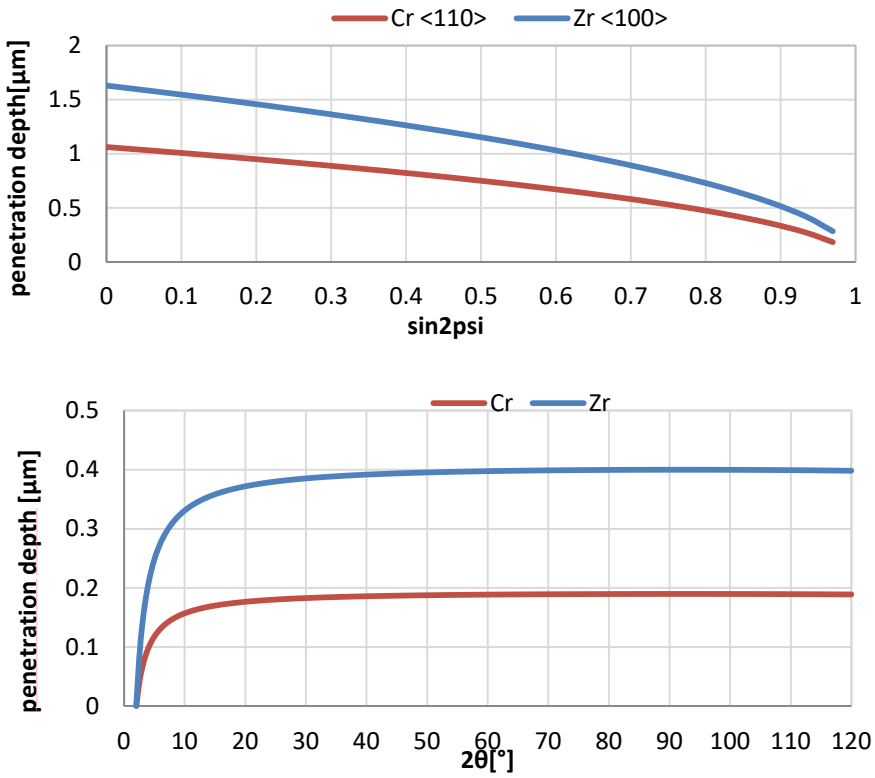

Figure 20. *Calculated penetration depth in dependence of the peak position for the 2θ setup (top) and for the GI 2° setup (bottom).*

The plotting of the d vs. sin2ψ or d vs. $\cos^2\alpha\sin^2\psi$ plot was accomplished with the spreadsheet Software *Origin (Ver. 7.5, OriginLab)*. Evaluation of the plots was carried out according to the procedure mentioned in the theory section.

The used XECs s_1^{hkl} and $^1/_2\, s_2^{hkl}$ were calculated based on single crystal data sets from literature. The used XEC values can be found in the following table. Macroscopic XEC were calculated based on results obtained from the nanoindentation experiments for the thickest films, denoted by the source *NI*. The XECs based on calculations from single crystal datasets were calculated with the Software *DECcalc*. The difference in stress result based on the difference XECs is discussed later on.

Table 6. *Used XEC for XRD stress calculation*

Material	XEC#	Source	Peak	E_{ISO} [GPa]	μ	S_1 [1/MPa]	$^1/_2 S_2$ [1/MPa]	E_{110} [GPa]
Cr	XEC 1	[84]	110	277	0.21	-7.95E-7	4.48E-6	271
	XEC 2	[85]	110	320	0.27	-9.01E-7	4.11E-6	311
	XEC 3	NI	-	126	0.21	-	-1.00E-5	-

A problem which one needs to keep in mind is that with the used copper source the signal from the chromium layer will contain fluorescents artifacts. This might negatively influence the curve fitting for the stress analysis, mainly due to a poor peak-to-background ratio.[62]

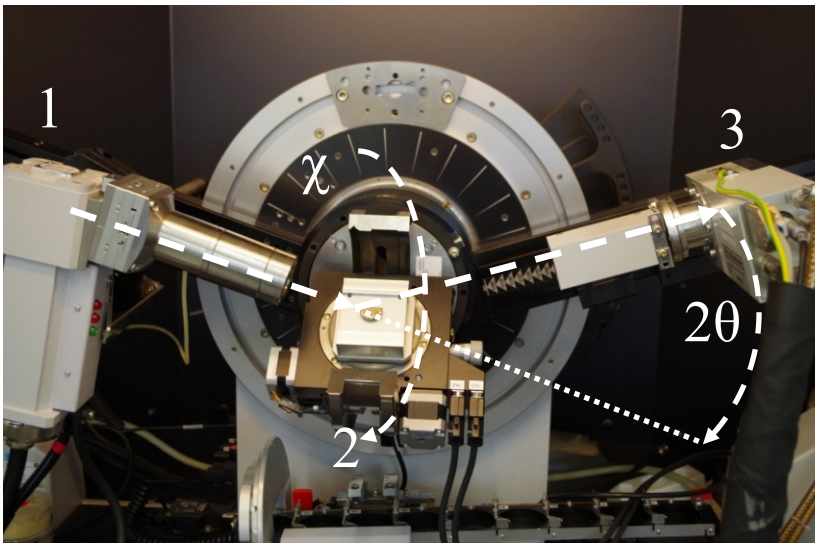

Figure 21. *Picture of the used XRD Setup with the indicated key components: 1. X-Ray Tube 2. Eulerian cradel, 3. X-Ray Detector and the measuring angle 2θ*

To determine the crystalline size by the Scherrer equation, the instrument contribution for the peak broadening is needed. This instrumental contribution was set to 0.171°, as measured with Lanthanhexaborid (LaB_6) for an angle at 43.5°, which is the closest to the (110) peak measured for chromium.

The texture measurements were conducted with 5° step size around the phi axis (0-360°) and a 10° step size along the chi tilting angle (0-80°) with a step time of 6 seconds. The peak position for fixing the 2θ angle was acquired from the Bragg Brentano scan.

4. RESULTS

In the following section, the results of the research done for this thesis are presented. For the purpose of keeping the results section easy to read, results which were considered not so important are attached in the appendix.

4.1 Coating thickness

As mentioned in the previous chapter, the coating thickness was measured by a step measurement utilizing a surface profiler and via SEM cross-section fracture. Whereas the first method is very fast, the SEM is considered to be the more accurate method, but needs more preparation and measuring time. A comparison of the two methods applied to a thick chromium film is presented Figure 22. It does not show a significant difference between the two methods. This becomes also clear, considering the graph beneath were the aimed thickness values as well as the measured thicknesses via SEM and step measured are depicted. It is apparent that the measured values do not show a big difference within one sample; however, the initial aimed thickness is sometimes not achieved. Furthermore, the thin coatings sometimes were not possible to be measured with the step method, due to a lack of a distinguishable signal.

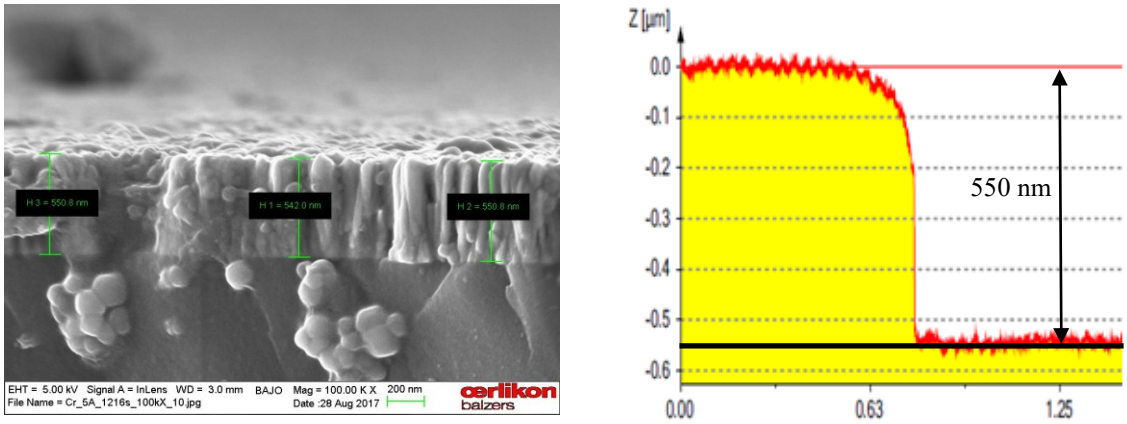

Figure 22. *Example of PVD Coating Thickness Measurement. Sample measured with the SEM (left) and by the step measurement using a surface profiler (right). Both results show almost similar values of around 550 nm.*

To be able to deposit coatings with an exact coating thickness, the used realized sputtering time was plotted against the measured coating thickens by SEM. This graph, as well as the linear fit function for both materials is shown below.

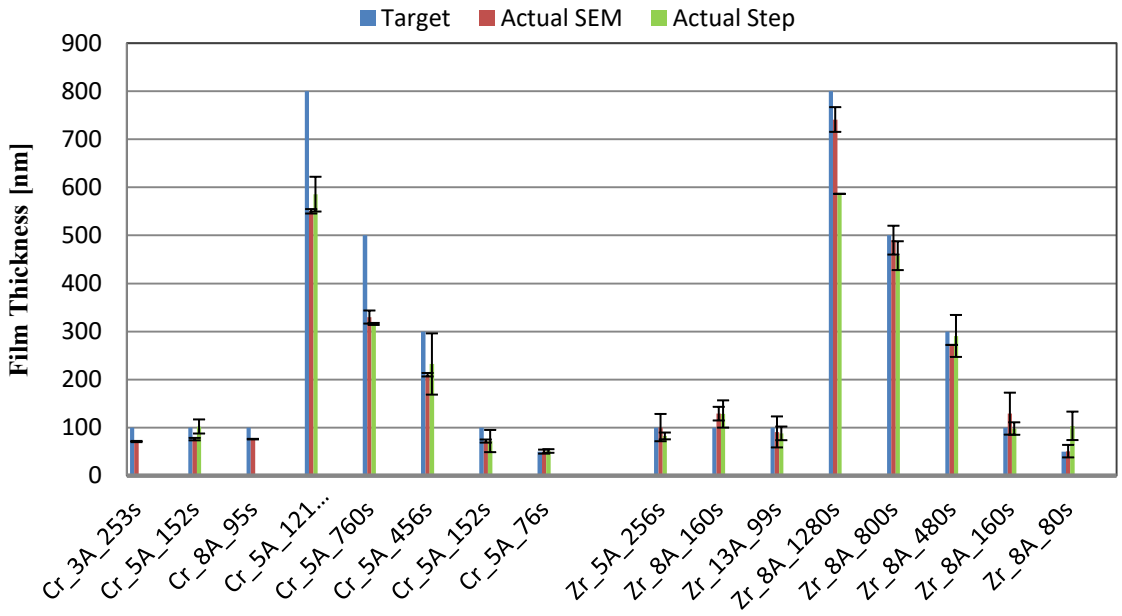

Figure 23. *The averaged results of 3 measurements of both thickness measurements methods in comparison, for both Cr and Zr. The standard deviation of the results inis indicated by the error bars.*

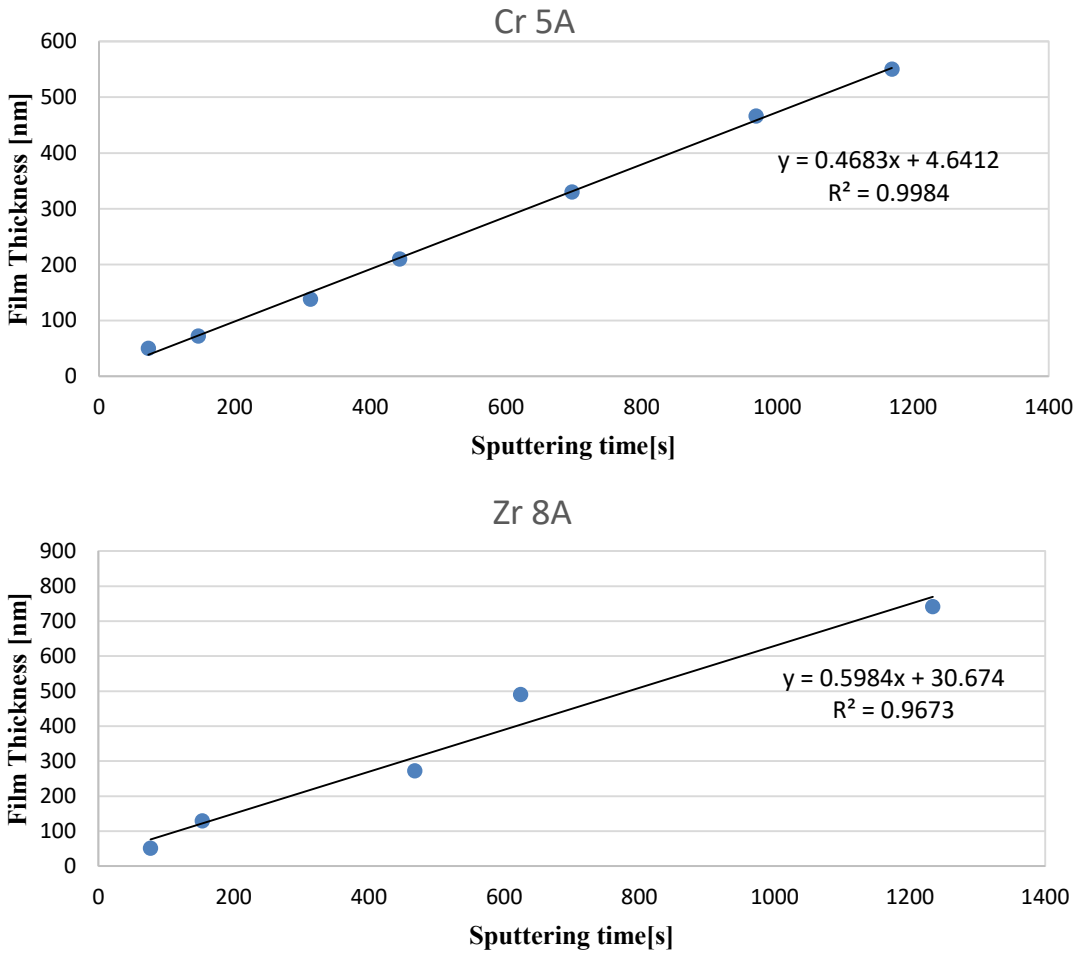

Figure 24. *Sputter time vs. film thickness diagram. Relationship for Cr sputtered at 5A, 1.0 x 10^{-3} mbar (top). Relationship for Zr sputtered at 8A, 1.0 x 10^{-3}mbar (bottom).*

4.2 Coating hardness

The normal force / normal displacement curves for a thick chromium film (Cr-5A-1216s) is shown below. To account for a substrate influence which can be present if the penetration depth exceeds the 10% rule (penetration depth < than 10% of film thickness) the results were corrected with a correction algorithm. The comparison of the measured values for hardness and Elastic Modulus via classic Oliver and Pharr, H_{OP} and E_{OP} and the corrected values by the *Filmdoctor* Software H_{FD} and E_{FD} can be found in Table 7. For chromium, the corrected values for hardness and elastic modulus are 19% and 29% higher respectively. For zirconium, the substrate correction increased the values for both properties only around 3%.

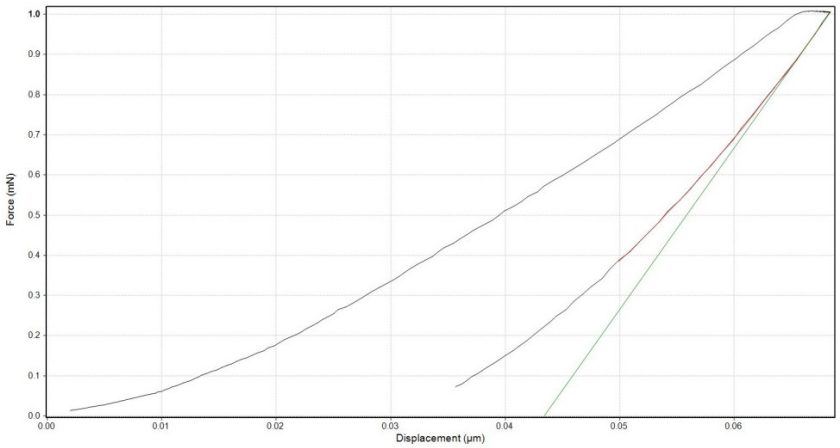

Figure 25. *Example of a Force-Displacement curve of the measured chromium film with 1 mN.*

Table 7. *Results of Hardness Measurement and Corrected Results by FilmDoctor® Software*

Material	H_{OP} [GPa]	E_{OP} [GPa]	H_{FD} [GPa]	E_{FD} [GPa]	H Diff [%]	E Diff [%]
Cr	6.9	90.0	8.5	126.5	19	29
Zr	4.9	79.9	5.05	81.8	3	3

4.3 Stress by substrate bending

To calculate the residual stress by the Stoney equation, the total bending induced by the coating needs to be determined. Due to a limitation of available substrates, only one substrate per coating process was used, which does not allow for any statistic for the residual stress results. However, to evaluate the repeatability of the method, the bending was determined by coating two different substrates with different initial curvature in the same process. The total bending after the deposition of the coating was compared. The results can be seen below. The difference in curvature is around is 1.6 %.

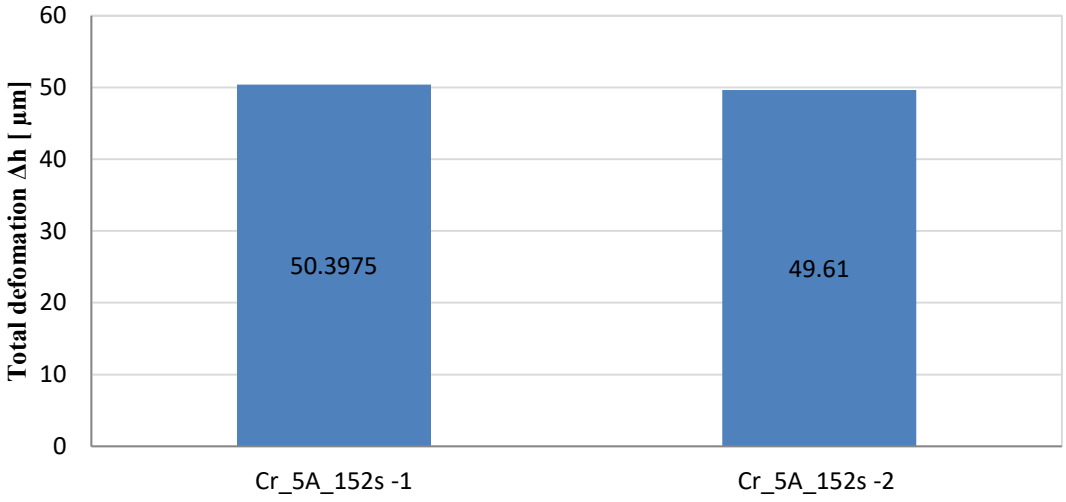

Figure 26. *The Diagram shows the repeatability of the curvature measurement. The different stress measurement disks show the same deformation after the same coating*

Influence of coating thickness on coating stress

As shown in Figure 27, the residual stress for Cr shows a sharp increase in residual tensile stress from 907 MPa for the 50 nm coating to 1456 MPa for the 72 nm thick coating. After this initial increase, the tensile stress declines with increasing coating thickness. For thicker coatings, the decline in residual tensile stress decreases further. Multiplying the calculated residual stress by the measured coating thickness results in Force per unit width (F/w). This dependency is shown in Figure 28 and shows that the thin coatings exert less force than the thicker coatings, which results in an inverse dependency with the coating thickness, compared to the residual stress.

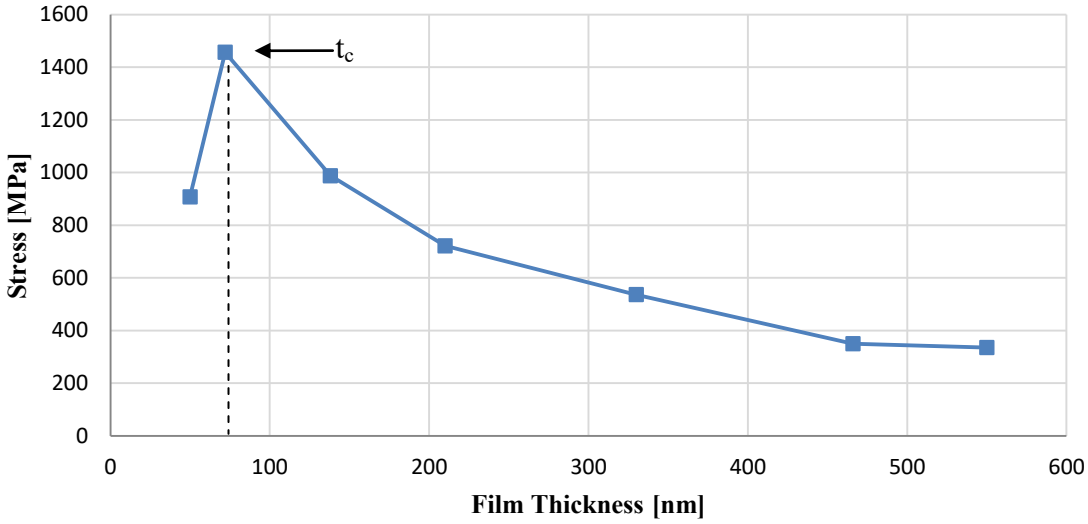

Figure 27. *Influence of coating thickness on residual stress of Cr deposited with 5A at 1 x 10^{-3}mbar. After and initial increase the stress drops again for thicker film. The point at which the direction of the stress development changes is marked with the critical film thickness t_c.*

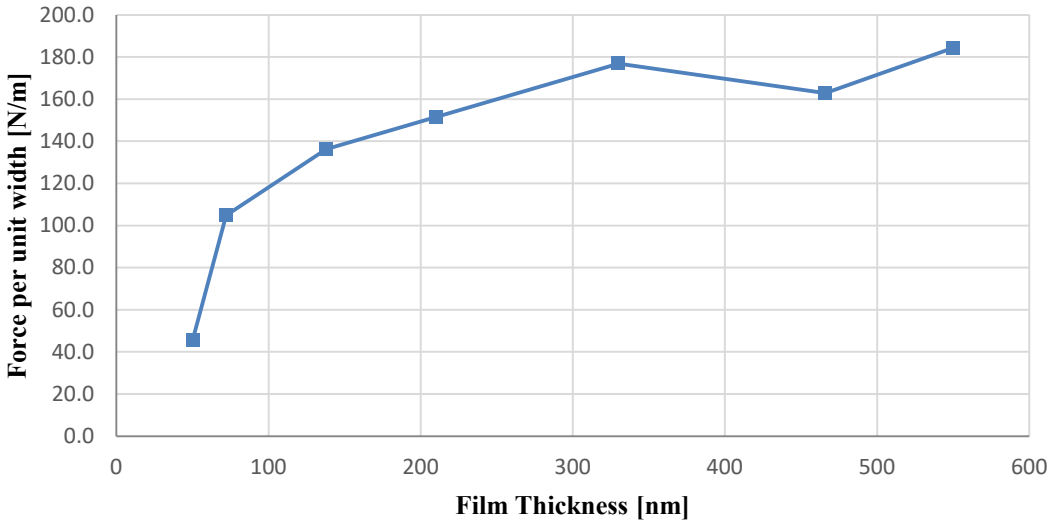

Figure 28. *Influence of coating thickness on N/m of Cr deposited with 5A at 1 x 10^{-3} mbar. An increase in the force per unit width with the thickness is observable.*

Contrary to chromium, zirconium does not show any particular trend for a dependency residual stress with the coating thickness. However, an overall observation is a higher compressive stress for the thin coatings and a less compressive stress for the thicker coatings. The resulting Force per unit width dependency is also shown below and also does not show any clear trend with the film thickness. If one compares the max and min values exerted force over the whole range of film thickness with the force per unit width of the chromium film, one sees that the chromium film exerted around 4 times more force in term of magnitude, than the zirconium.

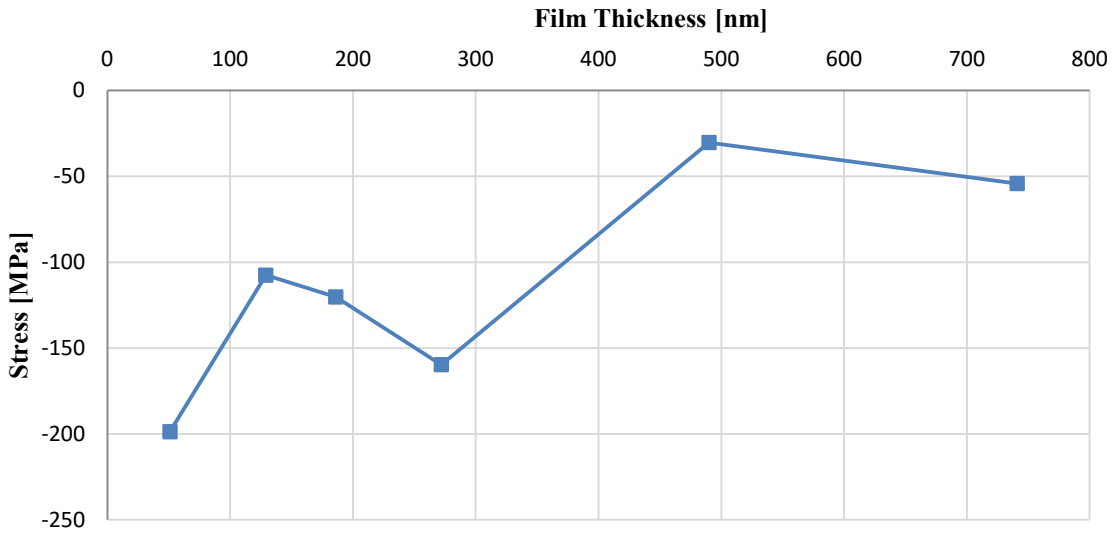

Figure 29. *Influence of coating thickness on residual stress of Zr deposited with 8A at 1 x x 10^{-3}mbar. Zr shows compressive stress which overall decreases with the film thickness.*

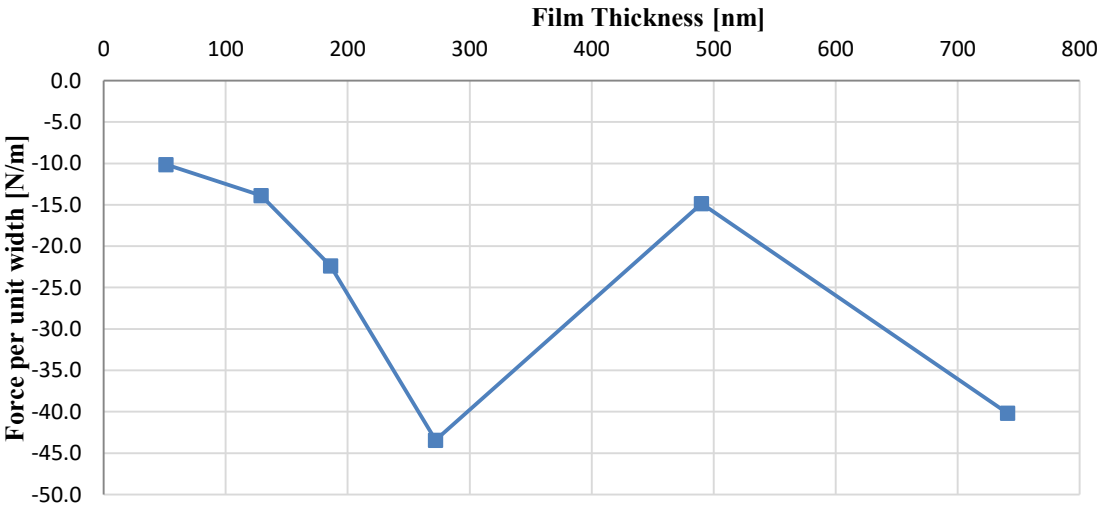

Figure 30. *Influence of coating thickness on N/m of Zr deposited with 8A at 1 x 10^{-3} mbar. After an initial increase in the compressive force until ≈270 nm the force decreases again.*

Influence of target current on coating stress

Chromium shows an increase in tensile stress from 875 MPa at 3A to 1404 MPa at 8A while keeping the coating thickness constant.

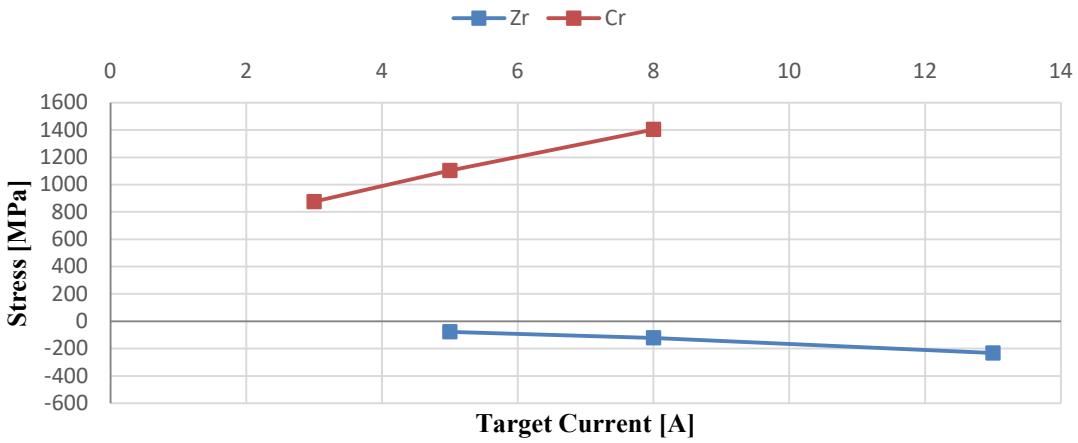

Figure 31. *Influence of target current on residual stress of Cr and Zr deposited with a constant coating thickness. Cr shows an increase in tensile stress whereas Zr shows in increase in compressive stress with increasing current.*

Zirconium at the same time shows an increase in compressive stress from -78 MPa at 5 A to -232 MPa at 13 A while keeping the coating thickness constant. Since the coating thickness was kept constant, the resulting force per unit width dependency shows the same trend as the residual stress. Comparing the exerted force for the film deposited with the low target current of chromium and zirconium, one can see that chromium exerts around 8 times more force than zirconium. For the other two target currents, chromium shows roughly a 5 times higher exerted force.

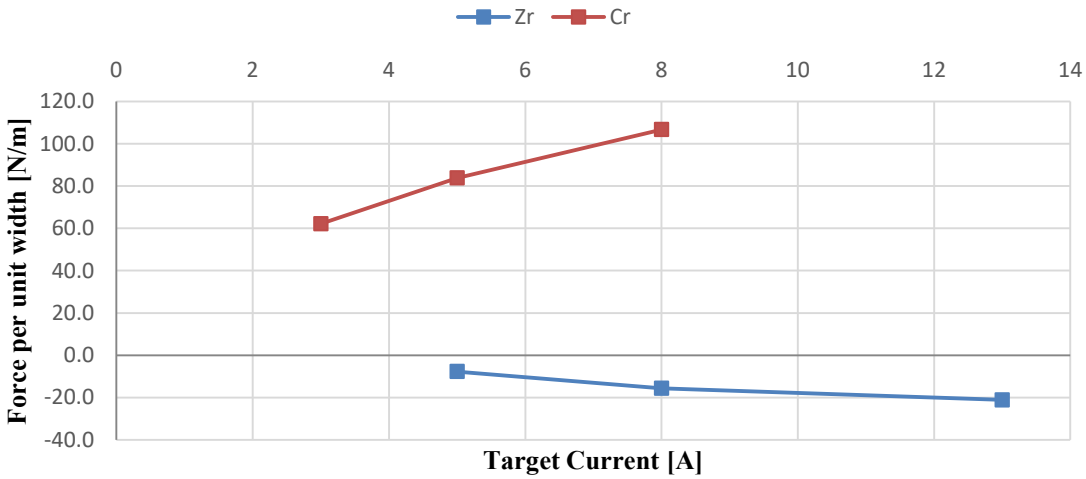

Figure 32. *Influence of target current on N/m of Cr and Zr deposited with a constant coating thickness. Cr shows an increase in tensile force whereas Zr shows in increase in compressive force with increasing current.*

Influence of Argon flow/sputtering pressure

The argon flow for depositing chromium and zirconium was set to 55, 140 and 200 sccm. This resulted in argon pressures of 1.18 E-3 mbar, 2.7 E-3 mbar and 3.75 E-3 mbar respectively. For chromium, a decrease of residual stress from 1136 MPa for 55 sccm to 919 MPa for 140 sccm can be observed in the graph below. A further increase of the argon flow to 200 sccm, results in a decrease in tensile stress of around 390 MPa.

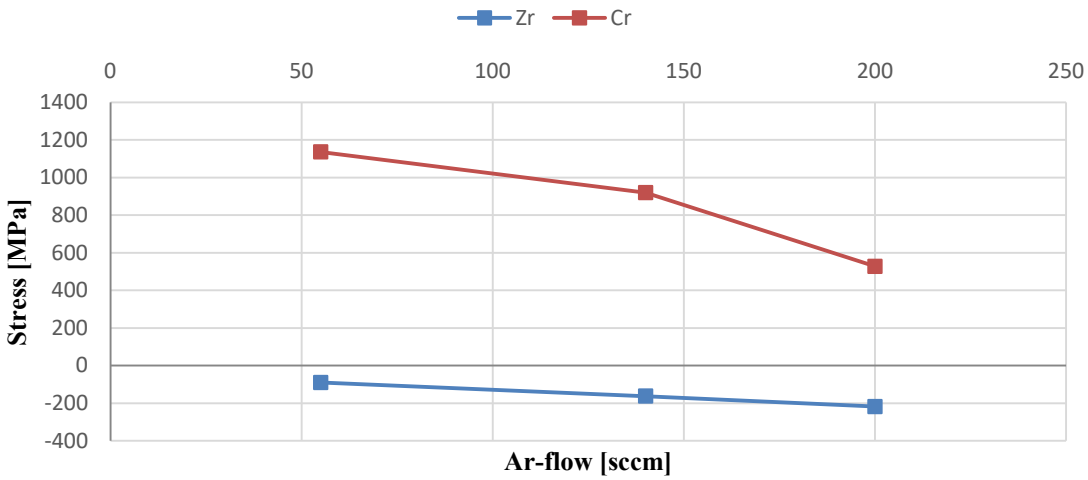

Figure 33. *Influence of argon flow on residual stress of Cr and Zr. Both show and decease in tensile stress/increase in compressive stress with an increasing argon flow.*

For zirconium, a decrease in the residual compressive stress of -90 MPa for 55 sccm to -162 MPa for 140 sccm was observed. Further increasing the argon flow to 200 sccm increases the compressive stress to -218 MPa. Both, Cr and Zr show an almost linear decrease of tensile /increase compressive force (N/m) for with the argon flow.

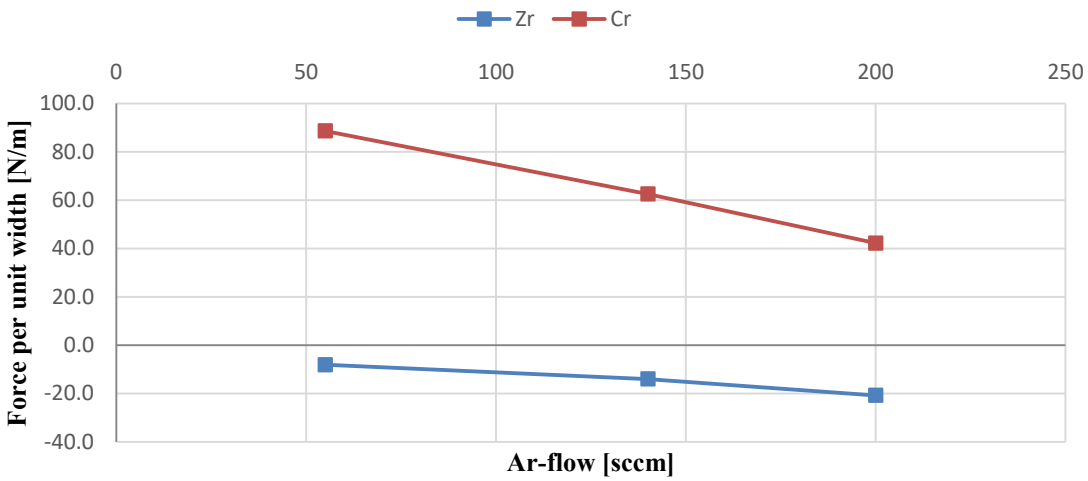

Figure 34. *Influence of argon flow on F/w of Cr and Zr. Both show and decease in tensile force/increase in compressive force with an increasing argon flow.*

Influence of substrate rotation

For chromium, the highest amount of residual tensile stress is found at a rotation of 20 rpm with 1793 MPa. For a set rotation speed of 10 and 30 rp,m the residual tensile stress is found at values with 990 and 1100 MPa respectively as can be seen from the figure below. As one can see from there, zirconium shows no significant change in residual stress with a change in rotation.

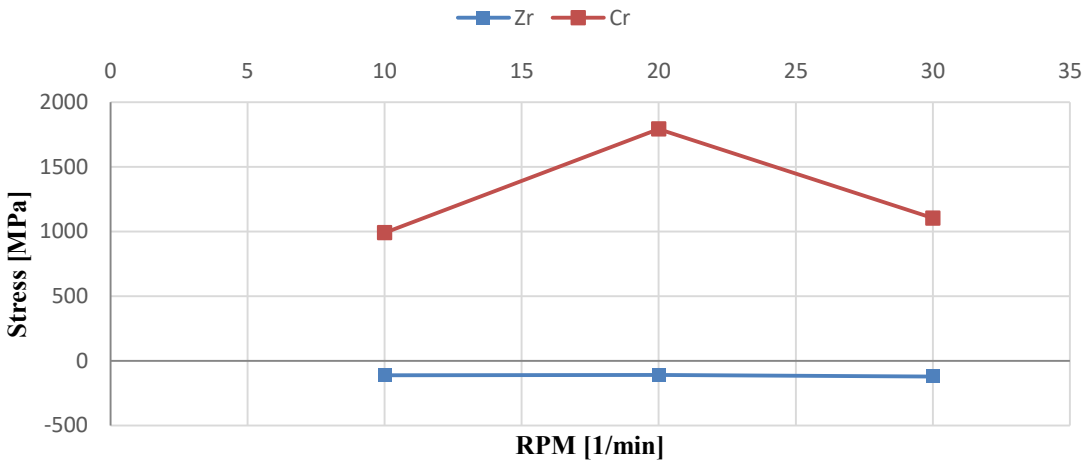

Figure 35. *Influence of substrate rotation on residual stress of Cr and Zr. Cr shows a peak for 20 rpm whereas Zr does not show any significant change in stress with a change in rotation speed.*

The dependency of N/m in relation to a change in the substrate rotation speed for both materials can be seen in Figure 36. This shows no obvious change with a change in rotation speed.

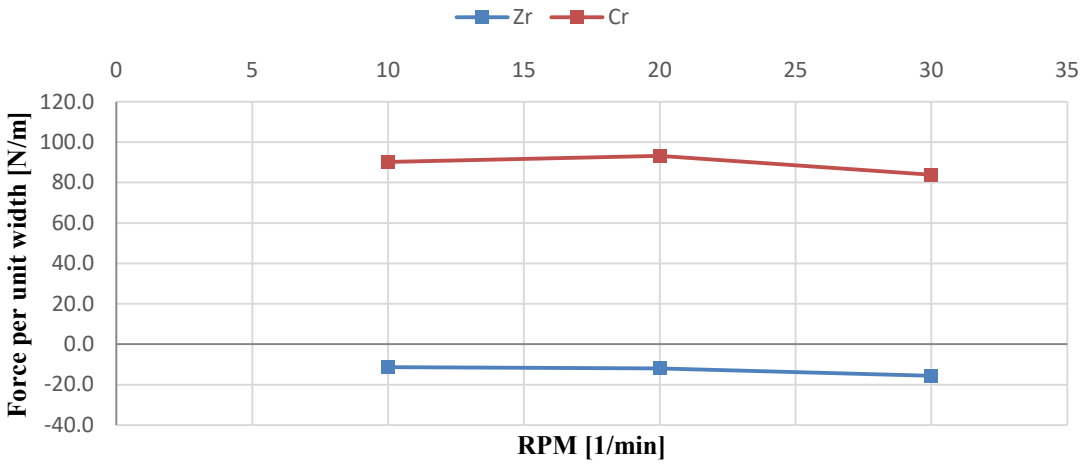

Figure 36. *Influence of substrate rotation N/m of Cr and Zr. No obvious change in F/w with a change in rotation speed can be observed.*

Influence of interrupted deposition

For the thin variation of the interrupted deposition, there is no difference visible for the residual compressive stress compared to the coating deposited in one single cycle, as is evident when looking at Figure 37. The measured stress show values of -105 MPa for the interrupted deposition compared to -110 MPa for the coating deposited in one single cycle. Since the coating thickness is the same for both films, there is also no difference in the force per unit width.

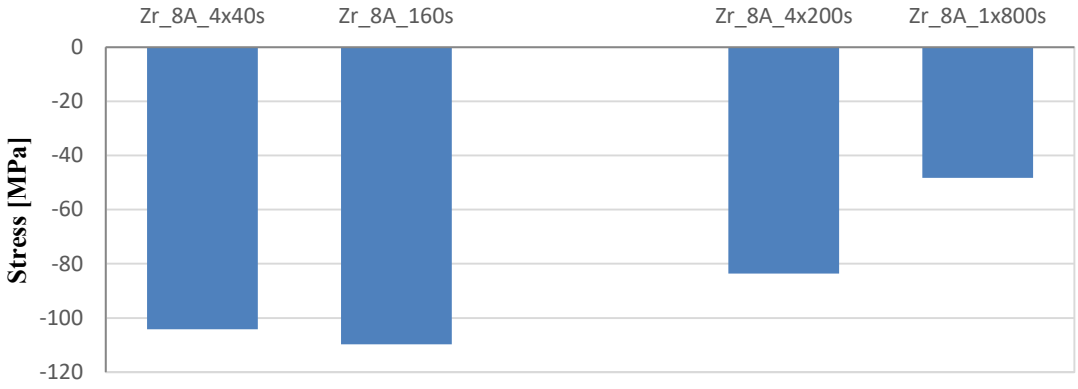

Figure 37. *Influence of interrupted deposition on residual stress of Zr deposited at 8A for 160 (left) and 800s total deposition time (right). Whereas the thinner film is not affected by an interrupted deposition, the thicker film shows a compressive stress which is almost 2 times higher than the one of the single deposition film.*

Contrary to the thin coating, the thicker variation shows -84 MPa for the interrupted deposition and -48 MPa for the continuous deposition. This is a change of 43%. Since the coating thickness is the same for both films, the similar difference is found for the force per unit width.

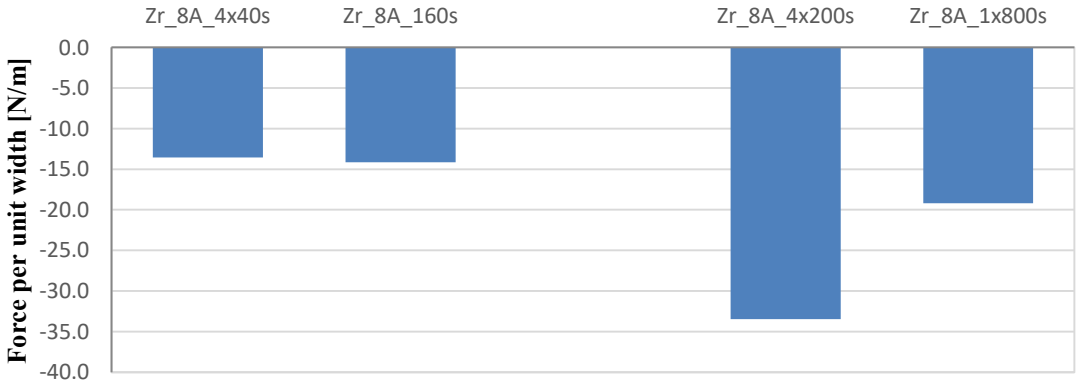

Figure 38. *Influence of interrupted deposition on N/m of Zr deposited at 8A for 160 and 800 s total deposition time. The same relationship which can be seen in Figure 37 is also present for the F/w, since the film thickness is the same for the interrupted and the film deposited in one run.*

Influence UV lacquer thickness on residual stress

In Figure 39 it can be seen that, after an initial raise from 8.8 to 11.6 MPa, the stress of the basecoat declines again and seems to be somewhat constant after 20 µm with a value around 7.5 MPa. The topcoat on the other side shows a constant linear declined with the thickness and also seems to plateau from around 22 µm onward at around 2.6 MPa.

Considering the force per unit width in Figure 40, it is evident that the basecoat shows a significant increase with the thickness, whereas the topcoat exhibits a plateau in between 10 and 22 µm of around 55 N/m. Overall, the basecoat exerts more than 2.5x the force for lacquers thicker than 10 µm, compared to the topcoat.

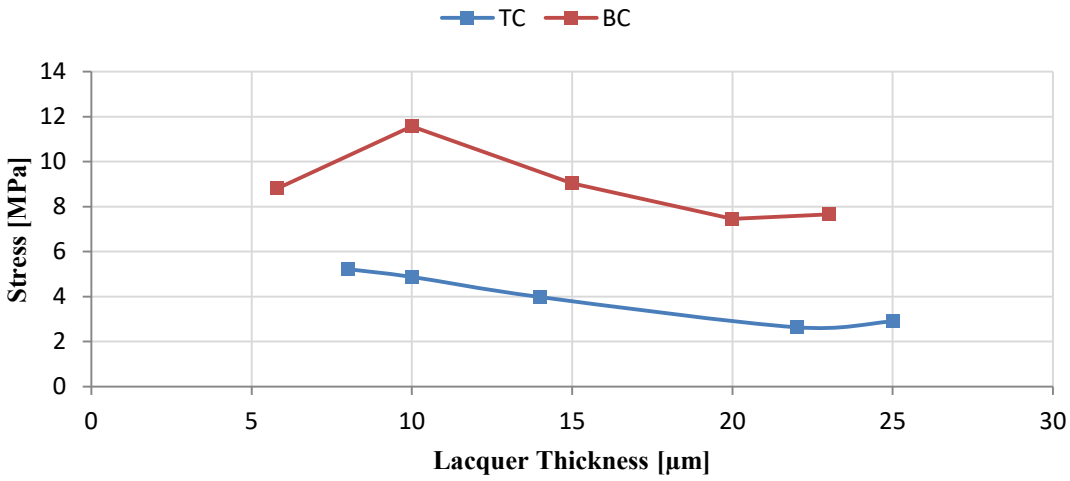

Figure 39. *Dependency of stress for basecoat (BC) and topcoat (TC) in relation to its thickness. Both lacquers show tensile stress. The topcoat however shows lower tensile stress.*

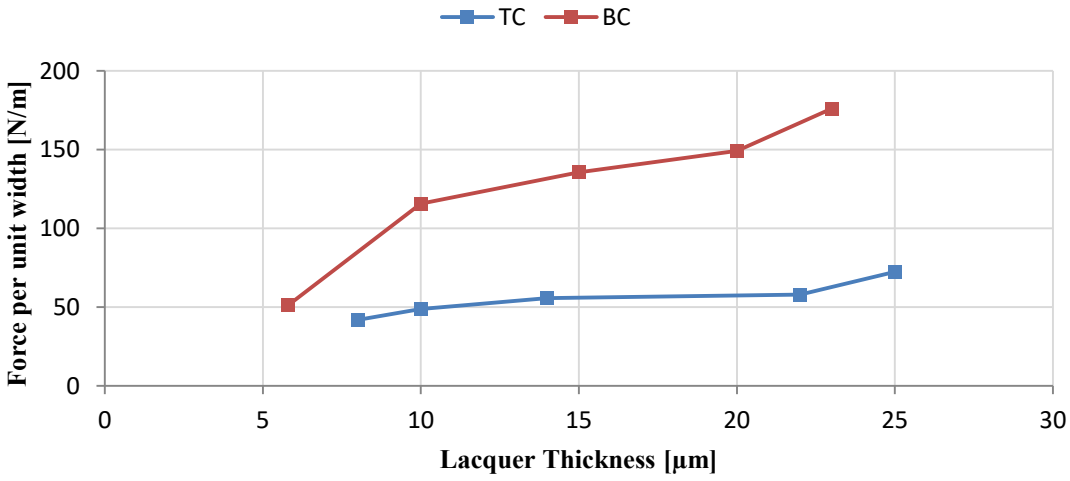

Figure 40. *Dependency of N/m for basecoat (BC) and topcoat (TC) in relation to its thickness. The basecoat exerts more than 2.5x the force for lacquers thicker than 10 µm, compared to the topcoat. The TC exhibits a force plateau between 10 and 23 µm*

4.4 Coating structure and surface morphology by SEM

In this section, the results of how the different process parameters are affecting the coating structure and coating morphology are shown.

4.4.1 Coating structure

In general, chromium shows a crystalline film structure in the fracture cross-section. The structure itself is columnar-like, and has a fine grain appearance. With an increase in film thickness, the structure becomes more distinguished, as can be seen by comparing the pictures in Figure 41.

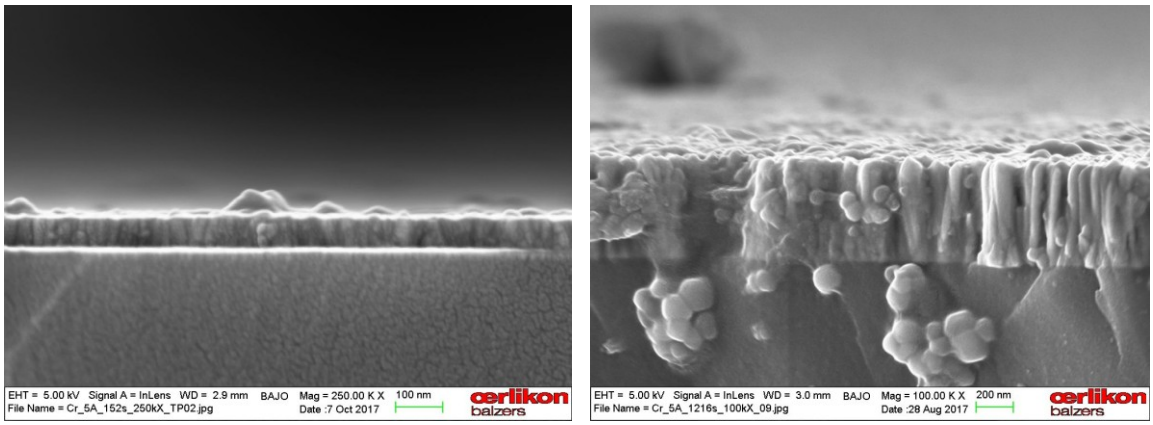

Figure 41. *Coating structure of a thin Cr film deposited at 5A for 152 s (left) and a thick coating deposited at 5A for 1216 s (right). Both films show a columnar like structure.*

Zirconium on the other hand exhibits no defined fracture structure for the thinner films, as can be seen in Figure 42. Thicker films deposited at times longer than 480 s show a more defined structure. However, it is not as distinguished as observed for the chromium films. Here the initial one-third of the coating seems to have a different structure than the rest of the film. The thickest zirconium film, deposited at 1280 s Figure 42, (right) shows a transition from a non-distinguishable structure over a coarse one to a very dense/ amorphous looking part at the top of the film.

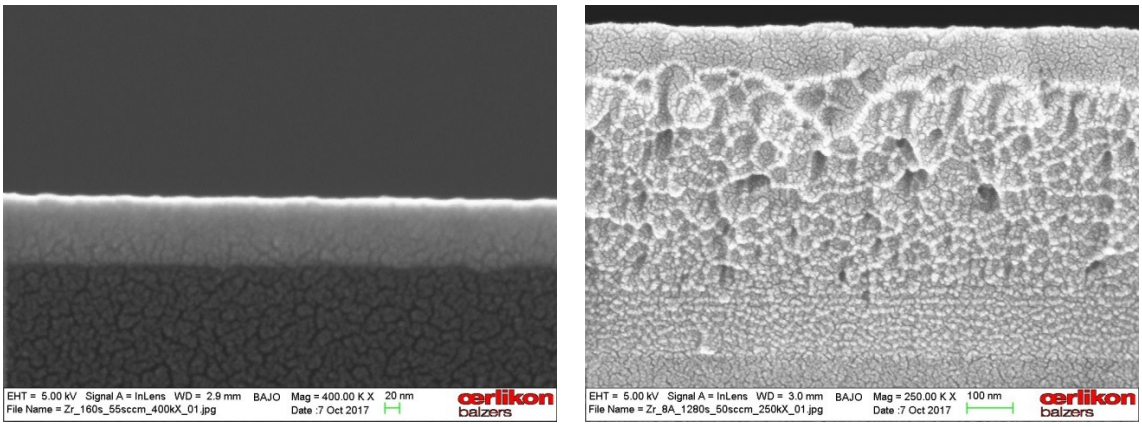

Figure 42. *Coating structure of a thin Zr film deposited at 8A for 160 s (left) and a thick coating deposited at 8A for 1280 s (right). The thin films shows a amorphous structure whereas the thicker film exhibits a evolution from a amorphous like structure close to the substrate to a crystalline one with the thickness.*

Both, Cr and Zr do not show a visible change in film structure with raising the target current (see Figure 43 in comparison to Figure 41 and Figure 42)

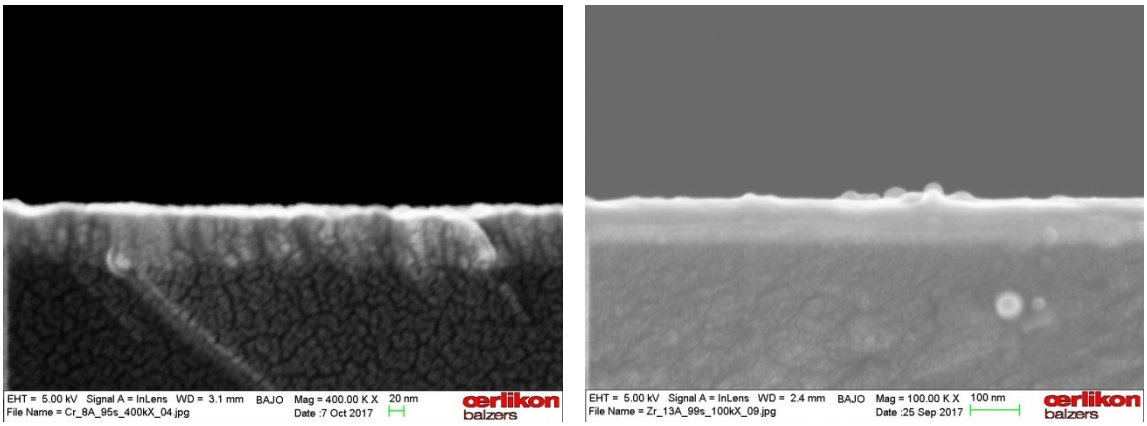

Figure 43. *Coating structure of the Cr film deposited at 8A for 95 s (left) and the Zr, coating deposited at 13A for 99 s (right).In comparison to the structure which can be observed for lower target current in the pervious figures, no change in structure can be observed.*

The change in argon flow from 55 sccm over 140 sccm to 200 sccm seems to change the fracture morphology of the film from crystalline to less crystalline. However, this change is not very distinct. The facture structure of zirconium does not seem to be affected at all by the change in the argon flow. Considering the influence of the substrate rotation the structure does not seem to be affected for either Cr or Zr.

4.4.2 Surface morphology

The surface morphology of chromium shows always a needle-like appearance. For the thinner films, the needles show a random orientation distribution. With an increase in the thickness, the needle size increases and they show a preferred orientation, as can be seen in Figure 44. The film structure for the thinnest film is somehow hard to distinguish.

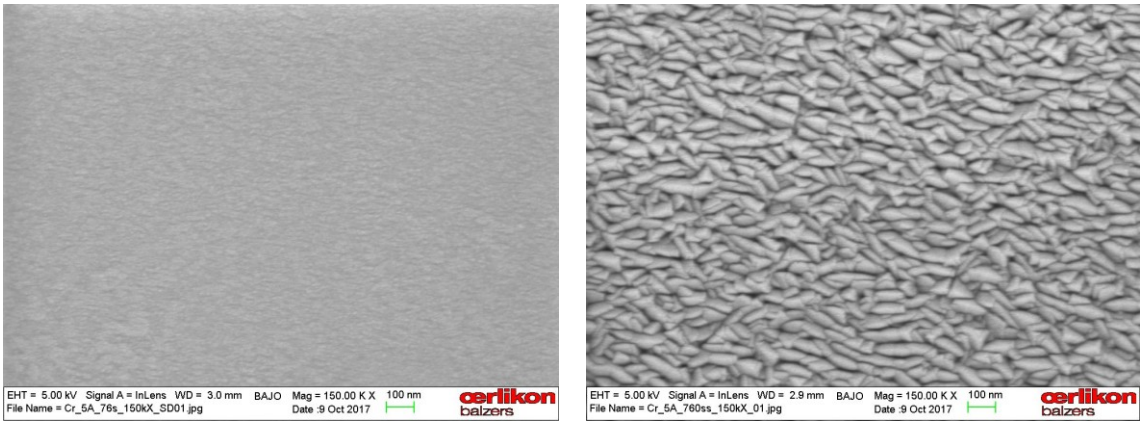

Figure 44. *Surface morphology evolution from the thin Cr film (left) to the thick Cr film (right). The thin film shows no clear morphology whereas the thick film shows a meddle like morphology with a preferential orientation of the needles.*

As one can see in Figure 45, the initial morphology of the thin zirconium film shows a somehow undefined structure. This structure becomes more round shaped with thickness and finally evolves into a cauliflower looking structure for the thickest film.

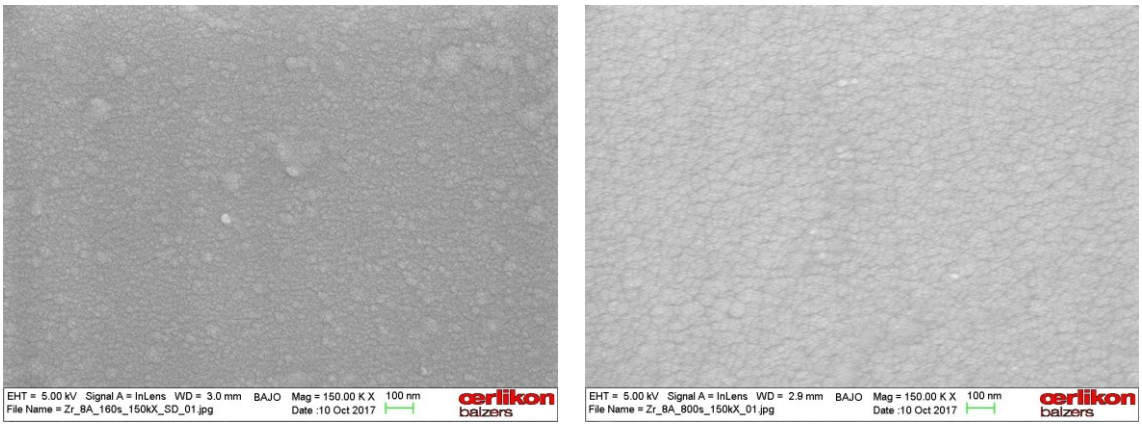

Figure 45. *Surface morphology evolution from the thin Zr film (left) to the thick Zr film (right). The thin film shows a fined grained morphology whereas the thick film shows a more coarse grained, cauliflower-like looking morphology.*

The target current, (see Figure 46 and Figure 47) changes the surface morphology the chromium films from a seemingly undefined structure for 3 and 5 A to a needle-like structure at 8A. Contrary to this, the shape of zirconium grains does not seem to be influenced by the target current. However, it seems that the grains of zirconium tend to get finer by increasing the current.

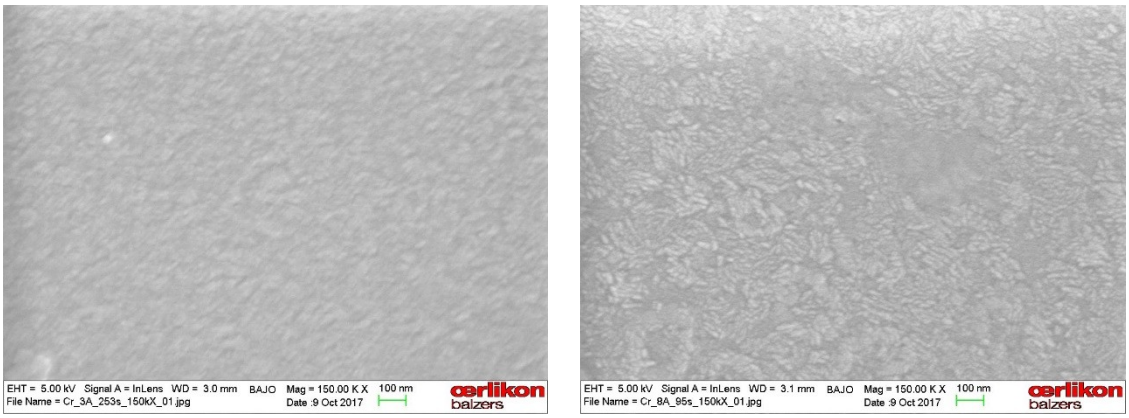

Figure 46. *Evolution of the surface morphology of Cr film with the target current. An increase of the target current of 3A (left) to 8A (right) changes the structure from an undefined to a needle like structure.*

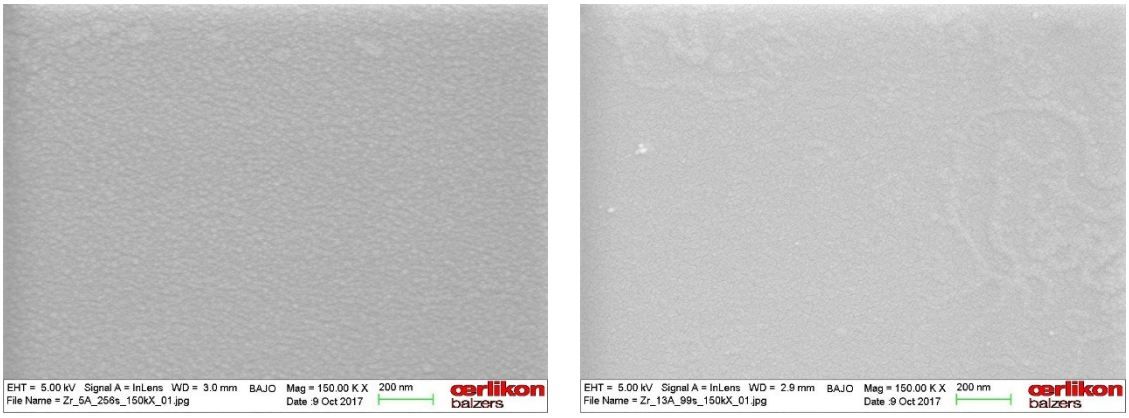

Figure 47. *Evolution of the surface morphology of Zr film with the target current. An increase of the target current of 5A (left) to 13A (right) changes the structure of Zr from an coarse grained to a fine grained structure.*

For the chromium film, an increase in argon flow changes the morphology from a fine, needle-like structure to more dense looking structure with bigger needles/grains. For zirconium, no obvious changes in surface morphology were observed. Also for the substrate rotation, no change in the morphology is visible for either Cr or Zr.

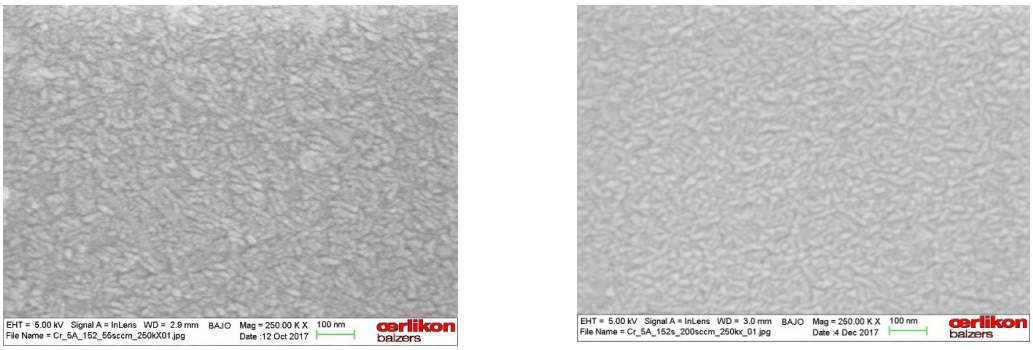

Figure 48. *Evolution of the surface morphology of Cr film with the argon flow from 55 sccm (left) to 200 sccm (right).*

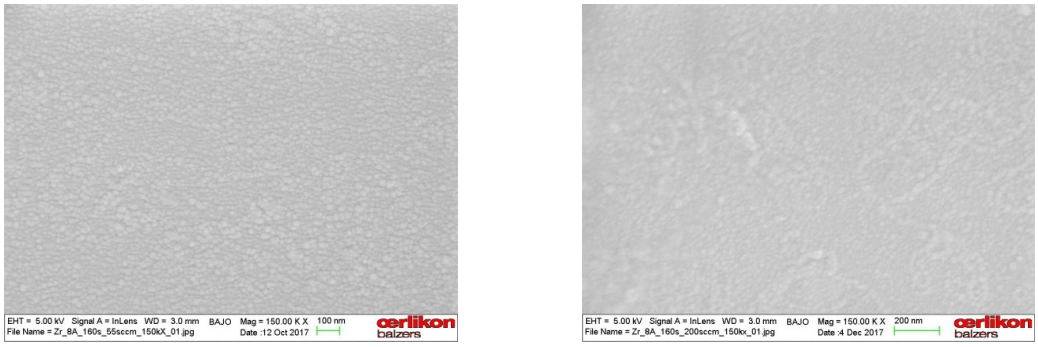

Figure 49. *Evolution of the surface morphology of Zr film with the argon flow from 55 sccm (left) to 200 sccm (right)*

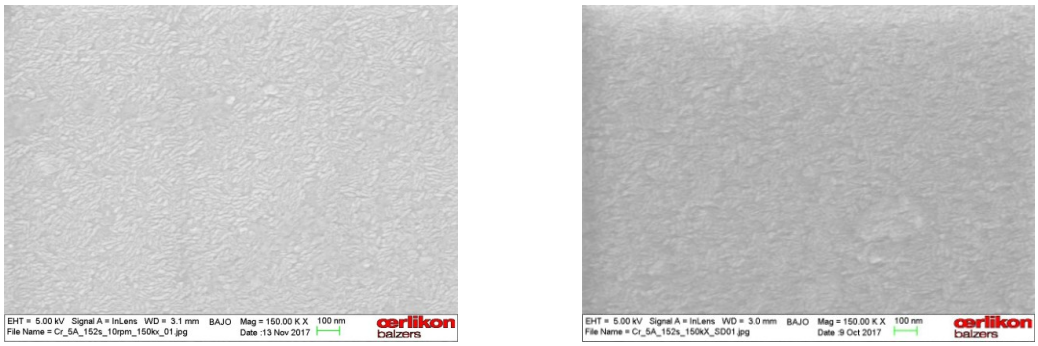

Figure 50. *Evolution of the surface morphology of Cr film with the substrate rotation from 10 rpm (left) to 30 rpm sccm (right)*

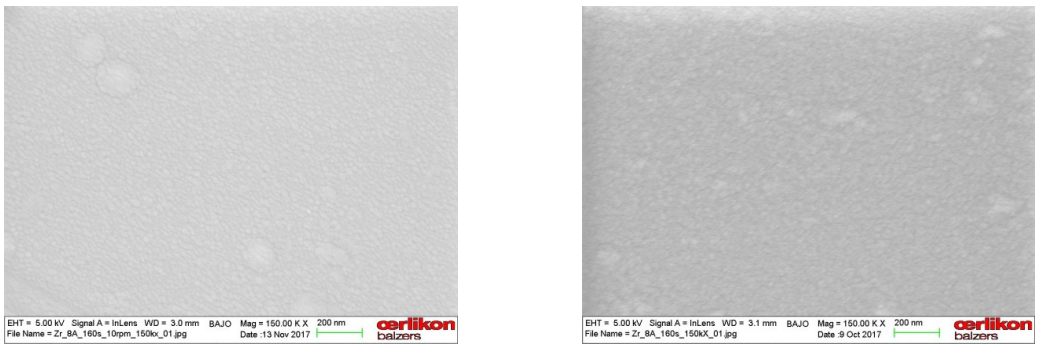

Figure 51. *Evolution of the surface morphology of Zr film with the substrate rotation from 10 rpm (left) to 30 rpm sccm (right)*

4.5 XRD phase and texture analysis

For all film thicknesses, chromium shows a very sharp (110) texture in the cubic phase (PDF-85-1336 [82]) with no other peaks present in any of the XRD patterns. The (110) peak increases with the sputtering time and therefore respectively with the film thickness as can be observed in Figure 52. For the thinnest chromium film, deposited at 76 s, no peak is visible at the T2T measuring setup (see appendix).

In Figure 53 XRD pole figures for chromium films of 72 nm (left) and 580 nm (right) thicknesses are shown. Both films exhibit a preferential (110) orientation perpendicular to the surface. Whereas the 72 nm film nearly shows a rotational symmetry with a texture value of 55, the texture of the thicker film resembles more of a „single crystal" type texture with a texture value of 314. Those numbers are a measure for the magnitude of texture. The higher, the more textured is the material.

For zirconium, no distinguishable peak is visible for the thin film deposited at 80 s and 160 s. For the thicker films, only one broad peak at around 35° becomes visible. However it is not clear if the cubic(PDF [83]) or hexagonal phase (PDF [86]) fits better.

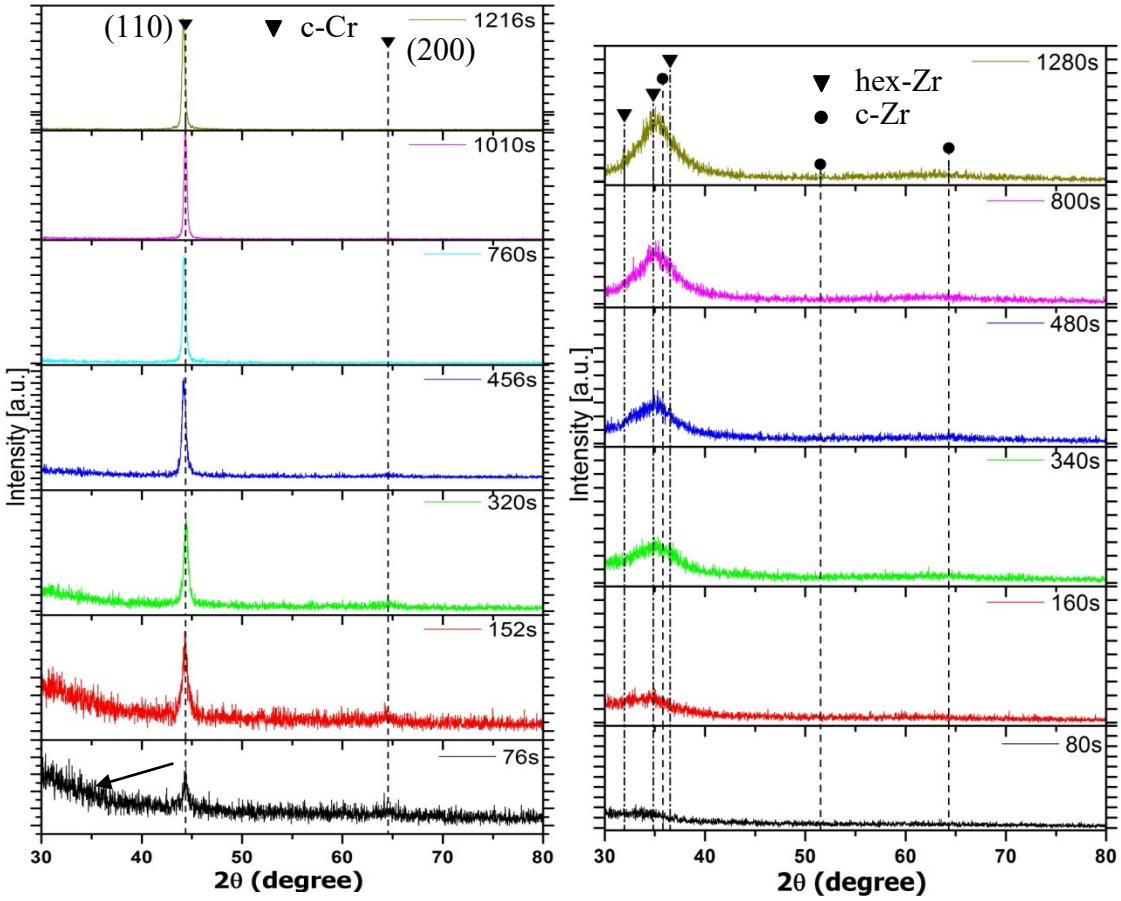

Figure 52. *GI 2°XRD patterns of Cr (left) and Zr (right) for different deposition times. Cr shows a 110 texture for all thicknesses. For Zr a change from an amorphous hump for the thin films to crystalline structure with the thickness is observable.*

Neither target current, rotation speed nor interrupted deposition results in visible changes in phase or texture for the Cr and Zr films. Also depositing the zirconium on Cr or basecoat does not change its phase or texture (see appendix). Changing the argon flow however results in a small peak on top of the hump for Zr. The peak emerges at 140 sccm and becomes more distinguishable for 200 sccm. Chromium, on the other hand, is not influenced by a change in the argon flow.

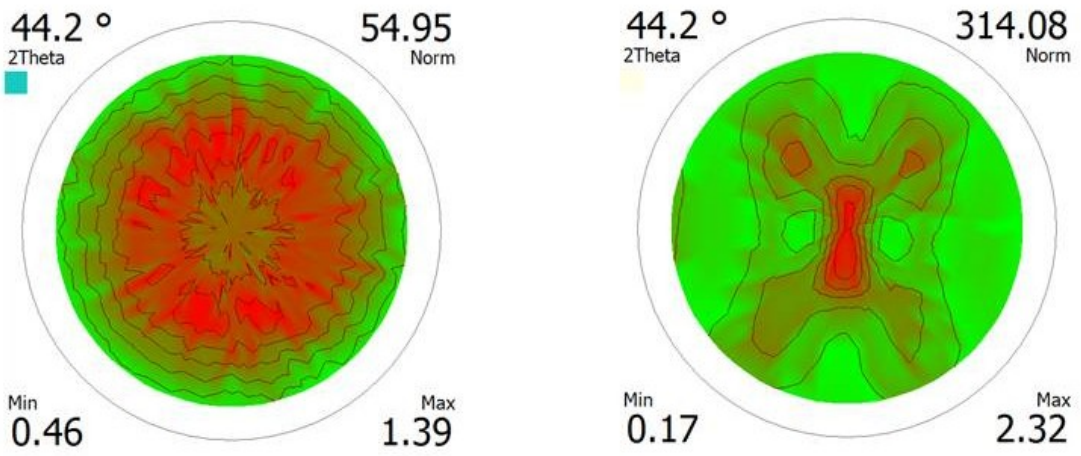

Figure 53. *XRD 110 Pol-figure for Cr deposited in 152 s (left) and at 1216 s (right). The red marks areas of high intensity. The thin films shows a rotationally random oriented 110 fiber texture whereas the thicker film shows a single crystal like texture.*

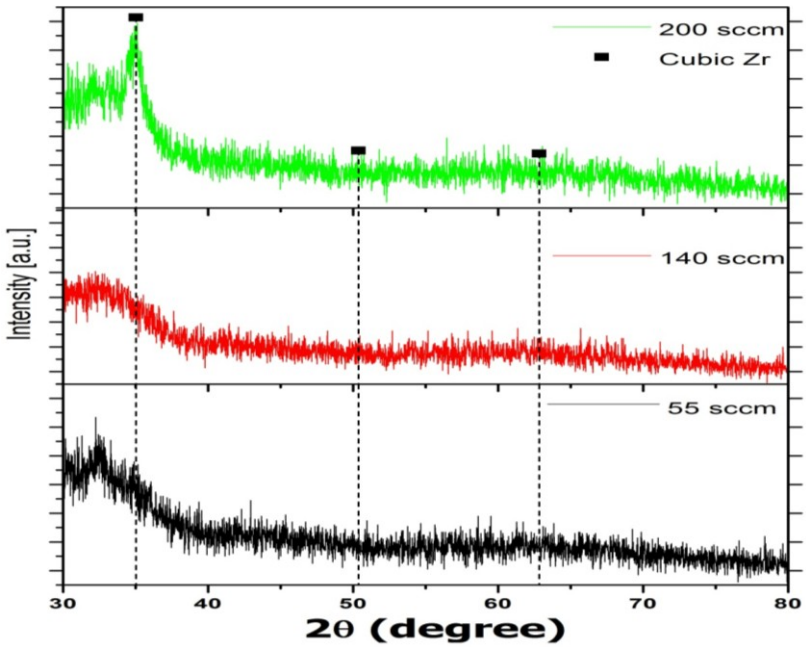

Figure 54. *XRD pattern in the 2θ setup of Zr sputtered at different argon flows. For 200 sccm a peak which indicates the presence of crystalline cubic Zr phase can be seen.*

4.6 XRD crystalline size measurement

The crystalline size measurement for the chromium shows a drop in size after around 300 s sputtering time. After this, a slow increase of the size with the times is observed. The overall change however is not that substantial. By contrast, an increase in the target current leads to a significant decrease in the crystalline size from 37 nm down to 20 nm.

For the rotation speed, a small dip in the size is to observe for 20 rpm, whereas for the change in argon flow an initial plateau of around 22 nm is present for 55 and 140 sccm after which the size drops to 14 nm for an argon flow of 200 sccm

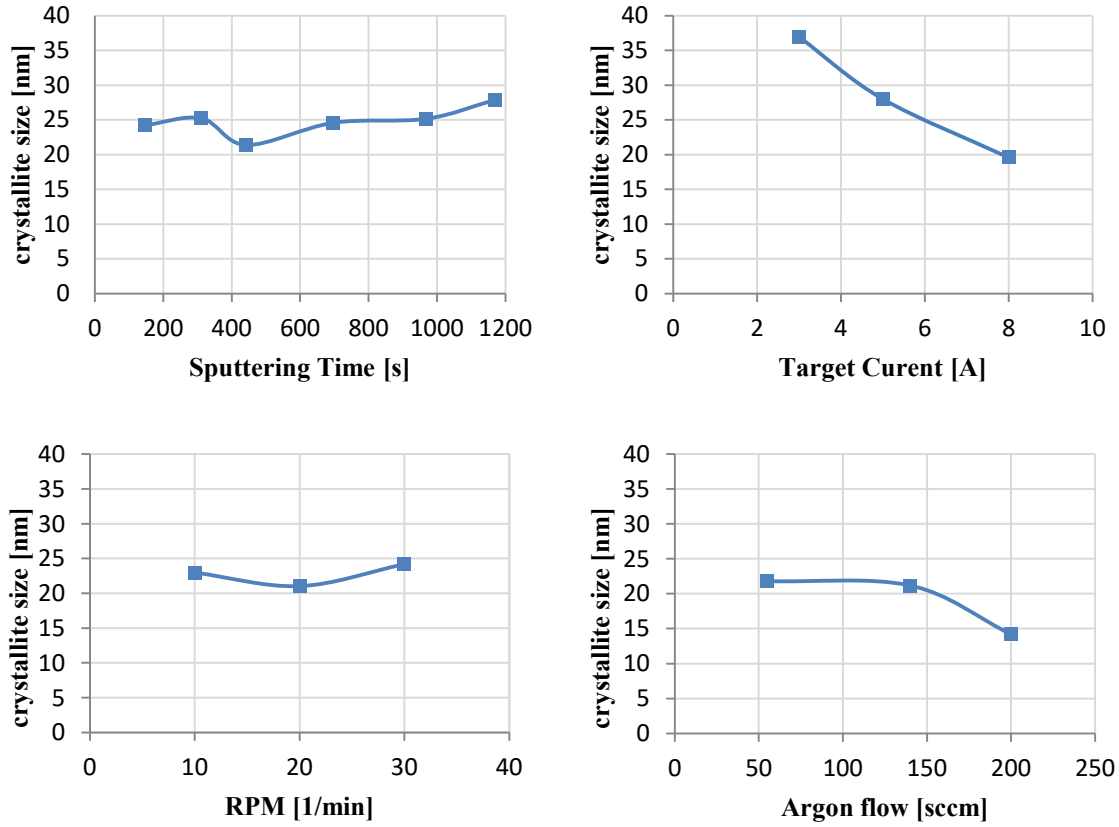

Figure 55. *Influence of the Process Parameters on the crystallite size measured by the XRD. For sputteringtime, RPM and Argon flow no significant change in the crystalline size can be observed. For an increase in the target current however a drop in the crystalline size can be seen.*

4.7 XRD stress measurement

Since the zirconium film does not show any sharp peak, no XRD stress measurement was conducted for the zirconium films. It is important to note the indicated error bars in the plots is a reflection of the estimated statistical errors in (or goodness of fit of the peak) the sin2 ψ and cos2α-sin2ψ plot.

Considering Figure 56 the chromium film deposited in 152 s shows a linear plot with a positive slope, which indicates tensile stress, for sin2psi as well as for cos2a-sin2psi. For the thinner film deposited at 76 s, it was only possible to detect a signal from the film in the glancing incidence setup.

For the film deposited at 456 s, the sin2ψ and cos2α-sin2ψ behaviour change to a more oscillating plot for the sin2psi and to a V-shaped-like plot for cos2a-sin2psi. This trend in behaviour for the plots continues for the coating deposited at 760 s, 1010 s and 1216 s. A table with the comparison of the plots is presented in the appendix.

Measuring the stress of the thicker films (see Figure 57) along the transversal axis results in an oscillating behaviour with a lower range. For the thin films (see Figure 56), no changes in either the sin2ψ or cos2α-sin2ψ plots are observed.

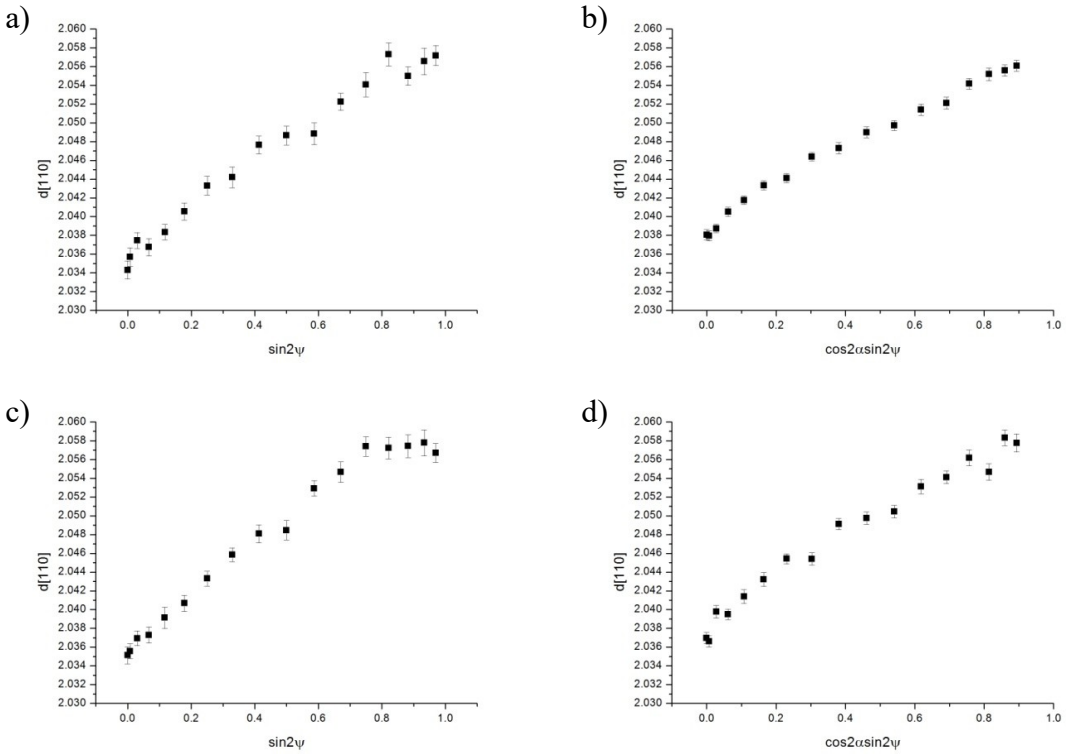

Figure 56. *Plots for stress measurement for Cr deposited at 5A, 152s. Top row: longitudinal a) T2T b) GI2°. Bottom row: transversal c) T2T d) GI2° All plots show a linear dependency with a positive slope, which allows to determine the stress.*

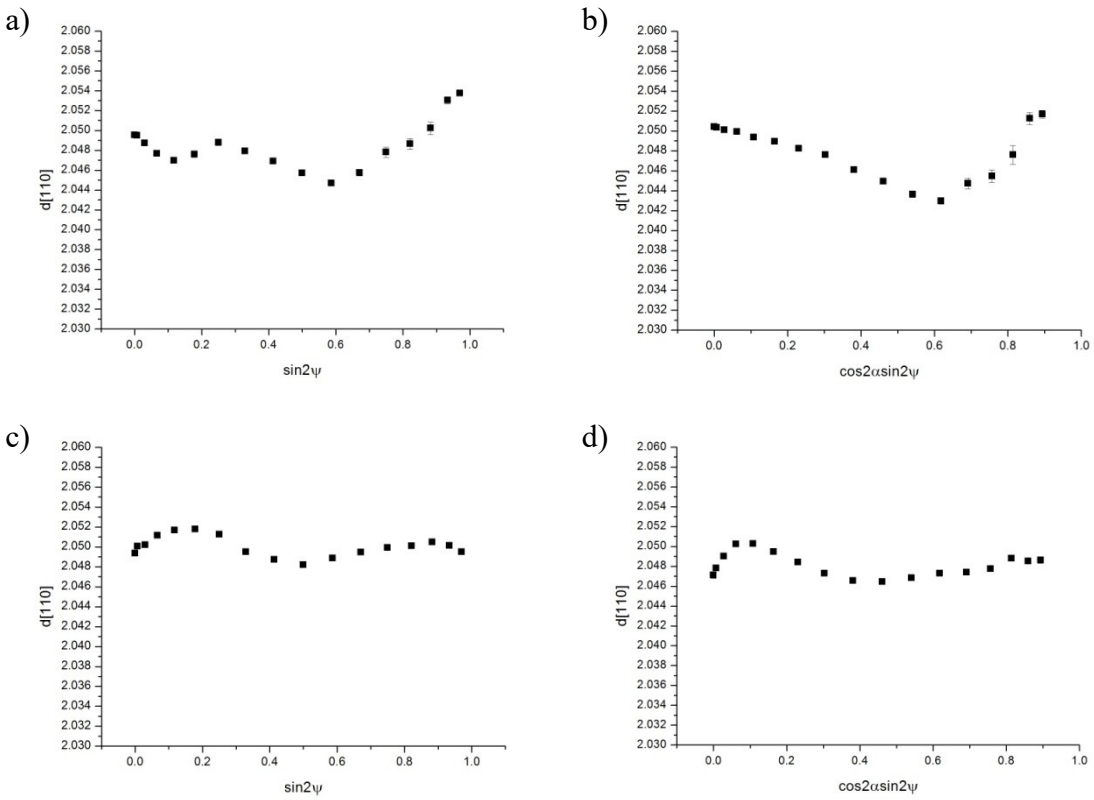

Figure 57. *Plots for Stress measurement for Cr deposited at 5A, 1216. Top row: longitudinal a) T2T b) GI2°. Bottom row: transversal c) T2T d) GI2°. Contrary to the thinner films in Figure 56, the plots do not show a linear dependency. Furthermore different behaviour of the plots along the longitudinal and transversal direction can be observed.*

The chromium film deposited with a low target current of 3 A shows a scattered sin2ψ and cos2α-sin2ψ plot. With the increase of the target current, both plots become more linear. All plots clearly indicate tensile residual stress.

The sin2ψ and cos2α-sin2ψ for the change in argon flow plot show one can a slight increase in scattering of the data point with increasing argon flow. This trend is more obvious for the sin2ψ plot. Changing the rotation speed did not cause any change in the sin2ψ and cos2α-sin2ψ plots.

Calculating the XRD Stress

For the stress calculation, only the slopes of the sin2psi and cos2a-sin2psi plots with a linear slope were used.

Calculation of the stress was carried out as described in the theory section with the use of the XEC from Table 6 in section 3.3.5. A comparison of the obtained residual stress using the different XECs values for the Cr film deposited for 152s can be seen in Table 8.

Table 8. *Influence of XEC on the residual stress result using XRD*

XEC	XEC_{110} 1	XEC_{110} 2	XEC_{macro} 3
Stress [MPa]	2529 ± 98	2754 ± 107	1128 ± 44

The XEC 3 from the nanoindentation is used hereafter to calculate the stress for the different parameters. For the raise in target current a simultaneous increase in the stress is observed. Whereas for increasing the substrate rotation speeds a decline in stress is observed. For both parameters the sin2ψ and cos2α-sin2ψ showed the same relationship. Regarding the argon flow, only a minor change was observed from 140 sccm. This was evident either as a drop in stress for the cos2α-sin2ψ or a peak in stress for the sin2ψ method.

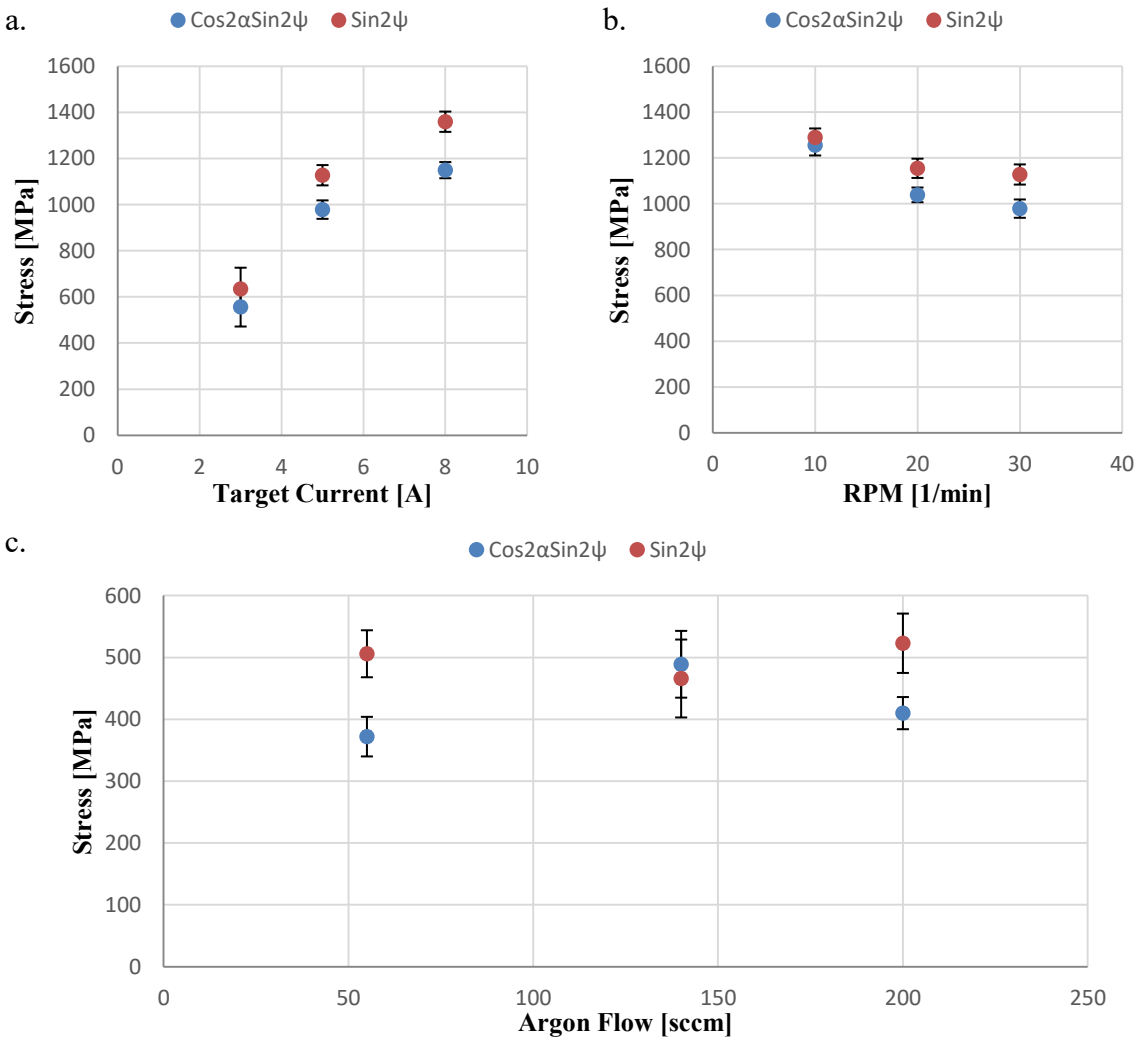

Figure 58. *XRD stress results in the Sin2ψ and Cos2α-Sin2ψ setup for a.) Target current, b.) Rotation speed and c.) argon flow. Both methods deliver similar results. With an increase target current and increase and with an increase of rotation speed a decrease in tensile stress can be seen. The argon flow does not seem to affect the stress.*

4.8 Surface investigation by Light Optical Microscopy

None of the chromium films shows cracks on the SMS. Contrary to this, only the thin chromium films, including the film deposited at 456 s show no cracks on the microscope slide. The thicker films, namely the ones deposited at 760 s, 1010 s and 1216 s, show cracks and flaking in some areas over the MS surface.

The zirconium films show no cracks on either of the two substrates.

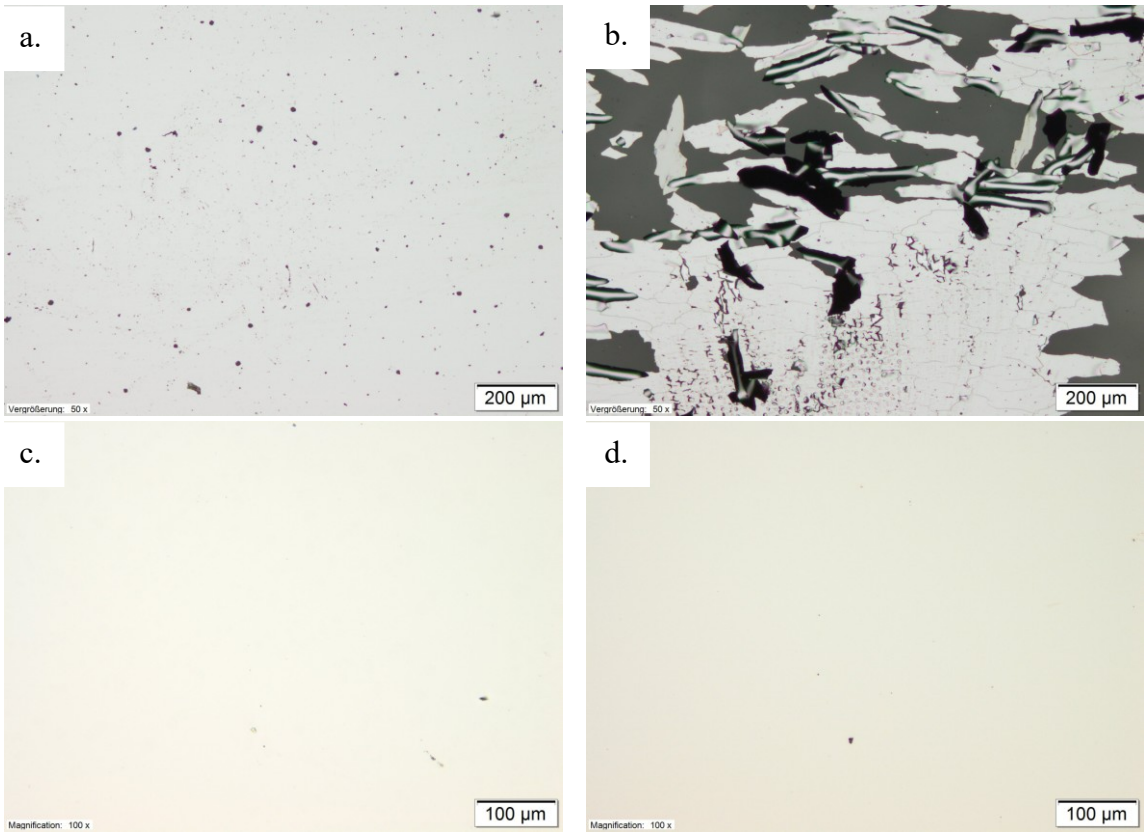

Figure 59. *The difference in cracking and loss of adhesion for a thin and thick Cr film in dependency of the elasticity of the substrate. Cr layer deposited at 5A for152 s on the microscope slide (a) Cr layer deposited at 5A for760 s on the microscope slide (b)) Cr layer deposited at 5A for152 s on SMS (c) Cr layer deposited at 5A for760 s on SMS (d)*

4.9 Deposition of force balanced PVD layers

Based on the obtained results, attempts were made to produce a stress-free layer stack consisting of Cr-Zr-Cr. The monolayers presented in the table below were used to produce this layer stack with the idea to tailor the stress to a specific value.

Using a chromium layer deposited at 5A for 76 s as an adhesion layer and the same layer on the top, results in a calculated total of 90.6 N/m which needs to be balanced (see Table 9).The single force per unit width which is exerted by a zirconium layer deposited at 8A for 160 seconds equals to -14 N/m. Dividing the 90.6 N/m/ from Cr by 14 N/m from the Zr layer equals to 6.5 layers which need to be deposited to balance out the stress. This would be equal to a total zirconium thickness of 840 nm and a total deposition time of 1040 seconds.

The problem for both trails was that the zirconium target did not run constantly during the whole deposition process. Sometimes the target did not ignite after the short break or the current broke down during the deposition. This is evident when looking at the resulting Ampere-second [As] displayed in Table 10. It was therefore not possible to deposit the intentioned film thickness.

Table 9. *DOE planned for obtaining stress designed layer stack. For explanation see section 2.4.4*

	Measured on single layer			Calculation of layer stack		
Monolayer	**Cr**	**Zr**	**Cr**	**2 x Cr**	**6,5 x Zr**	**∑ Layer Stack**
t [nm]	50	129	50	100	840	940
Stress σ [MPa]	907	-107	907	907	-107	0.87*
Force F [N/m]	45,3	-13,9	45,3	**90,6**	**-90,35**	**0.25**
Δh [µm]	27,3	-8,3	27,3	**54,6**	**-53,95**	**0.7**
As	380	1280	380	**760**	**8320**	**9080**

Table 10. *Results of the stress designed layer deposition. The stress and force could be reduced by depositing the Zr layers. *For explanation see section 2.4.4.*

Layer Stack	t [nm]	σ [MPa]	F [N/m]	Δh [µm]	As_{Cr}	As_{Zr}
Calculated	**940**	**0.87 ***	**0.25**	**0.7**	**760**	**8320**
Measured **# 1 Cr / 6,5xZr / Cr**	343	152	52.1	31.4	711	3860
#2 Cr / 6,5xZr / Cr	434	111	48.4	29.1	723	5446

5. DISCUSSION

Before proceeding into the discussion of the results, it should be noted that the physical underlying mechanisms for the development of stress in the thin film are under continuous debate and have been over the past decades [30],[37]. The reader is urged to keep in mind that the results, obtained with the equipment at hand, are sometimes discussed and correlated with the results obtained with more sensitive and methods with a higher resolution (In-situ stress measurement, TEM, AFM). Nevertheless, comparable results seem to be obtained. As it was mentioned in section 2.4, the residual stress consists of an intrinsic and a thermal stress component. Since the coatings were deposited at around 60°C on glass, which shows a comparable CTE to the ones of Zr and Cr, the calculated thermal stress results in -26 MPa for Cr and -16 MPa for Zr. This effect is therefore neglected in the following discussion. The calculation of the thermal stress was conducted according to formula 2.

5.1 Influence of the film thickness on the coating properties

Chromium

The investigated chromium films show a columnar-like structure, which is typical for sputtered chromium films [13]. Such a growth can be ascribed to the low mobility character (also named “Type 1” material) of the chromium deposition process (T_{dep}/T_{melt} = 0.153). Those conditions do not allow diffusion and grain growth, which leads to columnar grains, by the low-mobility Volmer-Weber growth mode [30][87]. This behaviour therefore matches with the zone 1 character in the Thornton SZD [19] as point out in the theory section.

The observed needle/ triangle-like surface appearance for the thicker chromium films ($t_f \geq 200$ nm>) (see Figure 44) was observed in papers published by Janssen [13][88]. He described the morphology as an anisotropic structure, which is a product of the highly anisotropic deposition system due to the elongated rectangular target geometry. Additionally shadowing caused by substrate rotation was mentioned as an influencing factor [88].

For the thinner films (tf<200 nm) the morphology does not show a well-distinguished shape or pattern. One could argue, since the stress vs. thickness curve correlates with the film formation stages, as will be described next, the film is not completed dense/continuous at this stage. Therefore one could assume that the samples Cr-5A-76s

shows the island growth stage and the sample Cr-5A-152s the coalescence stage, where the first needle likes grains appear [16][30][87]. This is further confirmed with the observed stress in relation to the thickness, which will be addressed next. In terms of the thickness scale this makes sense since, as it was pointed out by Ohring [16], those processes take place in the first few 100 Å.

The island growth stage of the film formation is initiated when small stable clusters start to nucleate on the substrate. Such clusters grow in three dimensions, while the island density starts to saturate fast. During the following coalesces stage, the crystallographic facets of the initial islands are often preserved. As the coalescence continues, the emergence of a partly connected continuous film in form of a network with unfilled channels in between can be observed [16]. Those stages can be present over a wide range of film thicknesses for low mobility materials, depending on the process parameters[16][43].

Taking a look at Figure 27, one can observe a rapid initial increase in tensile stress with the film thickness. This section, of increasing tensile stress with the thickness, corresponds well to the nucleation, island formation and percolation stage of the film growth, leading to a continuous film [30][87]. Studies, which focused on this initial growth stage of low mobility metal films, contribute this observed increase in stress and the ongoing microstructural evolution, to the formation of new grain boundaries [30]. This formation process is explained with the attempt of neighbouring islands to reduce their interfacial energy by forming new grain boundaries [30].

After the initial increase in stress, the tensile stress starts to decline after it peaked. Hong [33] found a similar behavior for his investigated samples. He used the term "critical thickness" t_c for the thickness beneath ($t_f<t_c$) which the stress rises and at which ($t_f=t_c$) the maximum stress value is measured. For thicker films ($t_f>t_c$) he observed a gradual decrease in tensile stress with the thickness. This corresponds well to findings in this work (see Figure 27). Hong [33] defined the threshold for t_c by a qualitatively relation of the radius R and the film thickness t_f within the Stoney equation and pointed out, that above t_c only minor changes in the radius R can be observed. For further Information please see appendix.

Also Janssen and his colleague Kamminga [89] published results which showed similar behaviour for chromium films [89]. They found an increase in column width at the top of the chromium film with an increase film thickness and translated this to a decrease in grain boundaries density with an increase film thickness. Based on the fact that the stress is supposed to be generated at the grain boundaries, and a similar coating structure is observed in the present work (see Figure 41), their observation is supporting the observed decreased in tensile stress with the film thickness.[13][31][89]

Furthermore, Hong [33] found that the interfacial stress force (N/m) between substrate and film mainly increases in the region $t_f<t_c$. In the following region ($t_f>t_c$) the contribu-

tion of each additional atom layer shows a lower influence on N/m in comparison to the previous region. Those two regions are visualized with the lines in Figure 60.

Such a change in the behavior of N/m vs. thickness was also reported by Hoffmann and Thornton [50]. They, as well and Hong [33] assumed that this might signals a loss in adhesion or another relaxation mechanism inside the film, which causes a decrease in the slope of the force per unit width. Long and her colleagues [75] verified those assumptions in their work and furthermore introduce the term "critical interfacial force"(N/m), above which they were able to observe cracking. They concluded that for a fixed critical interfacial force, decreasing the substrate thickness allows increasing the film thickness. This can be understood by, that a thinner substrate or a substrate with a lower Young's modulus can comply easier than a stiff and thick one. Because of this, the force of the film, which causes bending of a complaint substrate, can cause cracks on a stiff and thick one.[33][75]

This hypothesis describes what can be observed in Figure 59. The thin chromium film shows no cracks and good adhesion on the MS and on the SMS. The thick film ($t_f > t_c$) shows cracks and delamination on the MS. Since the SMS however can dissipate the force induced by the thick film, no cracks emerge here. By merely looking at the residual stress vs. thickness curve one probably would not come to such a conclusion since the stress values drops after the critical thickness t_c. It is therefore argued that the force per unit width can be considered a more valuable predictor for the film stability and adhesion.

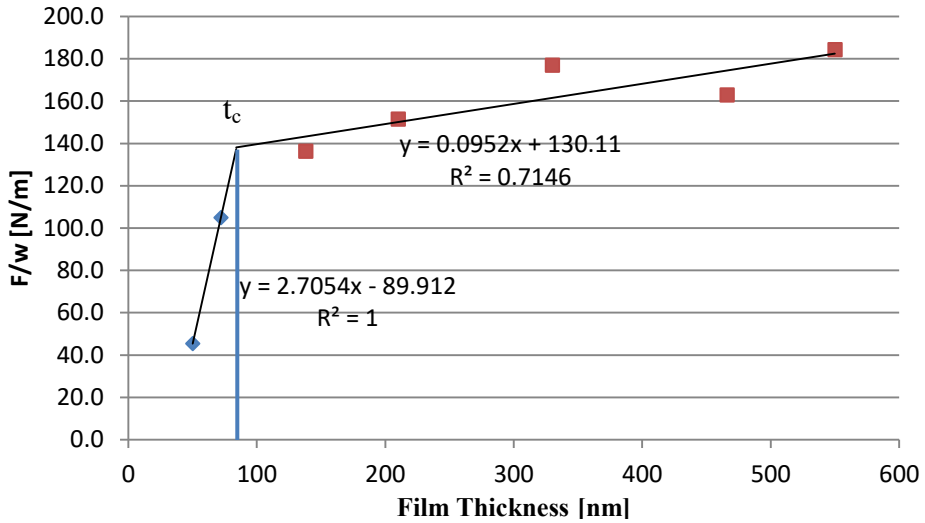

Figure 60. *Influence of coating thickness on N/m of Cr deposited with 5A at 1.0 x10^{-3} mbar. The two parts of the curve are fitted individually by linear functions and show the change in F/w which can be related to a change in the growth morphology.*

Before discussing the XRD results it is important to note that the slight hump, which is observable in the XRD pattern in between 30-40°(See Figure 52), as indicated by the arrow) stems from the used glass substrate and not from the coating.

The observed peak in the XRD pattern in Figure 52 corresponds well to the (110) peak of the bcc chromium (PDF 85-1336[82]). Such a strong (110)-texture is often present in sputtered chromium, as it has been reported by Moore et al. [46] and in other publications [50][88]. Comparing the pole figures (see Figure 53) of the film deposit in 152 s and the one deposited in 1216 s, one finds a preferred growth orientation in the [110] direction for both. However, the 152 s film shows a random fiber like texture, whereas the 1216 s film shows a "single crystal-like" texture. Similar results were published by Janssen et al. [88]. They argued that nuclei with a {110} plane parallel to the substrate surface are energetically favoured over others. This either indicates the total absence of nuclei with a {111} orientation or that the growth mechanism favours the [110] direction over the [111]. This goes in hand with result by Feng, et al [90] who found that after 20 nm an (110) texture exists since it overgrows grains with other orientations

It was further hypothesized by the same Janssen [88] that the development of the "single crystal like" texture is a result of shadowing. In a one-fold rotation, chromium atoms arrive at the substrate under a glancing angle every time when the surface normal is not parallel to the target normal and when it points away from the target. The latter is the point of maximum shadowing. Also the elongated target shape was pointed out as a factor for shadowing.[88] Similar results were found by Karpenko et a. for Mo [91] who gave a similar explanation for the emergence of this structure.

One possible explanation for the transition from a random columnar structure to a more "single crystal like" is might given by a mechanism presented by Hong [33] which he used to explain a change in film structure. For a given deposition pressure, the shadowing mechanisms causes the atoms to reach the substrate at oblique angles, which results in a variety of void spacing and randomly oriented, tilted columns. When a specific film thickness is reached, which is mainly depended on the sputtering pressure, the voids exhibit certain spacing, allowing the existing film to act as a growth-template to facilitate a normal columnar growth. [33]. In his work Hong [33] however correlated this growth behaviour only with the observed stress, which showed a maximum at the point of transition from tilted oriented columns to normal oriented fiber growth. It is nevertheless argued that this mechanism also could facilitate growth in a single crystal like fashion. This hypothesis needs however further investigation to find out how the stress and the development of the film structure are correlated.

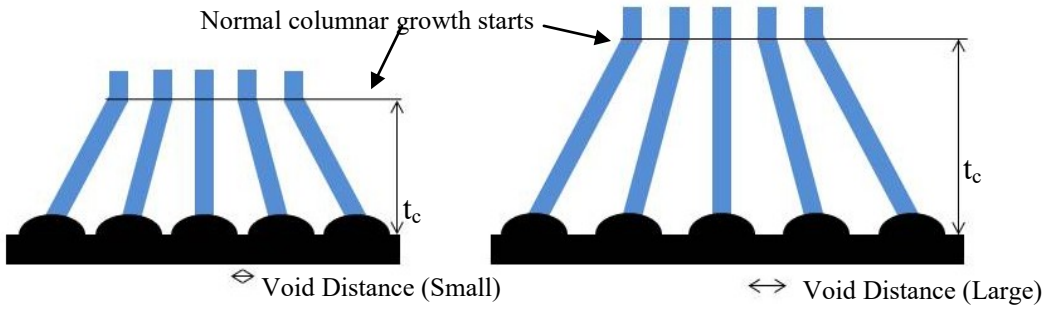

Figure 61. *The effect of pressure on critical thickness of film growth. Low pressure and therefore small shadowing effect (left). High Pressure and large shadowing effect (right)*

The previously discussed (110) texture helps to explain the observed oscillating behaviours of the sin2ψ and cos2α sin2ψ for the thick chromium film. As it is mentioned in the literature, a deviation from the linear behaviour can have its root in texture and/or anisotropy of a thin film [28][62]. When recording sin2ψ and cos2αsin2ψ for the thin films a linear behaviour can be observed in both sample directions. The thicker films however show a different oscillation when measuring along longitudinal and orthogonal sample axis (see Figure 56 and Figure 57 respectively). It can therefore be assumed that non-linearity of the sin2ψ is a direct result of the highly textured film.

Despite the fact that literature suggests using XECs from single crystal data sets, if available [66], the Young's modulus derived from the hardness measurement was used to calculate a macroscopic XEC.

The first reason for this is that using the Young's modulus from the hardness measurement yields stress values of 1128 MPa which closer to 1103 MPa, obtained by the curvature method. This becomes evident when comparing the XRD stress result in Figure 58a, with result from the curvature method in Figure 31. Additionally, the stress values obtained by the single crystal data are around double the one obtained from the macroscopic Young's modulus (see Table 8). This probably has its roots in the single crystal data itself, since the calculated Young's modulus from the single crystal data sets show values which are up to two times higher than the one measured by the hardness measurement (see Table 6). However, since the measured value for the Young's modulus of 126.5 GPa as well as hardness with 8.5 GPa are actually close to reported values for porous sputtered chromium films with 140 GPa [92] and 7.5 GPa [93] respectively, using the macroscopic XEC is considered a reasonable decision. The fact that the Young's modulus of the porous sputtered Cr is lower compared to bulk chromium or chromium which was sputtered with a bias, can be explained by the rule of mixture [93].

Zirconium

As will be discussed later on, the structure of the Zr films is considered amorphous in the first few hundred nanometers. However, the mechanisms discussed hereafter are

obtained on crystalline films, which should be taken into account when considering the full validity and transferability of the proposed mechanism. Mayr and his colleague [94] proposed a mechanism which combines the models present for crystalline material and used it to explain the stress development in amorphous films. It is therefore assumed that the underlying mechanism of reducing the overall energy in the system, as the base of those mechanisms, is also applicable for the present case.

The investigated zirconium coatings always exhibit compressive stress, as it was observed by other authors [42][43]. Drese and his colleague [42] reported that the stress state of sputtered metallic zirconium however strongly depends on the used deposition pressure [42]. Despite the fact that the reported transition pressure values for a compressive-to- tensile transition differ between 8.0 E-3 to 3.5E-2 mbar [35][42] both values are above the pressures measured during the experiments, which supports the presence of compressive stress.

Considering the stress development with the thickness, Chakraborty et al.[43] observed a similar behaviour for crystalline zirconium films. They attributed the stress development in the first stage (region I, Figure 62) mainly to the formation and growth of nuclei which transitions into island growth and the formation of atomic clusters. The actual mechanism responsible for the compressive stress is due to the so-called surface stress which exists between the amorphous substrate and the atomic clusters.[43][95]. It was also pointed out that such a stress can, in theory, be calculated with existing models but caution regarding results for the Zr/glass interface were raised [43][96]. Mayr and his colleague [94] used the argument of energy reduction in the system, which lead to increase in tensile stress in this region. They also observed a cusp-like film morphology and connected the growth of those cusps along with the film thickness, to the simultaneous tensile stress generation, based on a local energy minimization [94]

In the model of Chakraborty et al[43], the section, which corresponds to the range between 110 nm and 500 nm in the present work (region II), is characterized by the formation and growth continuation of the isolated islands, which eventually leads to the formation of a stable and connected film. The coalescence of the isolated islands causes shrinkage in the in-plane direction of the film, generating tensile stress. Additionally, the authors [43] argued that, the longer deposition time increases the substrate temperatures, causing formation and growth of grains by atomic self-diffusion. The generated compressive surface stress [43] and the tensile stress generating mechanism are of opposing nature, which lowers the overall stress in the film in this region.

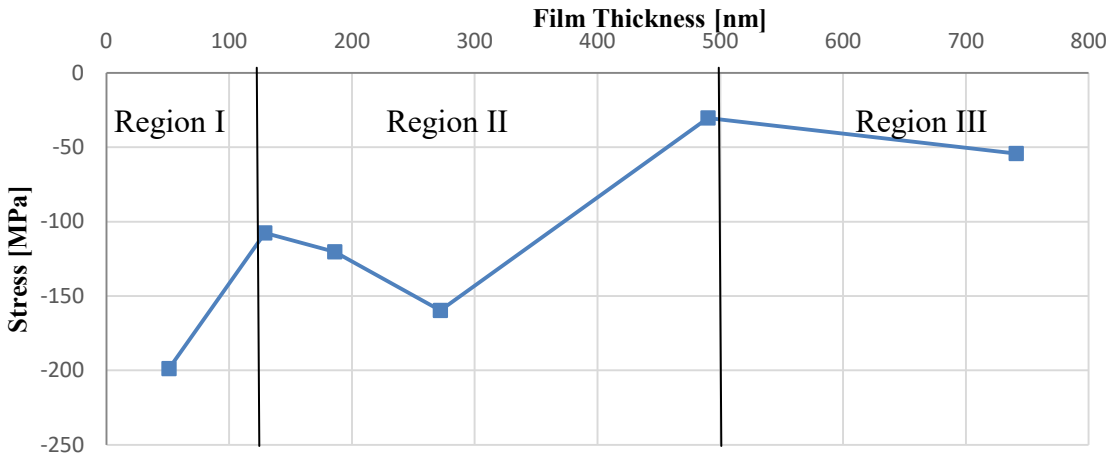

Figure 62. *Influence of coating thickness on residual stress of Zr deposited with 8A at 1E-3 mbar and the separation in different film evolution sections I, II and III.*

In the film with a thickness above 500 nm (region III) the authors [43] assumed that the working mechanisms are grain growth driven by vacancy annihilation and continuation of tensile stress development due to a net shrinking of the film. The latter process is terminated at a certain film thickness, since the energy, comprising of the sum of strain and grain boundaries energy, of the system approaches a minimum. This results in an overall lower steady compressive stress state for thicker films, which coincides with present findings for the zirconium films [43]. It is however stated by the authors that this mechanism needs further investigation [43]. Since the structure resembles an amorphous like structure only in the first few hundred nanometers and becomes crystalline as evident by the XRD and SEM fracture this relaxation mechanism could be a valid assumption for the thicker films.

The change of growth mode in between the different thickness regimes pointed out above is also evident when considering the difference in stress for the films which were deposited by four intervals with a five second break in between. For the thin Zr films (≈ 100 nm, region I) no difference in stress development in between the continuous and the interrupted deposition is observed as can be seen in Figure 37. Contrary to this stands the thick Zr film (≈400 nm, region II) where the film deposited in a continues process shows a lower stress compared to the film with the same thickness deposited in 4 single steps. This observation needs further investigation since a growth interrupt for low mobility material films is known to not affect the continuation of stress development[30]. This is in general explained with the low mobility character of Zr, which prevents grain growth, resulting in a matching microstructure of the new layer with the layer beneath[30].Those results hence support the observed change in growth mode when deposited in a continues manner.

Results published by Dixit et al.[40] show a similar development of the Zr film structure with the film thickness. As an explanation, they proposed that the large mismatch be-

tween the lattice/structure of the glass substrate and the zirconium leads to the development of a highly disordered phase for a film thickness t_f <200 nm. Indeed, taking a closer look at Figure 42, one could think that at around 150 nm there is an interface visible after which the structure appears to be more crystalline/grain-like in nature. The authors [40] suggested that such an initial layer later on acts as a buffer layer for the following Zr films, which allows continuation of the growth with an increasing crystallinity and a decreased defect density. The authors [40] also reported an initial amorphous structure in the XRD for thin Zr films which changed to a highly crystalline structure for thicker films. In this work the crystallinity also did develop from an amorphous-like to a more crystalline structure with the thicknesses as can be seen in the XRD pattern in Figure 52 and cross-section Figure 42. The observed crystallinity however was not as well-distinguished in comparison to the results published by Dixit et al.[40].

Development of the Zirconium Phase

As previously mentioned, an amorphous Zr film was found in the present work, with a slight increase in crystallinity as a function of the film thickness. Contrary to this stand results from previous trails at *Oerlikon Balzers* were Zr was deposited on an in-line coating machine on a lacquer coated substrate, where a mix of probably hexagonal and cubic phase was found as a result (see appendix). An influence of the lacquer and a Cr adhesion layer could be excluded as an influencing factor on the Zr structure (see appendix). This begs the question what other factors influence the formation of a crystalline or amorphous film.

The two biggest differences which stand out for those results are that the two machines (batch and in-line) have a difference in power density and that the targets in the in-line coater are under constant vacuum. Therefore, an influence of either the target power or of an oxidized target on the film structure could be assumed to cause a phase change in Zr and need further investigation.

It is known that amorphous films grow preferably at low substrate temperatures (T_{dep}/T_{melt} <0,3) and at high deposition rates. The low deposition temperatures hinder the diffusion of atoms to find equilibrium lattice sites, which is fulfilled in both investigated cases. The high deposition rate hinders the atoms to move to such energetically favourable places before other ad atoms arrive at the surface. The result of this is that such atoms are trapped and overgrown by the further growing film[97]. Comparing the depositions rates of the initial trail (≈0.97 nm/s) with the one in the trails of this work (≈0.39-0.92 nm/s) it is however assumed that this is not a determining factor.

Based on this it could be hypothesized that zirconium develops a crystalline structure at low flux energies and an amorphous structure, with a high amount of defects, at high flux energy. This is mainly influenced by the power density of the target. Furthermore,

with an increasing argon flow, which means a lower energy of the incoming particles, also crystalline phase emerges as can be seen in Figure 54. As pointed out by Girardeau and his colleagues [41] Zirconium can exhibit a wide range of phases and phase mixes, including an amorphous structure.

An argument for the oxidized target caused by the presence of residual oxygen is made by Drese et al. [42]. They stated that even small amounts of present oxygen change the phase from a purely crystalline Zr to a nanocrystaline ZrO phase. The problem is that, metallic Zr and ZrO have overlapping peaks, which makes it difficult to distinguish the two in the XRD pattern. His results could support the hypothesis that, since the targets in the In-line machine is under constant vacuum, a pure metallic zirconium crystalline phase forms. Contrary to this stands the batch machine, where the target gets contaminated by oxygen every single time the machine loaded. However, results published by Dixit et al. [40] also show the presence of amorphous zirconium, even with an initial pre-sputtering of the oxygen contaminated target.

As one can see, no clear conclusion about the development of the observed zirconium phase can be drawn for now. Therefore a more in-depth investigation about the causes for the formation of the zirconium phase is needed.

5.2 Influence of the target current on the coating properties

As pointed out by Thornton [87] a deposition process is carried out under high supersaturation, resulting in small critical nuclei, which leads to a high nucleation rate and small grains. It is argued that an increased target current results in a higher supersaturation of the atomic flux at the growth front, which increases the nucleation rate and with it, decreases the grain size of the chromium film. Since the average crystalline size decreases with the target current (see Figure 55) the grain boundary density is increased simultaneously. Several authors referred to work done by Doljack and Hoffman [16] [19][88] which states that the tensile stresses are generated at the grain boundaries due to the reduction of the distance between neighbouring grains, caused by the interatomic forces between those. Due to this, the observed increase in tensile stress with the target current (Figure 31) corresponds well to the simultaneously observed decrease in grain size in the XRD as can be seen in Figure 55.

Calculating the unstrained lattice constant with equation (8) [13][62] for the different target currents results in a decreasing lattice constant with an increasing current, towards the reported unstrained bulk lattice. Janssen [13] observed a similar trend and explained that the stress generated at the grain boundaries stretches the film in the in-plane direction while simultaneously is contracted it along the normal axis.[13] He therefore assumed that a film with more tensile stress should exhibit a smaller lattice constant with respect to the film with less tensile stress. Also Vergason [1] found that the cracks, which usually occur in the presence of tensile stress [15] can be reduced by lowering the sputtering power (hence the target current). In his work, the stress state of the film is however not stated [1] and it can therefore only be speculated that the tensile stress decreased as well.

Several authors [30][31] mentioned that the development of compressive stress is still a part of an ongoing debate. A possible explanation is given by Chason and several co-authors [30][31] which shows that compressive stress has 2 main underlying processes. The first, widely accepted mechanisms, is the atomic peening process which generates point defects. The second one is a collision induced densification of the grain boundaries combined with a flow of atoms into the grain boundaries as a reason of higher surface chemical potential. It can therefore be assumed that for different materials, a competition between creation of defects and annihilation of those can create a difference in stress sensitivity for different deposition rates at a fixed pressure [98]. With this model it is possible to explain on one hand the increase in tensile stress for chromium and on the other hand the increase in compressive stress for zirconium, while raising the target current. This would mean, that for chromium the stress contribution for the higher grain boundary density cannot be counterbalanced by the compressive stress originating from atoms flowing into the additional generated grain boundaries. [32][98]

5.3 Influence of the argon flow on the coating properties

The observed decrease in tensile stress/shift towards compressive stress with the increased sputtering pressure does not fit the model of atomic peening. Such a behaviour was however shown by several authors[16][19][50]. Normally, one would predict the reverse behaviour i.e., an increase in compressive stress with lower sputtering pressure, since a lower pressure increases the energy of the impinging particles, caused by fewer collisions with the plasma. The second model, which is however often disregarded, is the incorporation of sputtering gas which leads to lattice compression in the in-plane direction. Even though no significant amount of argon was found in either of those films, it suggested by Hoffmann and Thornton [50] that it can be a nevertheless contribution factor for increasing compressive stress. Hoffmann and Thornton [50] however suggested another mechanism which is more satisfying. Since films deposited with a higher working gas pressure tend to be discontinuous in the in plane direction, lateral tensile stress cannot be supported. Therefore a decrease of the tensile stress for discontinues films, due to higher working pressure can be assumed [50]. It was however not possible to confirm such a discontinuity by either surface or fracture investigation of the films since no observable change was present.

Based on the mechanisms for compressive stress pointed out in Section 5.1 it can be argued that the emergence of tensile stress caused by coalescence of the isolated islands might be prevented due to the higher working pressure, as already described for the chromium film above. Another explanation could be the formation of a crystalline phase, which is observable for 200 sccm sample by a new peak in the XRD spectrum. Since the amount of published results on metallic zirconium is limited and the actual formation of the crystalline phase is not understood, as already discussed above, this effect needs further investigation.

5.4 Influence of substrate rotation on the coating properties

Both materials show a peak in stress at 20 rpm when considering the influence of the substrate rotation on the stress in Figure 35. Even though a change in substrate rotation speed should not influence the coating thickness, the film deposited at 20 rpm shows a much lower thickness which is almost half of the other two films. Because of this, it makes sense to consider the thickness-weighted stress (N/m) for a more neutral judgment. Herein, an only a very small peak for 20 rpm is observed for chromium. In addition to this, the same sample shows the highest (110) peak for 20 rpm. Since the radiated volume of this sample is the smallest due to the lower film thickness, this effect might be rooted in a change in growth behaviour (see appendix). Such an effect of substrate rotation on growth behaviour was pointed out by several authors [47][49] and can be explained by a change in the vapor impact angles on the substrate surface. This allows altering the growth behaviour. The obtained results also show that a rotation speed

20 rpm might result in a more crystalline coating which causes more tensile stress due to a higher grain boundary density caused by finer grains as evident from the Scherrer equation in Figure 55. Comparing both materials, a slight increase in compression force/decrease in tensile force is observed for 30 rpm in comparison to 10 and 20 rpm. It is however important to consider the scaling of the graph and it is therefore argued that the observable change for chromium and zirconium might be of no major significance. For zirconium, this is furthermore supported by no observed changes in the surface morphology, film structure or XRD pattern.

To get a better insight into the effect of substrate rotation, it is therefore suggested to deposit thicker films in order to increase the accuracy of the thickness measurement and hence the bending method.

5.5 Reliability of the results obtained by substrate curvature

Due to a limited number of SMS, no meaningful statistical results can be presented in this work. Hence, the reliability and errors induced by the measuring method are discussed to evaluate the robustness of the obtained results. Any fluctuation of the Young's modulus and Poisson's ratio of the SMS substrates is however not considered.

To validate the repeatability of the method, two SMS with different initial curvatures were coated in the same batch and measured. Those results are presented in Figure 26. The deformation and as a result of the obtained stress, show a deviation of 1.6 %, which is considered as reasonable value for this measuring method.

In the next step, the same SMS was measured 10 times by removing the SMS from the sample holder in between the consecutive measurements and realigning it again to conduct a new measurement. The resulting standard deviation of this repeatability shows with 0.9% a very low value. The method is therefore considered very reliable.

Table 11. *Results of a 10x repeated measurement. The results show a very good repeatability lof the method*

No.#	1	2	3	4	5	6	7	8	9	10	Ø	Std [%]
σ [MPa]	1140	1130	1136	1118	1129	1117	1122	1121	1140	1114	1127	0.87

Taking into account the scattering of the thickness and diameter as part of the manufacturing tolerances, provided by the manufacturer [80] of the SMS, the two scenarios for the lowest and highest measurable stress resulting from the Stoney's equation are presented.

- Minimum stress: Lowest substrate thickness, largest substrate diameter
- Maximum stress: Highest substrate thickness, small substrate diameter

Based on those assumptions, the upper limit for the obtained stress result is + 14.6% and the lower limit – 13.4% in comparison to the results determined with the used substrate properties.

A bigger actual contribution to the errors in the stress results is attributed to the values used for the film thickness. As it is obvious from the graph displayed in Figure 23 the values obtained by measuring the thickness from the fracture show a lower scattering compared to the ones obtained by the step measurement. However, those values still show a standard deviation up to 7.5 %, which is smaller than the 27.5 % for the step measurement. The calculated error for the stress values based on a maximum deviation of 7.5 % results in -6.98 % as a lower end and a + 8.11 % for the upper end of the stress spectrum.

Additionally, the following challenges were identified as limiting factors for determining the film thickness.

1. At the high magnification (up to 250.000x) used for the thickness measurement in the SEM, one pixel equals to 1.16 nm. The non conducting glass substrate can cause drifting of the electron beam during acquisition of the pictures. This will stretch or compress the picture and can cause significant errors in the thickness measurement.
2. In case the fracture surface is not parallel to the surface normal, error in the thickness measurement will arise. This is however is not considered to be big factor.
3. The exact interface and surface of the film are sometimes hard to distinguish.

Broadway and his colleagues [74] discussed in their work the measurements repeatability of in-situ stress measurement for accomplishing zero stress. For their system, they concluded that the batch-to-batch difference of a repeated process can be mostly related to in the variation of deposition temperature, argon pressure and deposition rate. For an ex-situ curvature measurement, they ascribed tracing, indexing and re-tracing of the measuring positions, before and after the deposition process, as the biggest source of error. Therefore they came to the conclusion that in-situ measurements are in favour over ex-situ measurement for achieving near-zero stress thin films.[74].

Based on those previously mentioned points it can be concluded that for a direct comparison of changes in the stress or N/m it can be advantageous to just monitor the curvature change, since both reproducibility and reparability are very reasonable as shown above. For this approach, a low bending/curvature change translates into low amounts

of stress. A more detailed discussion about this approach will be presented in the following section.

For the thicker chromium film, the rise of anisotropy needs to be kept in mind when considering the correctness of the obtained values, since the texture can cause non-uniform wrapping of the disk.[88]. It is also pointed out in literature, that the Stoney equation is only valid in case $h_f << h_s$. [73][99]. A definite number for this is published in [99] where it is stated that the ratio h_f / h_s should be lower than 0.1 for yielding a good approximation of the stress. This is always the case for the PVD films but however only for the lacquer layers thinner than 20 µm.

5.6 Predicting stress in a multilayer from its single layers

The Stoney formula shows, that if the curvature and therefore the Force per unit width of single layers are known, the sum of those single curvatures yield the curvature of all coatings when combined in a layer stack. This relationship, presented in section 2.4.4, was used by Guo and her colleagues [54] to predict the stress of multilayer structures.

An approach of directly utilizing the measured N/m vs. thickness relationship to predict N/m for a film is presented below. This is followed by the discussion of the attempt to tailor the stress in a layer stack system.

Several authors reported the influence of the stress induced by the interfaces in multilayer /layer stacks on the overall film system[13][34][60]. Those results are however for a multilayer structure with up to 20 or more Bi-layers, which translates to a large number of interfaces for a given system thickness. This is not the case in the investigated coatings system. The influence of interfaces is therefore neglected in the discussion in this section.

In work published by Willey [36] and Begou [100] both modelled the stress of various metal films by using an equation which is based on the original work of Nordin and her colleagues [101]. In the original paper by Nordin et al.[101] the Force/width vs. thickness plots were fitted by a combined function consisting of a constant, a linear thickness dependency and two exponentially decaying sine functions, as can be seen below.

$$\frac{F}{w} = a + bt + f\sin(dt) * e^{-ct} + j\sin(ht) * e^{-gt} \quad (18)$$

The factors *a,b,c,d,f,g,* are fitting constants, the film thickness is represented by the letter *t* and *e* stands for the Euler's number. This model was further simplified to a linear approximation which allows for predicting the N/m for a thickness >20 nm for low mobility metals with a very high accuracy, as can be seen in [36].

The idea of approximating the N/m vs. thickness curve to be able to forecast the force per unit width is adapted for the result obtained in this thesis. The biggest difference however is that the results published for pure metals are only over the range of 200 nm. It seems nevertheless to be a valid approximation.

Modelling of N/m by the example of using Chromium

It should be noted first that the linear dependency of N/m with the film thickness in the first few nm presented in Figure 60 is used to show the connection between the film evolution and the force per unit width as it is presented in various publication [33][37][30][98]. The approach presented in this section is merely used to design the stress in layer stacks for coating development purposes only.

Since the deformation of the substrate (*Δh)* in relation to the film thickness, and therefore the sputtering time, follows a trend which can be described by a logarithmic function as can be seen in the following graph, the bending of the substrate can be predicted.

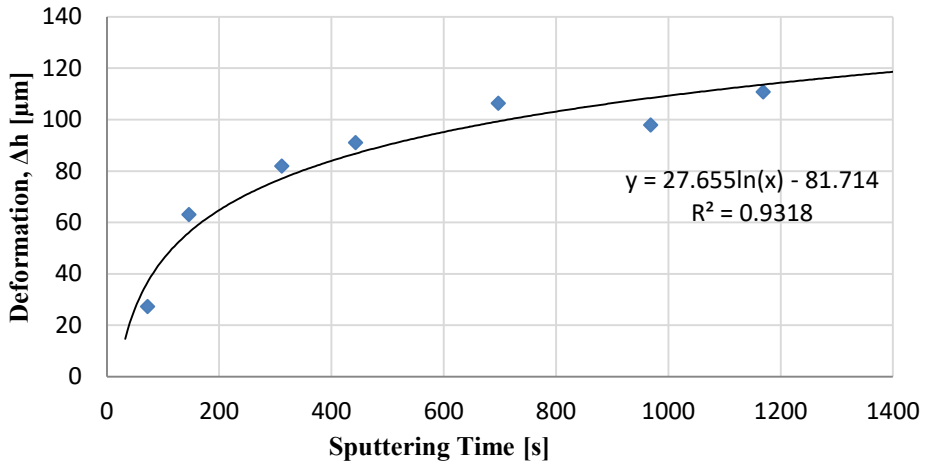

Figure 63. *Influence of sputtering time on the substrate deformation of Cr deposited with 5A at 1.0 x10^{-3} mbar.*

The used logarithmic fit function of the deformation has the form of

$$\Delta h = A * \ln(t) - B \qquad (19)$$

The constant have the values A=27.665 and B= 81.714, as can be seen by the fit overlaid in the graph. Considering now equation 13 from section 2.5.6 it can be shown that N/m, and hence the stress σ^f times the film thickness h_f, equal to the factor *k,* provided by the mechanical and geometrical properties of the substrate, times the substrate deformation *Δh.*

$$\sigma^f * h_f = k * \Delta h \qquad (20)$$

This relationship allows directly predicting the Force per unit width by the following equation with only using the substrate deformation[37][98].

$$\frac{F}{w} = A * k * \ln(t) - B * k \qquad (21)$$

An applied example of this is shown in the graph below. The calculated N/m, using the film thickens and the stress derived from Stoney formula is shown by the blue markers with its corresponding fit function. The constants of the fit function for the measured values, 46.009 and 135.95 can be derived from multiplying the constant A and B from equation 19 with the factor *k* (k= 1.66368), as pointed out by formula 20. Simultaneously the relationship of formula 21 is used to calculate the N/m by only using the substrate deformation is shown by the red markers. It can be seen that fitting the F/w values obtained by the calculation based on the stress values follows the trend of the directly measured F/w from the substrate deformation. This approach shows the connection between the substrate deformation and force per unit width given by the Stoney formula as it has been pointed out in the theory section 2.5.6

Determining the force per unit width in N/m without measuring directly the film thickness, which is prone to errors, has some advantageous. The first one is that it saves time. The second advantages, as it is discussed above in section 5.1, is the fact that the F/w value seems to be a more significant predictor of film stability and cracking than the stress value itself. It is nevertheless recognized that, with the sputtering time, an indirect relationship to the film thickness is provided.

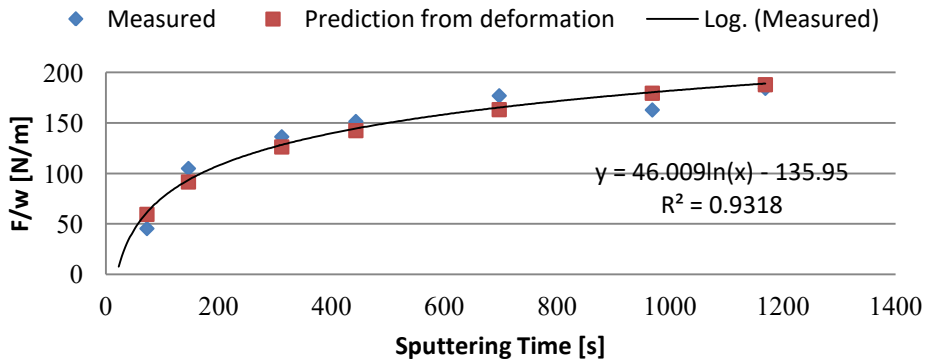

Figure 64. *Measured N/m and its fit function and the predicted N/m for chromium as indicated in the legend. This shows that N/m can be determined directly from the curvature measurement.*

Modelling of N/m by the example of using Zirconium

For the purpose of modelling the force per unit width, it is assumed that zirconium follows a linear dependency in the thickness range <300 nm. This assumption is based on the fact that

a) Zirconium is also a low mobility metal due to its high melting point of 1.855°C. So it is assumed that it behaves more or less similar to the materials published in [36]

b) The interrupted deposition of thin zirconium (4x40 s vs. 1x160 s layer, see Figure 38) adds up to the same N/m value, hence is more or less linear in this range.

Based on this, bending for zirconium in a range t_f <300 nm is fitted by a linear equation a can be seen below.

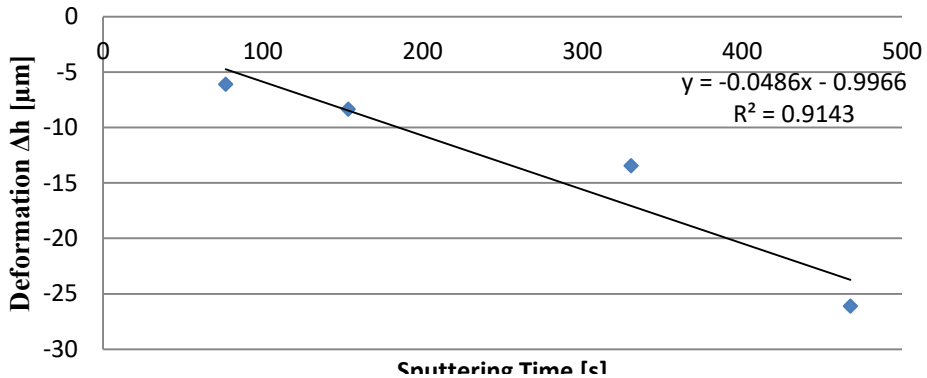

Figure 65. *Influence of sputtering time on the substrate deformation of Zr deposited with 8A at 1.0 x10^{-3} mbar*

The used fit function of the bending has the linear form of

$$\Delta h = -A * t - B \quad (22)$$

The constants have the values A=0.0486 and B= 0.9966, as can be seen by the fit overlaid in the graph. Following the same idea as pointed out for chromium above, the force per unit width can be predicted with using the following function and multiplying the constants A and B of function 22 again with factor k of the Stoney equation.

$$\frac{F}{w} = -A * k * t - B * k \quad (23)$$

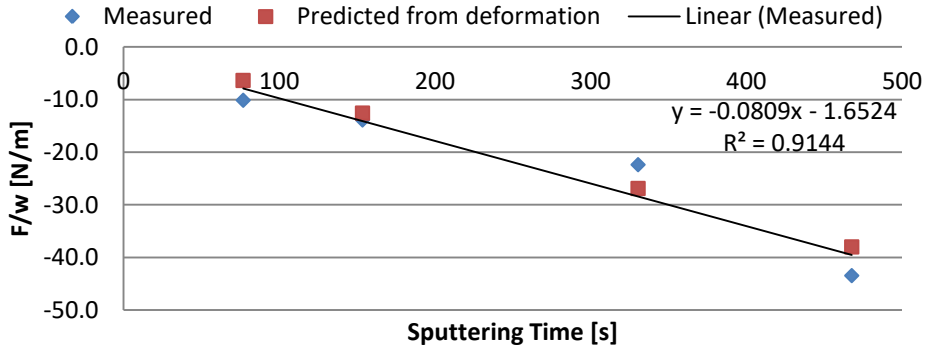

Figure 66. *Measured N/m and its fit function and the predicted N/m for zirconium. N/m can be determined directly from the curvature measurement.*

Using the same substrate for all coatings allows for finding a suitable coating which exerts the same but opposite moment and therefore curvature, on the substrate. If those two coatings are combined, in theory, those two forces should balance each other out, resulting in a layer stack which has an outward overall net stress of zero, since the forces are balanced. An important note is that this should not be confused with a non-existence of the internal stress of the single films, which is still present.

Achieving Zero stress in the PVD System

Using a chromium layer deposited at 5 A for 76 s as an adhesion layer and as a colour layer on top of the layer stack results in a total force of 90.8 N/m which needs to be balanced as can be seen from Table 9.

The single F/w is excreted by a zirconium layer deposited at 8 A for 160 s equals to 14 N/m. Dividing the force exerted by the two Cr layers (90.8 N/m) with the 14 N/m from the Zr equals to around ≈ 6.5 layers which need to be deposited to balance out the force of the Cr-layers. This would be equal to a total zirconium thickness of 840 nm as can be seen from Table 10. As already mentioned in the summary of the results, some problems with the target ignition came up during this part of the trails, as can be seen by the realized Ampere-second. Nevertheless, if one considers the reduced force as well as the resulting curvature it is evident that it is in relation to the amount of deposited Zr.

Taken this one step further one could use this approach also to predict how much Zr needs to be used the balance the force of the whole ePD® stack, including both lacquers. Before this, the experiment with the Zr should be repeated first to verify the underlying hypothesis of this approach.

5.7 Influence of UV coating on stress

As one can see by comparing the stress values of the lacquer in Figure 39, it is evident that the residual stress values of the investigated UV films are within the reported values found in various publications [10][11]. However, by comparing the F/w values of base and topcoat in Figure 40, with values measured for the PVD coatings, it is clear that the lacquers exert a larger amount of force than the PVD coatings. Based on the gained knowledge about the importance of F/w, this stands in contrast to the initial assumption, that the lacquers do not play an important role. However, the initial assumption was based on stress and not F/w. In a lacquer/PVD system, this raises the question, how the exerted force is dissipated if the substrate is too thick/stiff and does not allow bending as pointed out in section 2.5.7.

One possible idea is that the interfacial stress force transferred from the topcoat to the PVD coating causes cracking in the PVD film. This would be the case if the adhesion force between the PVD and the lacquer is higher than the force exerted by the UV coating, which allows for the transfer of the force. Secondly, the cohesion of the PVD film

needs to be lower than the transferred force to allow for cracking. The exact influence of the force exerted by the lacquers as well as the lacquer deposition process on the stress in the ePD® system is left open at this point and offers opportunities for extensive research in the future.

6. CONCLUSION

The effect of deposition parameters on the microstructure, phase and surface morphology with a focus on the development of residual stress of zirconium and chromium was successfully studied using several characterization methods. Those methods included SEM, XRD, substrate curvature and nanoindentation. The investigated process parameter included sputtering time, target current, sputtering pressure, substrate rotation speed and interrupted deposition. Since glass substrates were used in this work, an effect of the substrate structure on the investigated properties is believed to be neglectable. This should allow transferring the obtained results to the polymer substrate, which however needs to be checked in further studies. Based on obtained results, it was possible to predict the force, the film exerts. Furthermore it was tried to balance the occurring tensile stress / force of the chromium film by a compressive component of the zirconium film. This endeavour was only partly successful, since the chosen sputtering program for zirconium did no run properly. However, a trend of a reduction in tensile force was observed, which correlated with the film thickness, as it was expected. Thus, this work provides a solid base to further investigate the influence of various deposition parameters on the development of residual stress for chromium and zirconium films, also in respect to tailoring the residual stress in a layer-stack system.

The following conclusions can be drawn as a summary of this thesis:

- The substrate bending method for very thin films was established and its accuracy and repeatability was shown.
- The surface sensitive XRD stress measurement method was adopted from the literature and the advantageous for the very thin film (<100 nm) over the conventional Bragg-Brentano setup was shown.
- It was shown that the use of macroscopic XEC, obtained from nanoindentation, yields similar stress result for the XRD stress and bending method respectively.
- An almost “single crystal like” structure for thicker Cr film was observed, which is believed to be the cause of an anisotropic stress development for those films. Contrary to his, thinner chromium films (<100 nm) show a rotational symmetry in their stress development and a (110)-fiber texture.
- Zirconium showed a change in film structure with an increase in film thickness. It is assumed that this change is responsible for the difference in observed stress with the film thickness. This result also could be linked to the change in stress for the interrupted deposition process.

- A strong dependence of the zirconium phase from either sputtering pressure, residual oxygen and/or probably the power density was observed. Since the causality is not clear yet and only few results are published for metallic zirconium, this phenomenon needs further investigation.
- It was possible to explain the results and the measured residual stress by the available mechanisms and stress models, suggested by literature.
- It seems that above certain critical thickness (t_c), the force exerted by the chromium film is higher than the adhesion and or/cohesion of the PVD film, which resulted in cracks and flaking of the film. This is represented by a plateau in the N/m curve.
- The direct link between the substrate deformation and the force per unit width based on the Stoney formula was shown. This allowed deriving the F/w directly from the curvature without the necessity of measuring the film thickness. It was furthermore concluded that F/w is a more significant predictor for film stability than stress
- A dependency of force per unit width (F/w) with the film thickness was found for both materials, which can be described by a mathematical function. This allows tailoring the individual thickness to design the outward stress of the layer stack

7. OUTLOOK

Even though some challenges were faced with the coating deposition system during this work, it seems that the force per unit width can be predicted to a certain extend with the found relationships. This is true for the single layers as well as for the layer stack. Therefore it would be of high interest to repeat similar experiments to further prove the validity of the stress/force prediction for the whole layer stack system, including both UV coatings.

It was found out in this work that zirconium can be present in an amorphous or a crystalline phase within the range of technical relevant process parameters. For coating development it would be beneficial to understand the factors which influence this difference, to be able to control the growth as well as the possible different residual stress which arise from this.

For chromium, a strong connection of the texture and anisotropic stress to film thickness was observed. This was mainly attributed to shadowing as a result of substrate rotation and using elongated targets. This aspect needs to be investigated further. In addition, a thorough investigation of the influence of the deposition parameter on the texture development as well as the emergence of the “single crystal like” structure for thicker Cr films, can be of high interest.

Finally, as a further step, it is also interesting to find out how the lacquers influence stress in the films. Here the influence of the basecoat on the growth and stress of the PVD film is of importance, as well as how the topcoat application process and the topcoat itself affect the stress in the PVD films.

REFERENCES

[1] G. Vergason and M. Fitch, “Replacing Decorative Electroplated Chrome on Plastics Coatings —,” *Soc. Vac. Coaters Bull.*, vol. 3, no. 2, pp. 32–37, 2013.

[2] J. T. Eich, E. Weber, P. Abell, and C. Mack, “Opportunities for Functional Design Using Physical Vapor Deposition and UV-Curable Coatings,” in *RadTech Report*, 2014, pp. 1–6.

[3] K. Wagner and J. R. Smith, “Exterior UV-Curable Topcoat For Physical Vapor Deposition Applications,” in *Society of Plastics Engineers*, 2009, no. 2, pp. 832–835.

[4] Surface Engineering Association, “REACH and the impact of Hexavalent Chromium.” [Online]. Available: http://www.sea.org.uk/en/blog/the-reach-directive-and-the-implications-to-the-surface-engineering-industry.cfm. [Accessed: 07-Jun-2017].

[5] I. Kolev, “Coatings on Plastics — Technology Designed for a Wide Range of Solutions,” *Soc. Vac. Coaters*, vol. 3, no. 2, pp. 42–43, 2013.

[6] Oerlikon Balzers, “ePD & Inubia I Chrome Looking Plastic Metallisation on a New Level,” p. 8.

[7] D. M. Mattox, “History Corner A Short History : Adhesion, Interface,Formation and Stress in PVD Coatings,” *Soc. Vac. Coaters*, no. Summer, pp. 32–37, 2016.

[8] Insight Global Market, “Plating on Plastics (POP) Market Size,” 2016. [Online]. Available: https://www.gminsights.com/industry-analysis/plating-on-plastics-POP-market. [Accessed: 07-Jun-2017].

[9] E. Weber and P. Abell, “UV-Curable Basecoats and Clearcoats for Automotive Lighting,” in *RadTech Report*, 2003, no. 6, pp. 1–7.

[10] D. M. Vaessen, F. A. Ngantung, M. L. B. Palacio, and L. F. Francis, “Effect of Lamp Cycling on Conversion and Stress Development in Ultraviolet-Cured Acrylate Coatings,” *J. Appl. Polym. Sci.*, vol. 84, pp. 2784–2793, 2002.

[11] O. O. Knudsen, A. Bjorgum, T. Frydenberg, and R. Johnsen, “Development of Internal Stress in Organic Coatings during Curing and Exposure,” *CORROSION*, pp. 2–11, 2006.

[12] M. J. Cordill, A. Taylor, J. Schalko, and G. Dehm, “Fracture and Delamination of Chromium Thin Films on Polymer Substrates,” *Metall. Mater. Trans. A*, vol. 41, no. 4, pp. 870–875, 2010.

[13] G. C. A. M. Janssen, “Stress and strain in polycrystalline thin films,” *Thin Solid Films*, vol. 515, no. 17, pp. 6654–6664, 2007.

[14] jobaTECGmbH and Vergason Technology Inc., “SUPERCHROME PVD Coating A green alternative for,” in *SUPERCHROME PVD Coating- A green alternative for chromium-galvanized plastic components*, 2015, p. 17.

[15] D. M. Mattox, *Handbook of Physical Vapor Deposition (PVD) Processing*, 2nd ed. Elsevier Inc., 2010.

[16] M. Ohring, *Material Science of Thin Films*, 2nd ed. Academic Press, 2002.

[17] I. Petrov, P. B. Barna, L. Hultman, and J. E. Greene, “Microstructural evolution during film growth,” *J. Vac. Sci. Technol. A Vacuum, Surfaces, Film.*, vol. 21, no. 5, pp. S117–S128, 2003.

[18] S. L. Rohde, “Sputter Deposition,” *ASM Handbook.*, vol. 5, pp. 93–123, 1994.
[19] J. L. Perry, “Effects of sputter deposition parameters on stress in tantalum films with applications to chemical mechanical planarization of copper,” Rochester Institute of Technology, Master Thesis, 2004.
[20] N. D. Bergshoeff, “Microstructure analysis of PVD deposited thin copper films,” Eindhoven University of Technology, Project Report 2011.
[21] D. Skinner, “UV Curing in the Plastic, Components Industry,” *RadTech Rep.*, no. August, pp. 19–23, 2003.
[22] R. Haftung, “Terra Gloss UV Lacke.” ACTEGA Terra GmbH, Lehrte Germany.
[23] J. Almer, G. Hakanson, and M. Oden, “The effects of bias voltage and annealing on the microstructure and residual stress of arc-evaporated Cr–N coatings,” *Surf. Coatings Technol.*, vol. 121, pp. 272–276, 1999.
[24] J. W. Hutchinson, “Stresses and failure modes in thin films and multi-layers,” Technical University of Denmark, Lecture Notes, 1997.
[25] F. Elstner, C. Gautier, O. Piot, and J. Machet, “A Comparative Study of Structure and Residual Stress in Chromium Nitride Films Deposited by Vacuum Arc Evaporation , Ion Plating , and DC Magnetron Sputtering,” vol. 505, pp. 505–521, 1996.
[26] A. Anders, “A structure zone diagram including plasma-based deposition and ion etching,” *Thin Solid Films*, vol. 518, no. 15, pp. 4087–4090, 2010.
[27] P. . Barna and M. Adamik, “Fundamental structure forming phenomena of polycrystalline films and the structure zone models,” *Thin Solid Films*, vol. 317, no. 1–2, pp. 27–33, 1998.
[28] B. Eigenmann and E. Macherauch, “Rontgenographische Untersuchung von Spannungszustanden in Werkstoffen- Teil 1,” *Materwiss. Werksttech.*, vol. 26, pp. 148–160, 1995.
[29] M. Tümmler, “Röntgenografische Spannungsuntersuchungen an Schichtsystemen,” Technische Universität Ilmenau, Lecture Notes, 2008.
[30] E. Chason and P. R. Guduru, “Tutorial: Understanding residual stress in polycrystalline thin films through real-time measurements and physical models,” *J. Appl. Phys.*, vol. 119, no. 19, 2016.
[31] E. Chason, “A kinetic analysis of residual stress evolution in polycrystalline thin films,” *Thin Solid Films*, vol. 526, pp. 1–14, 2012.
[32] E. Chason, M. Karlson, J. J. Colin, D. Magnfält, K. Sarakinos, and G. Abadias, “A kinetic model for stress generation in thin films grown from energetic vapor fluxes,” *J. Appl. Phys.*, vol. 119, no. 14, 2016.
[33] S. Hong, “Dependence of stress and morphology of sputtered copper films on deposition conditions,” Rochester Institute of Technology, 1988.
[34] F. Spaepen, “Interfaces and stresses in thin films,” *Acta Mater.*, vol. 48, no. 1, pp. 31–42, 2000.
[35] L. B. Freund and S. Suresh, *Thin Film Materials - Stress, Defect Formation and Surface Evolution*, 1st ed. Cambridge University Press, 2003.
[36] R. R. Willey and W. Optical, “Procedure for Designing Optical Coatings to Control Stress,” in *57th Annual Technical Conference Proceedings*, 2014, pp. 1–6.
[37] G. Abadias, A. Fillon, J. J. Colin, A. Michel, and C. Jaouen, “Real-time stress evolution during early growth stages of sputter-deposited metal films: Influence of adatom mobility,” *Vacuum*, vol. 100, no. 2, pp. 36–40, 2014.
[38] E. B. Dolgusheva and V. Y. Trubitsin, “Study of peculiarities of the thermal expansion of zirconium thin films by molecular-dynamics simulation,” *Comput.*

Mater. Sci., vol. 111, pp. 231–238, 2016.
[39] E. B. Dolgusheva and V. Y. Trubitsin, "Lattice Parameters and Thermal Expansion of Zirconium Thin Films," *Proc. Int. Conf. Nanomater. Appl. Prop.*, vol. 2, no. 1, pp. 2–4, 2013.
[40] B. Usmani, V. Vijay, R. Chhibber, and A. Dixit, "Optimization of sputtered zirconium thin films as an infrared reflector for use in spectrally-selective solar absorbers," *Thin Solid Films*, vol. 627, no. 7, pp. 17–25, 2017.
[41] L. Pichon, T. Girardeau, F. Lignou, and A. Straboni, "Evidence of w -phase in ion beam sputtered zirconium thin films," *Thin Solid Films*, vol. 342, no. 1–2, pp. 93–99, 1999.
[42] R. J. Drese and M. Wuttig, "In situ stress measurements in zirconium and zirconium oxide films prepared by direct current sputtering," *J. Appl. Phys.*, vol. 99, no. 12, 2006.
[43] J. Chakraborty, K. K. Kumar, S. Mukherjee, and S. K. Ray, "Stress, texture and microstructure of zirconium thin films probed by X-ray diffraction," *Thin Solid Films*, vol. 516, no. 23, pp. 8479–8486, 2008.
[44] T. Jörg, M. J. Cordill, R. Franz, O. Glushko, J. Winkler, and C. Mitterer, "The electro-mechanical behavior of sputter-deposited Mo thin films on flexible substrates," *Thin Solid Films*, vol. 606, no. 1, pp. 45–50, 2016.
[45] T. Chiang, P. Ding, B. L. Chin, and B. Sun, "Stress tunable tantalum and foreign patent documents Tantalum nitride films," US 6488823 B1, 1994.
[46] J. Lin, J. J. Moore, W. D. Sproul, B. Mishra, and Z. Wu, "Modulated pulse power sputtered chromium coatings," *Thin Solid Films*, vol. 518, no. 5, pp. 1566–1570, 2009.
[47] M. Panjan, M. Čekada, P. Panjan, F. Zupanič, and W. Kölker, "Dependence of microstructure and hardness of TiAlN/VN hard coatings on the type of substrate rotation," *Vacuum*, vol. 86, no. 6, pp. 699–702, 2012.
[48] A. O. Eriksson *et al.*, "Layer formation by resputtering in Ti-Si-C hard coatings during large scale cathodic arc deposition," *Surf. Coatings Technol.*, vol. 205, no. 15, pp. 3923–3930, 2011.
[49] N. Panich and Y. Sun, "Effect of substrate rotation on structure, hardness and adhesion of magnetron sputtered TiB2 coating on high speed steel," *Thin Solid Films*, vol. 500, no. 1–2, pp. 190–196, 2006.
[50] J. A. Thornton and D. W. Hoffman, "Internal Stresses in Sputtered Chromium," *Thin Solid Films*, vol. 40, no. 1, pp. 355–363, 1977.
[51] L. S. Suominen, C. Zhou, M. A. Korhonen, and C. Y. Li, "X-ray study of Residual Stresses in thin Chromium Metallization on Glass Substrates," in *Denver X-ray Conference on Applications of X-ray Analysis*, 1997, no. 1, pp. 1–8.
[52] T. Karabacak, J. J. Senkevich, G.-C. Wang, and T.-M. Lu, "Stress reduction in sputter deposited films using nanostructured compliant layers by high working-gas pressures," *J. Vac. Sci. Technol. A Vacuum, Surfaces, Film.*, vol. 23, no. 4, pp. 986–990, 2005.
[53] M. C. K. Tinone, T. Haga, and H. Kinoshita, "Multilayer sputter deposition stress control," *J. Electron Spectros. Relat. Phenomena*, vol. 80, no. 1, pp. 461–464, 1996.
[54] C. Q. Guo, Z. L. Pei, D. Fan, R. D. Liu, J. Gong, and C. Sun, "Predicting multilayer film's residual stress from its monolayers," *Mater. Des.*, vol. 110, no. 1, pp. 858–864, 2016.
[55] J. G. Ockenfuss and B. Pond, "Low Net Stress Multilayer Thin Film Optical

Filter," US 2006/0087739, 2006.
[56] A. E. Spiller, B. P. Mirkarimi, C. Montcalm, S. Bajit, and A. J. Flota, "Method to adjust mutlilayer film stress induced deformation of optics," US006134049A, 2000.
[57] R. Nothhelfer-Richter, "Reducing tensions: Mechanical characteristics of UV clear coats," *Farbe und Lack*, vol. 117, no. 8, pp. 16–19, 2011.
[58] C. H. Hare, "Internal Stress : Part I," *J. Prot. Coatings Linings*, pp. 65–75, 1996.
[59] J. B. Oliver *et al.*, "Stress compensation in hafnia/silica optical coatings by inclusion of alumina layers," *Opt. Express*, vol. 20, no. 15, p. 16596, 2012.
[60] R. C. Cammarata, "Surface and Interface Stress Effects In Thin Films," *Prog. Surf. Sci.*, vol. 46, no. 1, pp. 1–38, 1994.
[61] B. Heine, *Werkstoffprüfung Ermittlung der Eigenschaften metallischer Werkstoffe*, 3rd ed. Carl Hanser Verlag GmbH & Co. KG, 2015.
[62] M. E. Fitzpatrick, A. T. Fry, P. Holdway, F. A. Kandil, J. Shackleton, and L. Suominen, "Determination of Residual Stresses by X-ray Diffraction - Issue 2," *A Natl. Meas. Good Pract. Guid.*, vol. 52, no. 2, p. 77, 2005.
[63] J. D. Rachwal, "X-ray diffraction applications in thin films and (100) silicon substrate stress analysis," *Univ. South Florida*, no. 100, p. 88, 2010.
[64] T. Manns and B. Scholtes, "Eine Software zur Berechnung diffraktionselastischer Konstanten aus Einkristalldaten A software for the calculation of diffraction elastic constants from single crystal," *HTM J. Heat Treat. Mater.*, vol. 65, pp. 75–84, 2010.
[65] A. C. Vermeulen, "An Elastic Constants Database and XEC Calculator for use in XRD Residual Stress Analysis," in *Denver X-ray Conference (DXC) on Applications of X-ray Analysis*, 2001, vol. 44, pp. 128–133.
[66] "Zerstörungsfreie Prüfung – Röntgendiffraktometrisches Prüfverfahren zur Ermittlung der Eigenspannungen," *DIN EN 15305*, 2008.
[67] C. Ma, J. Huang, and H. Chen, "Residual stress measurement in textured thin film by grazing-incidence X-ray diffraction Residual stress measurement in textured thin film by grazing-incidence X-ray diffraction," *Thin Solid Films*, vol. 418, no. 1, pp. 73–78, 2002.
[68] S. Wroński, K. Wierzbanowski, A. Baczmański, and A. Lodini, "X-ray grazing incidence technique - Corrections in Residual stress measurement - A review," *Denver X-ray Conf. Appl. X-ray Anal.*, vol. 16, no. 1, pp. 1–7, 2009.
[69] A. N. Wang, J. H. Huang, H. W. Hsiao, G. P. Yu, and H. Chen, "Residual stress measurement on TiN thin films by combing nanoindentation and average X-ray strain (AXS) method," *Surf. Coatings Technol.*, vol. 280, no. 1, pp. 43–49, 2015.
[70] M. Birkholz, P. F. Fewster, and C. Genzel, "Thin Film Analysis by X-ray Scattering," Weinheim: Wiley-VCH, 2005, pp. 155–165.
[71] O. Engler and V. Randles, *Introduction to Texture Analysis*, 2nd ed. Boca Raton: CRC Press Taylor & Francis Group, 2010.
[72] K. Nagao and E. Kagami, "X-ray thin film measurement techniques: VII. Pole figure measurement," *Rigaku J.*, vol. 27, no. 2, pp. 6–14, 2011.
[73] N. Schwarzer and F. Richter, "On the Determination of Film Stress from Substrate Bending: STONEY's Formula and Its Limits," *Whitepaper*, no. 1, pp. 1–17, 2006.
[74] D. M. Broadway *et al.*, "Achieving zero stress in iridium, chromium and nickel thin films," in *SPIE Optics + Optoelectronics*, 2015, pp. 1–16.
[75] K. Long, I.-C. Cheng, a Kattamis, H. Gleskova, S. Wagner, and J. C. Sturm, "Amorphous-silicon thin-film transistors made at 28°C on clear-plastic substrates

by interfacial stress engineering," *J. Soc. Inf. Disp.*, vol. 15, no. 3, pp. 167–176, 2007.

[76] W. C. Oliver and G. M. Pharr, "An improved technique for determining hardness and elastic modulus using load and displacement sensing indentation experiments," *Journal of Materials Research*, vol. 7, no. 6. pp. 1564–1583, 1992.

[77] A. R. Franco Jr., G. Pintaúde, A. Sinatora, C. E. Pinedo, and A. P. Tschiptschin, "The use of a vickers indenter in depth sensing indentation for measuring elastic modulus and vickers hardness," *Mater. Res.*, vol. 7, no. 3, pp. 483–491, 2004.

[78] N. Bierwisch and M. Fuchs, "Tutorial for Test Optimizer," in *Saxonian Institute of Surface Mechanics-Manual*, 2013, pp. 1–4.

[79] "Glass in building - Special basic products - Borosilicate glasses - Part 1-1: Definitions and general physical and mechanical properties," *DIN EN 1748-1-12004-12*, 2004.

[80] Präzisions Glas & Optik GmbH, "PGO Online." [Online]. Available: https://www.pgo-online.com/intl/mempax.html. [Accessed: 19-Jun-2017].

[81] J. H. Hubbell and S. M. Seltzer, "X-Ray Mass Attenuation Coefficients." [Online]. Available: https://www.nist.gov/pml/x-ray-mass-attenuation-coefficients. [Accessed: 29-Jun-2017].

[82] PDF-card No. 85-1336., *ICCD- International Centre for Diffraction Data*. 2004.

[83] PDF-card No. 34-0657., *ICCD- International Centre for Diffraction Data*. 2004.

[84] K.-H. Hellwege, *Landolt-Börnstein. Numerical Data and Functional Relationships in Science and Technology. New Series. Group III: Crystal and Solid State Physics*, 3rd ed. Springer Berlin, 1979.

[85] Unknown, "Chromium —Structure and Elastic Properties," *Materials & Design*, vol. 1, pp. 1–4, 2008.

[86] PDF-card No. 05-0665., *ICCD- International Centre for Diffraction Data*. 2004.

[87] C. V. Thompson and R. Carel, "Stress and grain growth in thin films," *J. Mech. Phys. Solids*, vol. 44, no. 5, pp. 657–673, 1996.

[88] G. C. A. M. Janssen and P. F. A. Alkemade, "Anisotropic growth of chromium films during sputter deposition on substrates in planetary motion," *J. Vac. Sci. Technol. A Vacuum, Surfaces, Film.*, vol. 22, no. 4, pp. 1773–1777, 2004.

[89] G. C. A. M. Janssen and J. D. Kamminga, "Stress in hard metal films," *Appl. Phys. Lett.*, vol. 85, no. 15, pp. 3086–3088, 2004.

[90] Y. C. Feng, D. . Laughlin, and D. . Lambeth, "Formation of crystellographic texture in RF sputter-deposited Cr thin films," *J. Appl. Phys.*, vol. 76, no. 11, pp. 7311–7316, 1994.

[91] O. . Krapenko, J. . Bilelli, and S. . Yalisove, "Combined transmission electron microscopy and x-ray study of the microstructure and texture in sputtered Mo films," vol. 76, no. 8, pp. 4610–4617, 1994.

[92] "IEEE micro electro mechanical systems : an investigation of micro structures, sensors, actuators, machines and robots," in *IEEE, MicroElectroMechanical Systems Workshop*, 1990, p. 174.

[93] F. Ferreira, R. Serra, J. C. Oliveira, and A. Cavaleiro, "Effect of peak target power on the properties of Cr thin films sputtered by HiPIMS in deep oscillation magnetron sputtering (DOMS) mode," *Surf. Coatings Technol.*, vol. 258, pp. 249–256, 2014.

[94] S. G. Mayr and K. Samwer, "Model for intrinsic stress formation in amorphous thin films," *Phys. Rev. Lett.*, vol. 87, no. 3, pp. 361051–361054, 2001.

[95] E. Chason, B. W. Sheldon, L. B. Freund, J. A. Floro, and S. J. Hearne, "Origin of Compressive Residual Stress in Polycrystalline Thin Films," *Phys. Rev. Lett.*,

vol. 88, no. 15, p. 156103, 2002.

[96] L. P. H. Jeurgens, W. G. Sloof, F. D. Tichelaar, and E. J. Mittemeijer, “Thermodynamic stability of amorphous oxide films on metals: Application to aluminum oxide films on aluminum substrates,” *Phys. Rev. B*, vol. 62, no. 7, pp. 4707–4719, 2000.

[97] H. Fager, *Growth and Characterization of Amorphous Multicomponent Nitride Thin Films*, no. August. 2014.

[98] A. Fillon, G. Abadias, A. Michel, and C. Jaouen, “Stress and microstructure evolution during growth of magnetron-sputtered low-mobility metal films: Influence of the nucleation conditions,” *Thin Solid Films*, vol. 519, no. 5, pp. 1655–1661, 2010.

[99] S. Huang and X. Zhang, “Extension of the Stoney formula for film-substrate systems with gradient stress for MEMS applications,” *J. Micromechanics Microengineering*, vol. 16, no. 2, pp. 382–389, 2006.

[100] T. Begou and J. Lumeau, “Accurate analysis of mechanical stress in dielectric multilayers,” *Opt. Lett.*, vol. 42, no. 16, 2017.

[101] M. Nordin, M. Larsson, T. Joelsson, and J. Birch, “Residual stress formation in multilayered TiN/TaNx coatings during reactive magnetron sputter deposition,” *J. Vac. Sci. Technol. A Vacuum, Surfaces, Film.*, vol. 18, no. 6, pp. 2884–2889, 2000.

APPENDIX 1: STRESS FREE AL2O3 SAMPLE

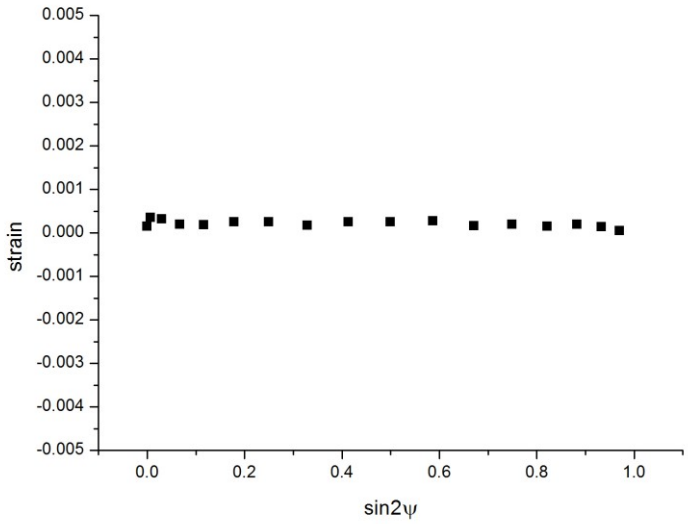

Sin2ψ plot of a stress free Al2O3 reference sample

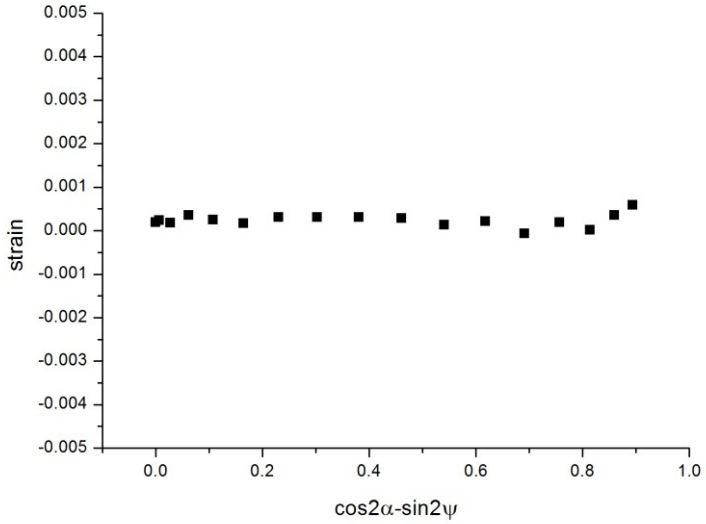

Cos2αSin2ψ Plot of a stress free Al2O3 reference sample

APPENDIX 2: COATING STRUCTURE

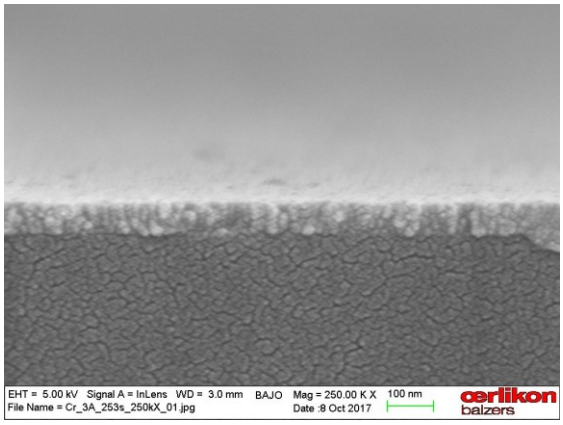

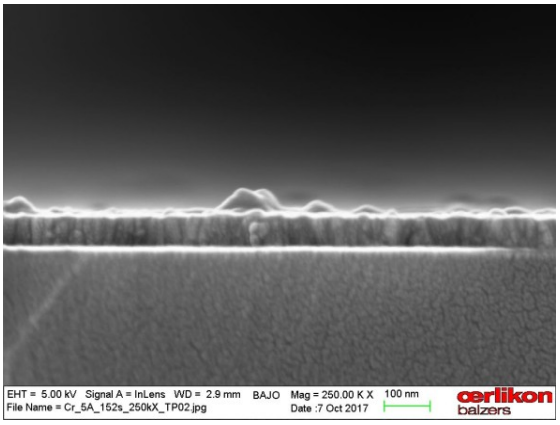

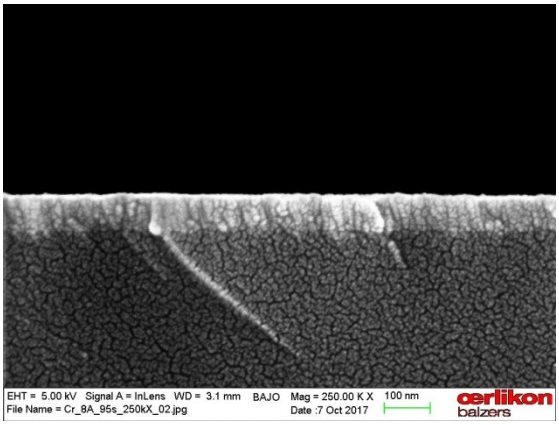

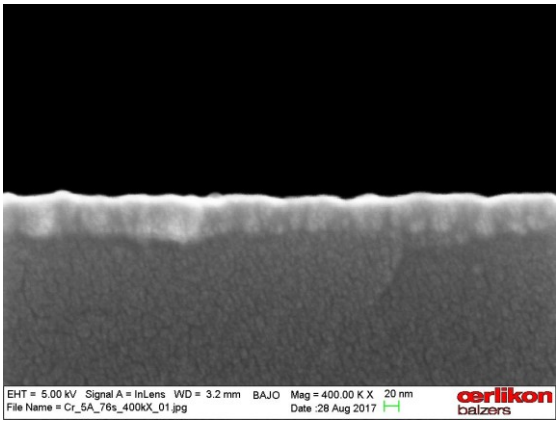

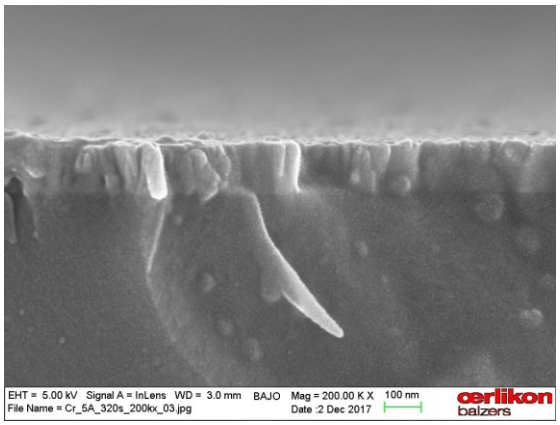

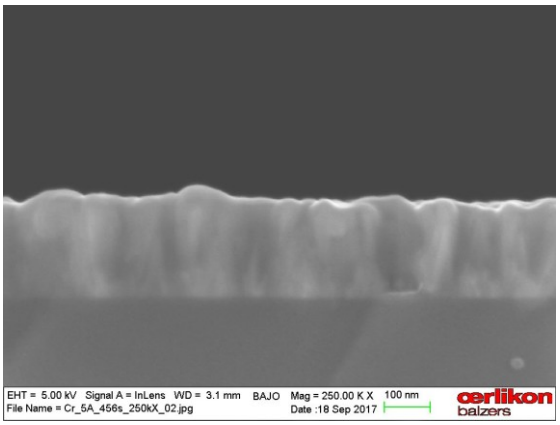

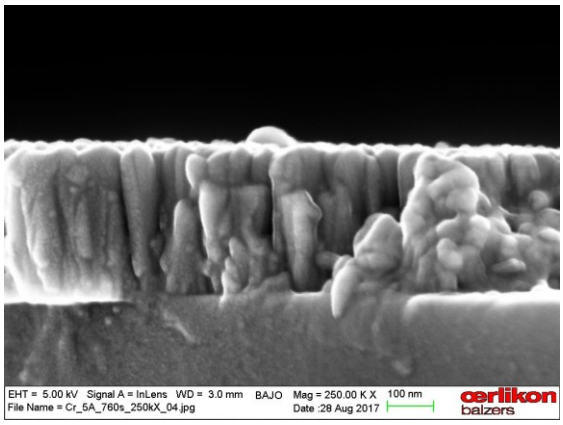
EHT = 5.00 kV Signal A = InLens WD = 3.0 mm BAJO Mag = 250.00 K X 100 nm
File Name = Cr_5A_760s_250kX_04.jpg Date :28 Aug 2017
oerlikon balzers

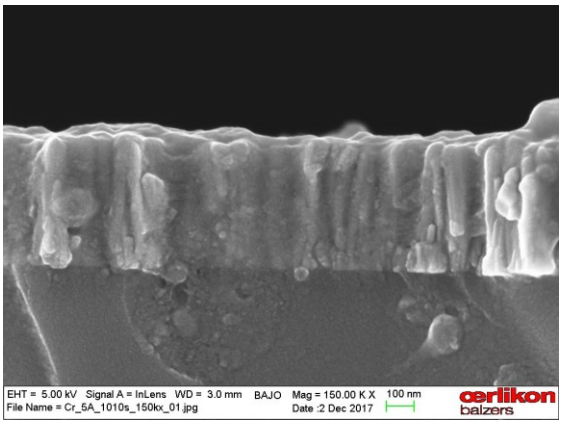
EHT = 5.00 kV Signal A = InLens WD = 3.0 mm BAJO Mag = 150.00 K X 100 nm
File Name = Cr_5A_1010s_150kx_01.jpg Date :2 Dec 2017
oerlikon balzers

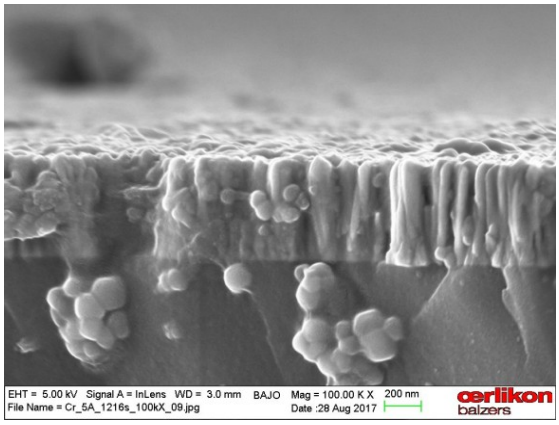
EHT = 5.00 kV Signal A = InLens WD = 3.0 mm BAJO Mag = 100.00 K X 200 nm
File Name = Cr_5A_1216s_100kX_09.jpg Date :28 Aug 2017
oerlikon balzers

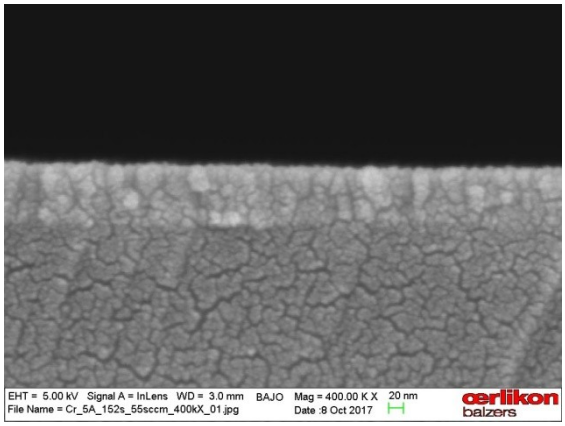
EHT = 5.00 kV Signal A = InLens WD = 3.0 mm BAJO Mag = 400.00 K X 20 nm
File Name = Cr_5A_152s_55sccm_400kX_01.jpg Date :8 Oct 2017
oerlikon balzers

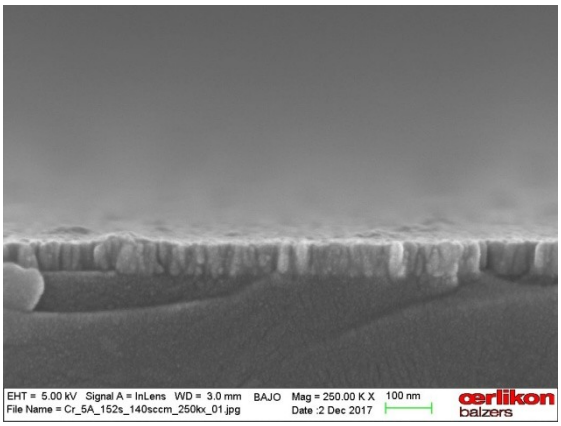
EHT = 5.00 kV Signal A = InLens WD = 3.0 mm BAJO Mag = 250.00 K X 100 nm
File Name = Cr_5A_152s_140sccm_250kx_01.jpg Date :2 Dec 2017
oerlikon balzers

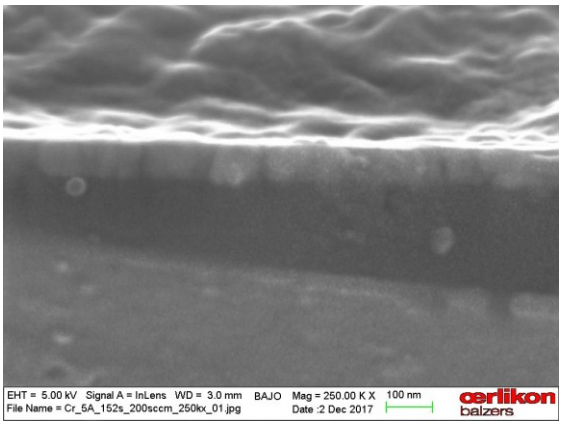
EHT = 5.00 kV Signal A = InLens WD = 3.0 mm BAJO Mag = 250.00 K X 100 nm
File Name = Cr_5A_152s_200sccm_250kx_01.jpg Date :2 Dec 2017
oerlikon balzers

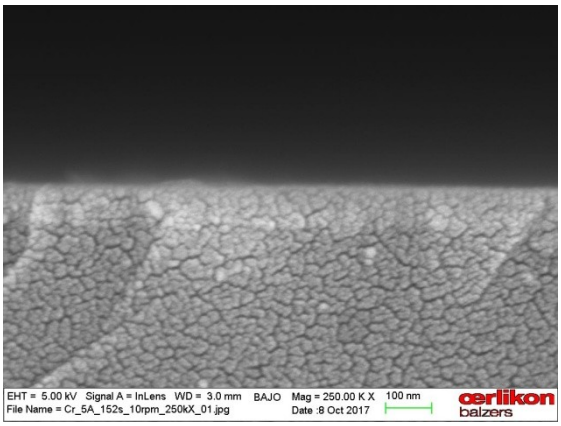
EHT = 5.00 kV Signal A = InLens WD = 3.0 mm BAJO Mag = 250.00 K X 100 nm
File Name = Cr_5A_152s_10rpm_250kX_01.jpg Date :8 Oct 2017
oerlikon balzers

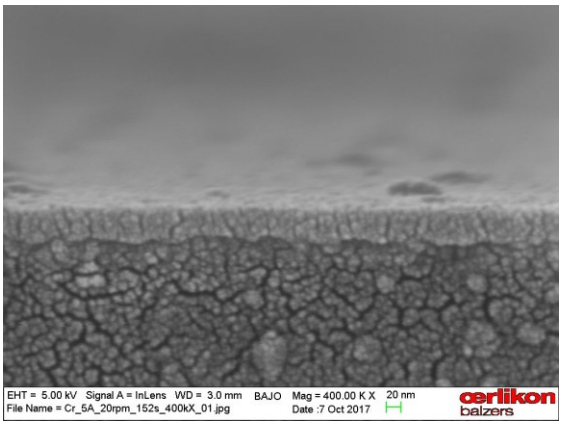
EHT = 5.00 kV Signal A = InLens WD = 3.0 mm BAJO Mag = 400.00 K X 20 nm
File Name = Cr_5A_20rpm_152s_400kX_01.jpg Date :7 Oct 2017
oerlikon balzers

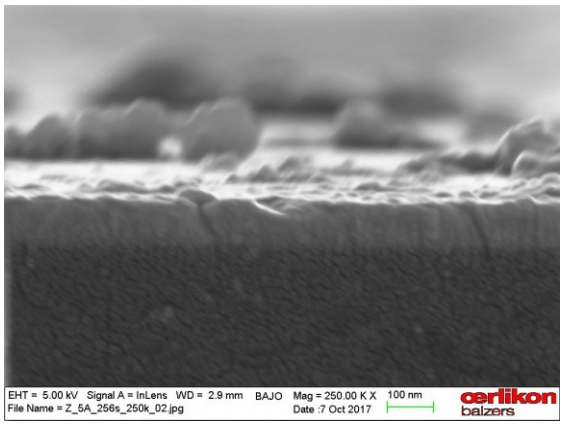
EHT = 5.00 kV Signal A = InLens WD = 2.9 mm BAJO Mag = 250.00 K X 100 nm
File Name = Z_5A_256s_250k_02.jpg Date :7 Oct 2017
oerlikon balzers

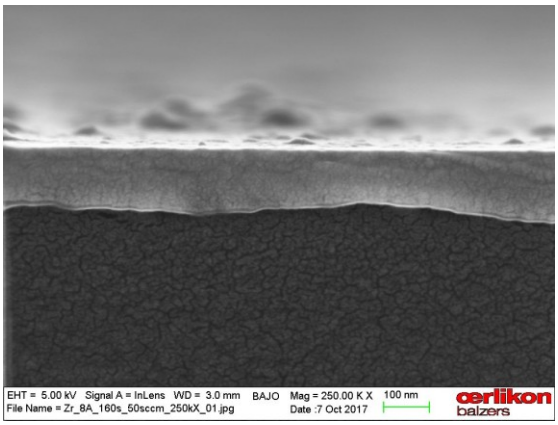
EHT = 5.00 kV Signal A = InLens WD = 3.0 mm BAJO Mag = 250.00 K X 100 nm
File Name = Zr_8A_160s_50sccm_250kX_01.jpg Date :7 Oct 2017
oerlikon balzers

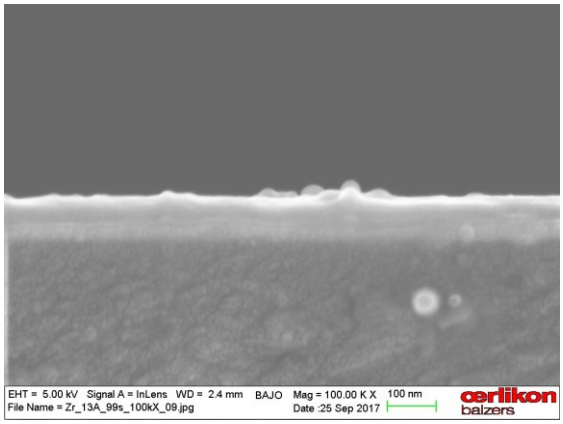
EHT = 5.00 kV Signal A = InLens WD = 2.4 mm BAJO Mag = 100.00 K X 100 nm
File Name = Zr_13A_99s_100kX_09.jpg Date :25 Sep 2017
oerlikon balzers

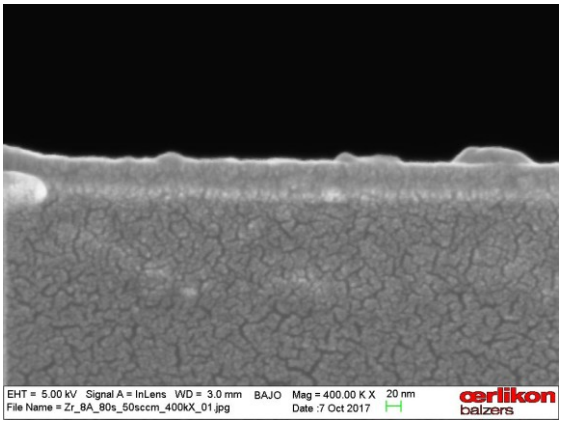
EHT = 5.00 kV Signal A = InLens WD = 3.0 mm BAJO Mag = 400.00 K X 20 nm
File Name = Zr_8A_80s_50sccm_400kX_01.jpg Date :7 Oct 2017
oerlikon balzers

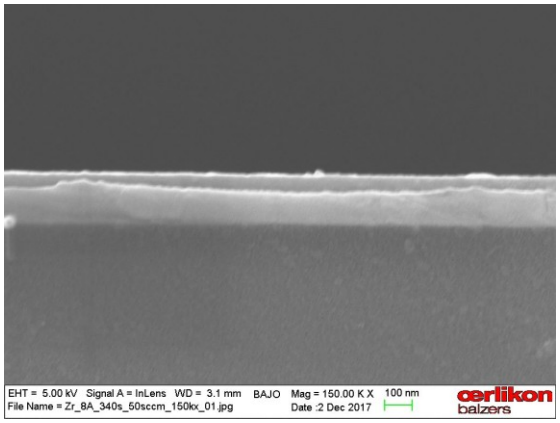
EHT = 5.00 kV Signal A = InLens WD = 3.1 mm BAJO Mag = 150.00 K X 100 nm
File Name = Zr_8A_340s_50sccm_150kx_01.jpg Date :2 Dec 2017
oerlikon balzers

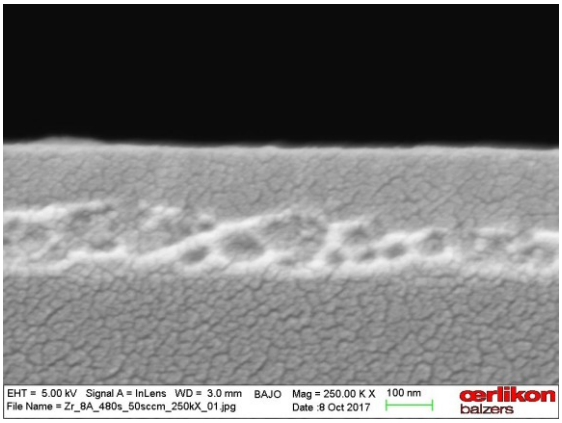
EHT = 5.00 kV Signal A = InLens WD = 3.0 mm BAJO Mag = 250.00 K X 100 nm
File Name = Zr_8A_480s_50sccm_250kX_01.jpg Date :8 Oct 2017
oerlikon balzers

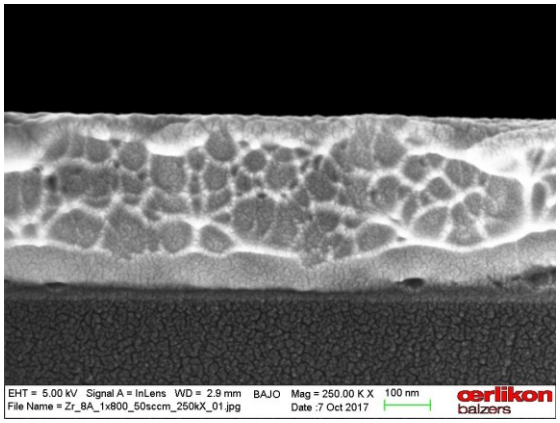
EHT = 5.00 kV Signal A = InLens WD = 2.9 mm BAJO Mag = 250.00 K X 100 nm
File Name = Zr_8A_1x800_50sccm_250kX_01.jpg Date :7 Oct 2017
oerlikon balzers

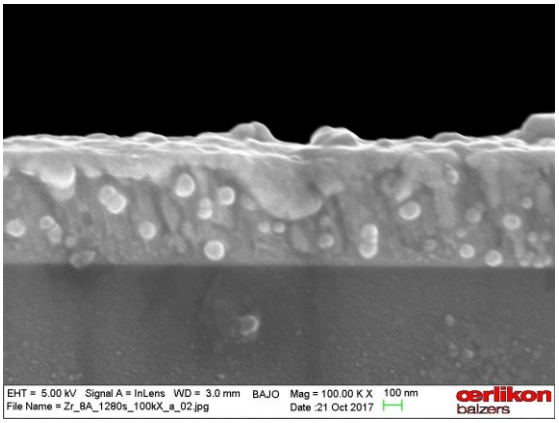
EHT = 5.00 kV Signal A = InLens WD = 3.0 mm BAJO Mag = 100.00 K X 100 nm
File Name = Zr_8A_1280s_100kX_a_02.jpg Date :21 Oct 2017
oerlikon balzers

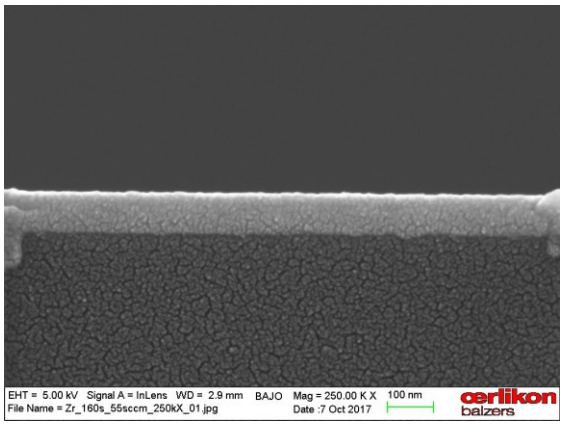
EHT = 5.00 kV Signal A = InLens WD = 2.9 mm BAJO Mag = 250.00 K X 100 nm
File Name = Zr_160s_55sccm_250kX_01.jpg Date :7 Oct 2017
oerlikon balzers

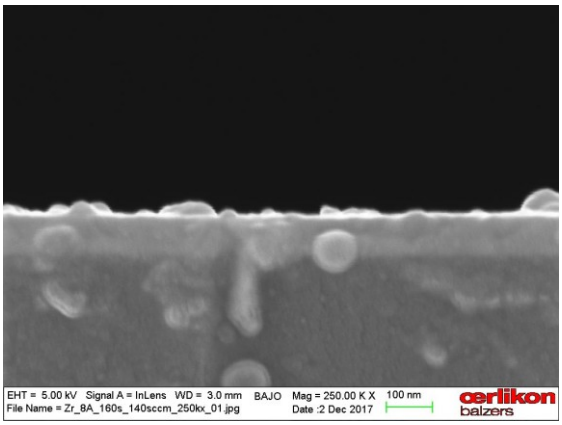
EHT = 5.00 kV Signal A = InLens WD = 3.0 mm BAJO Mag = 250.00 K X 100 nm
File Name = Zr_8A_160s_140sccm_250kx_01.jpg Date :2 Dec 2017
oerlikon balzers

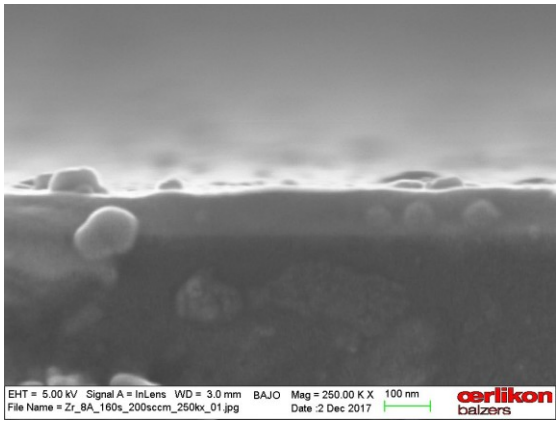
EHT = 5.00 kV Signal A = InLens WD = 3.0 mm BAJO Mag = 250.00 K X 100 nm
File Name = Zr_8A_160s_200sccm_250kx_01.jpg Date :2 Dec 2017
oerlikon balzers

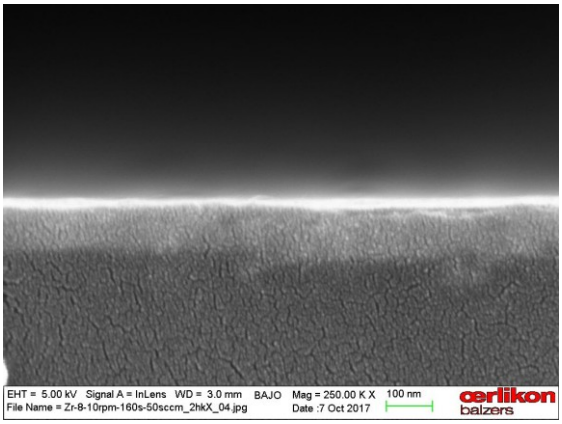
EHT = 5.00 kV Signal A = InLens WD = 3.0 mm BAJO Mag = 250.00 K X 100 nm
File Name = Zr-8-10rpm-160s-50sccm_2hkX_04.jpg Date :7 Oct 2017
oerlikon balzers

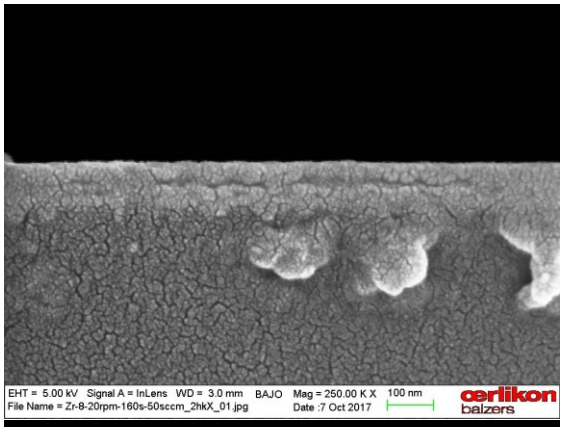
EHT = 5.00 kV Signal A = InLens WD = 3.0 mm BAJO Mag = 250.00 K X 100 nm
File Name = Zr-8-20rpm-160s-50sccm_2hkX_01.jpg Date :7 Oct 2017
oerlikon balzers

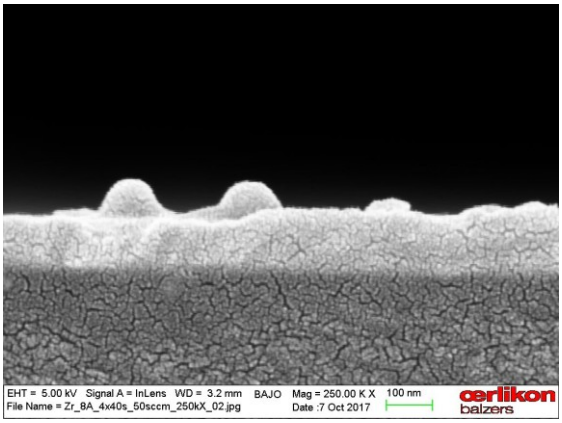
EHT = 5.00 kV Signal A = InLens WD = 3.2 mm BAJO Mag = 250.00 K X 100 nm
File Name = Zr_8A_4x40s_50sccm_250kX_02.jpg Date :7 Oct 2017
oerlikon balzers

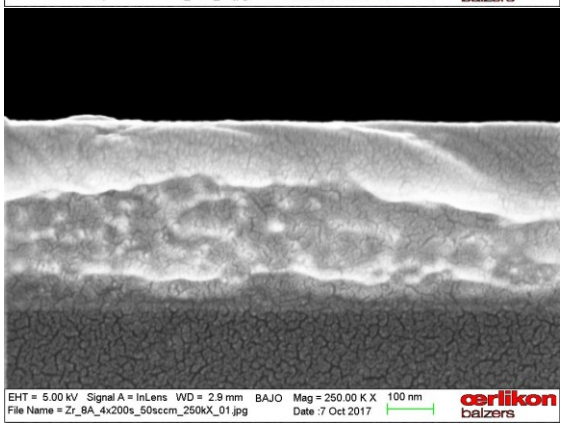
EHT = 5.00 kV Signal A = InLens WD = 2.9 mm BAJO Mag = 250.00 K X 100 nm
File Name = Zr_8A_4x200s_50sccm_250kX_01.jpg Date :7 Oct 2017
oerlikon balzers

APPENDIX 3: COATING MORPHOLOGY

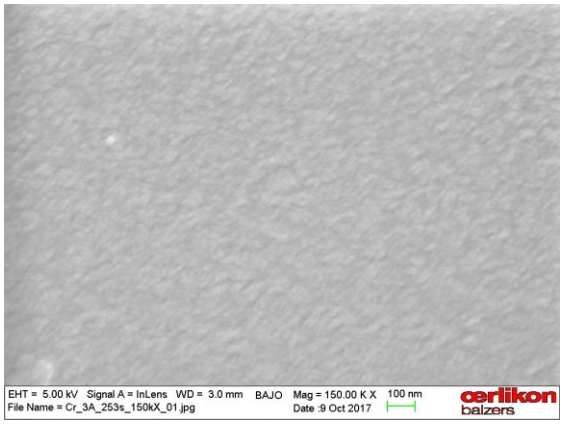

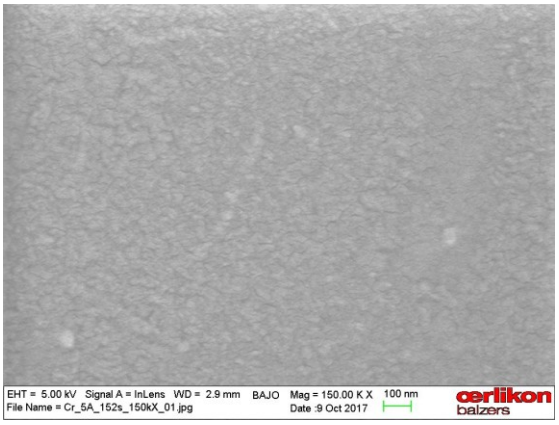

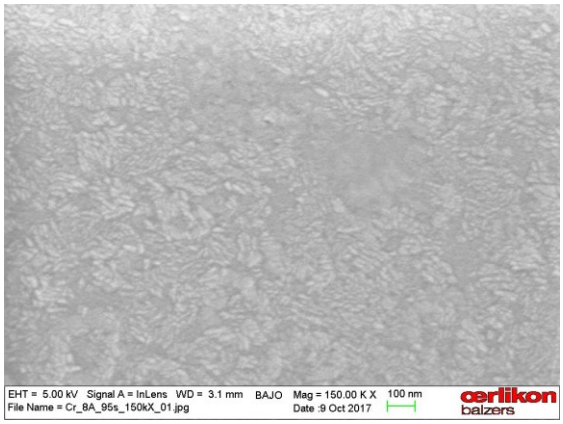

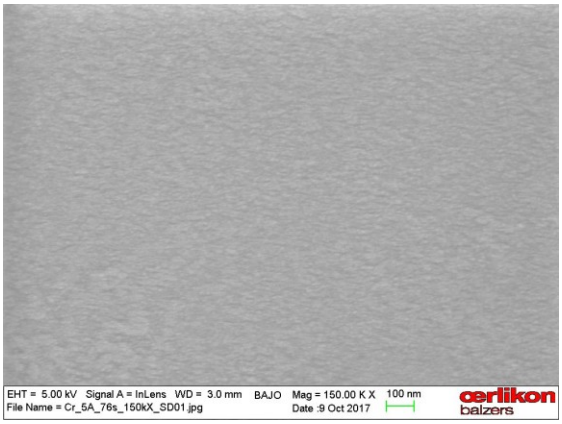

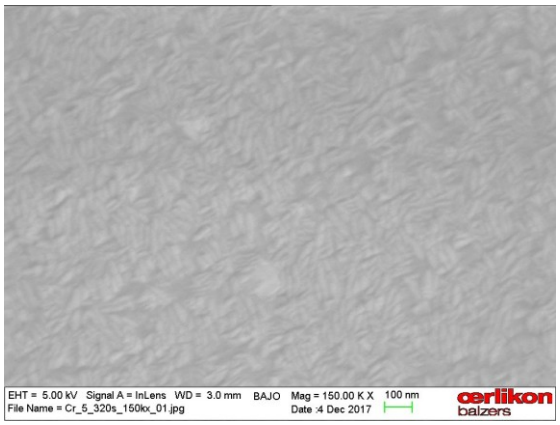

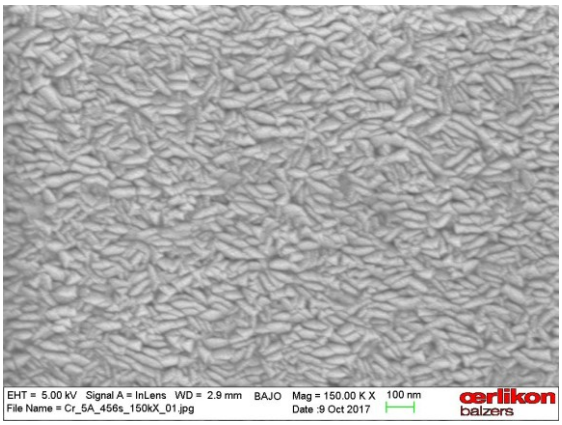

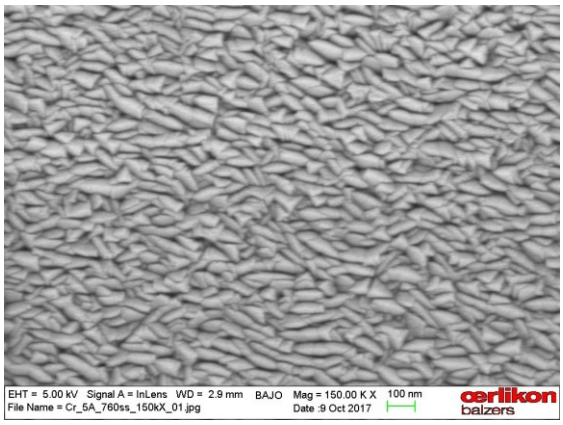
EHT = 5.00 kV Signal A = InLens WD = 2.9 mm BAJO Mag = 150.00 K X 100 nm
File Name = Cr_5A_760ss_150kX_01.jpg Date :9 Oct 2017
oerlikon balzers

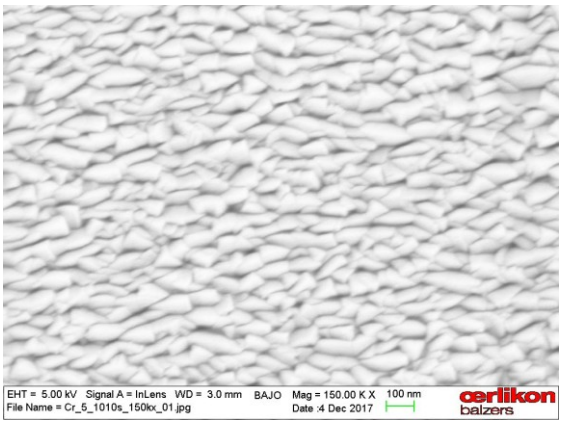
EHT = 5.00 kV Signal A = InLens WD = 3.0 mm BAJO Mag = 150.00 K X 100 nm
File Name = Cr_5_1010s_150kx_01.jpg Date :4 Dec 2017
oerlikon balzers

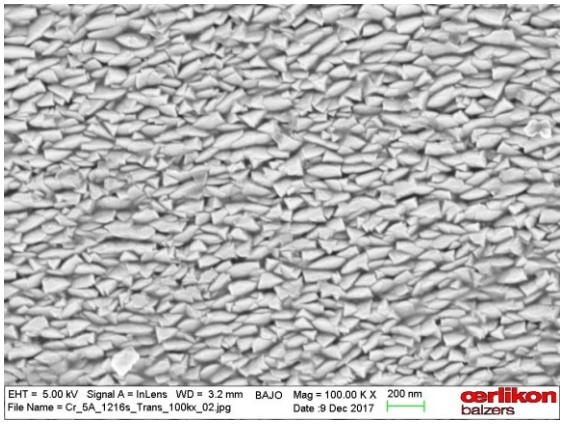
EHT = 5.00 kV Signal A = InLens WD = 3.2 mm BAJO Mag = 100.00 K X 200 nm
File Name = Cr_5A_1216s_Trans_100kx_02.jpg Date :9 Dec 2017
oerlikon balzers

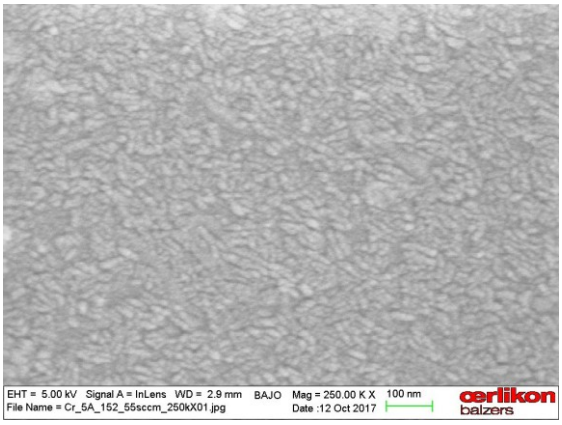
EHT = 5.00 kV Signal A = InLens WD = 2.9 mm BAJO Mag = 250.00 K X 100 nm
File Name = Cr_5A_152_55sccm_250kX01.jpg Date :12 Oct 2017
oerlikon balzers

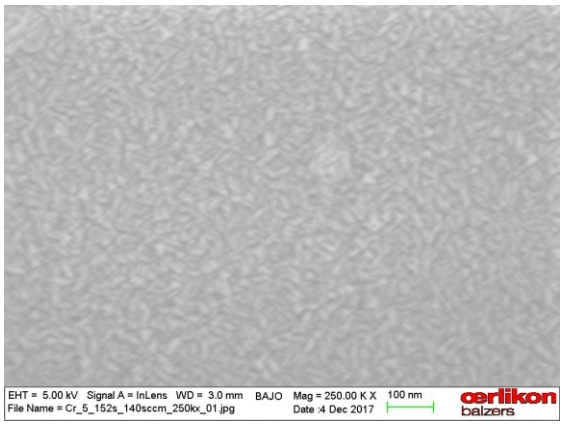
EHT = 5.00 kV Signal A = InLens WD = 3.0 mm BAJO Mag = 250.00 K X 100 nm
File Name = Cr_5_152s_140sccm_250kx_01.jpg Date :4 Dec 2017
oerlikon balzers

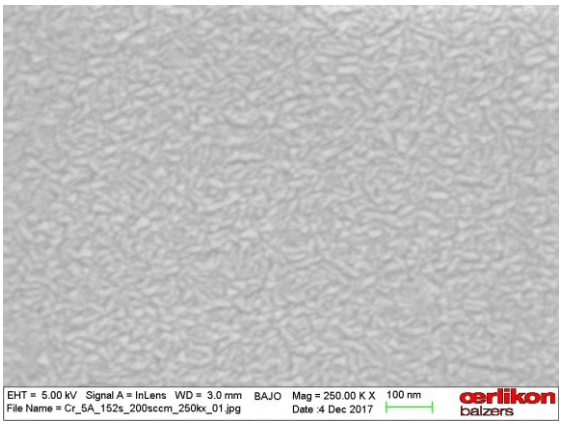
EHT = 5.00 kV Signal A = InLens WD = 3.0 mm BAJO Mag = 250.00 K X 100 nm
File Name = Cr_5A_152s_200sccm_250kx_01.jpg Date :4 Dec 2017
oerlikon balzers

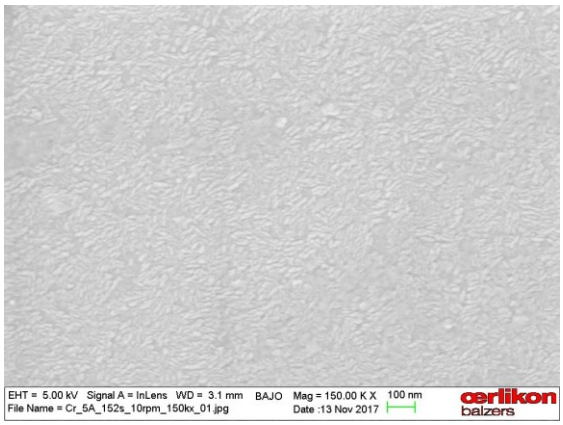
EHT = 5.00 kV Signal A = InLens WD = 3.1 mm BAJO Mag = 150.00 K X 100 nm
File Name = Cr_5A_152s_10rpm_150kx_01.jpg Date :13 Nov 2017
oerlikon balzers

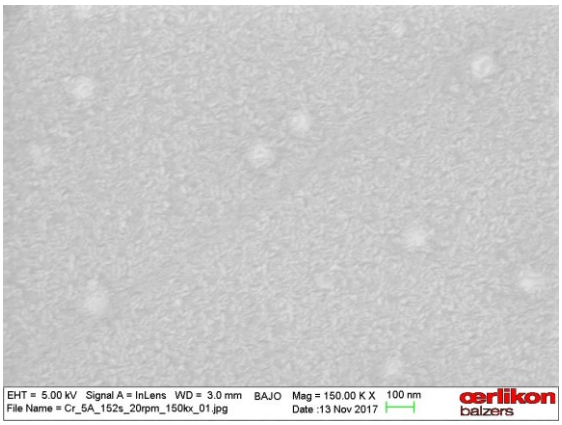
EHT = 5.00 kV Signal A = InLens WD = 3.0 mm BAJO Mag = 150.00 K X 100 nm
File Name = Cr_5A_152s_20rpm_150kx_01.jpg Date :13 Nov 2017
oerlikon balzers

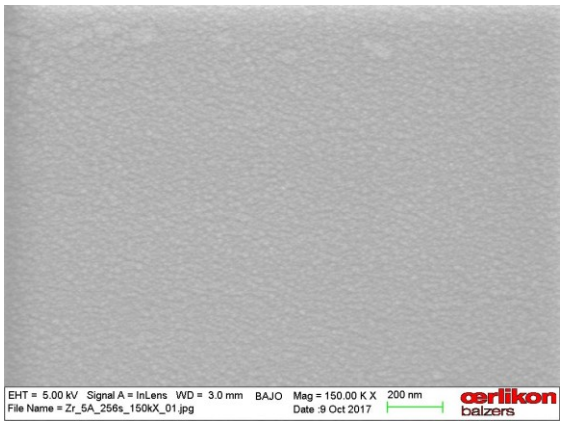
EHT = 5.00 kV Signal A = InLens WD = 3.0 mm BAJO Mag = 150.00 K X 200 nm
File Name = Zr_5A_256s_150kX_01.jpg Date :9 Oct 2017
oerlikon balzers

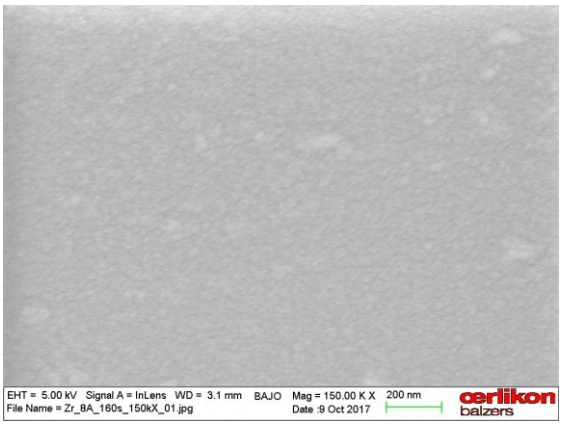
EHT = 5.00 kV Signal A = InLens WD = 3.1 mm BAJO Mag = 150.00 K X 200 nm
File Name = Zr_8A_160s_150kX_01.jpg Date :9 Oct 2017
oerlikon balzers

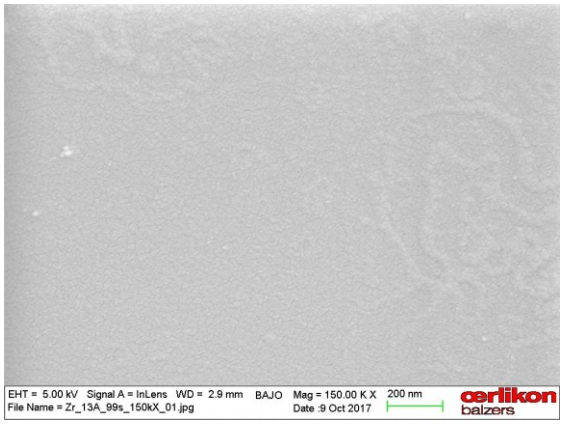
EHT = 5.00 kV Signal A = InLens WD = 2.9 mm BAJO Mag = 150.00 K X 200 nm
File Name = Zr_13A_99s_150kX_01.jpg Date :9 Oct 2017
oerlikon balzers

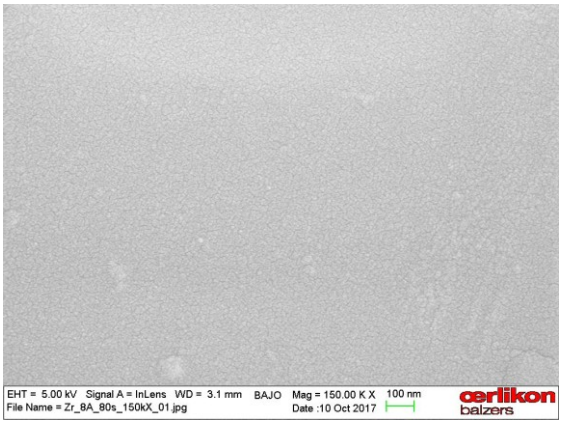
EHT = 5.00 kV Signal A = InLens WD = 3.1 mm BAJO Mag = 150.00 K X 100 nm
File Name = Zr_8A_80s_150kX_01.jpg Date :10 Oct 2017
oerlikon balzers

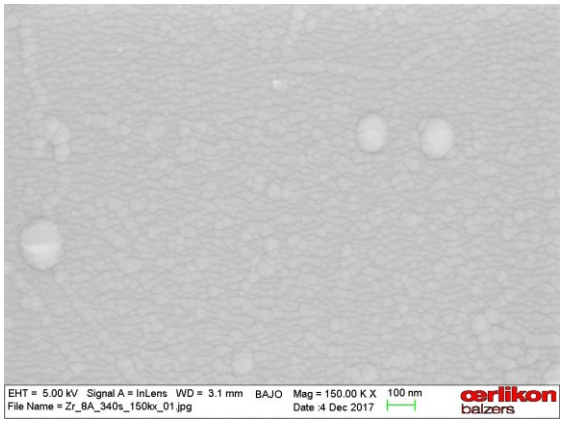
EHT = 5.00 kV Signal A = InLens WD = 3.1 mm BAJO Mag = 150.00 K X 100 nm
File Name = Zr_8A_340s_150kx_01.jpg Date :4 Dec 2017
oerlikon balzers

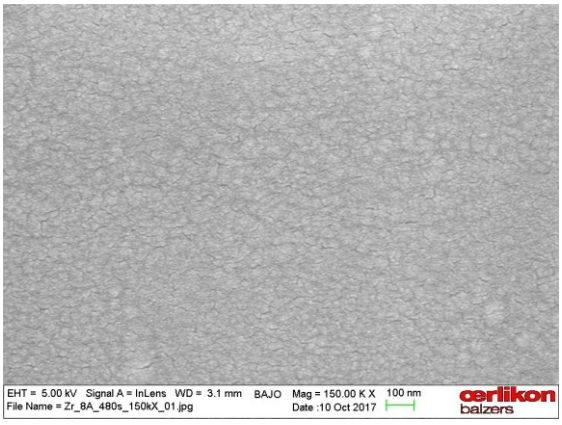
EHT = 5.00 kV Signal A = InLens WD = 3.1 mm BAJO Mag = 150.00 K X 100 nm
File Name = Zr_8A_480s_150kX_01.jpg Date :10 Oct 2017
oerlikon balzers

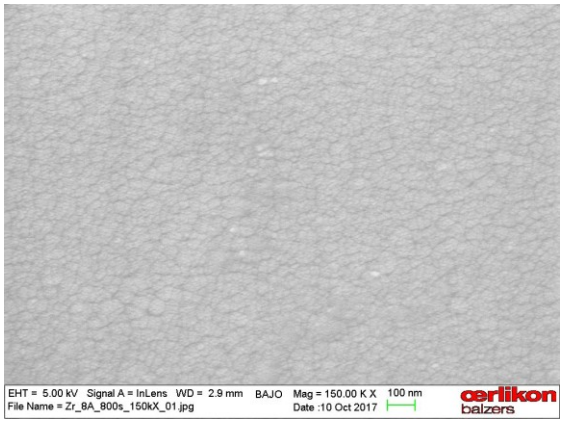
EHT = 5.00 kV Signal A = InLens WD = 2.9 mm BAJO Mag = 150.00 K X 100 nm
File Name = Zr_8A_800s_150kX_01.jpg Date :10 Oct 2017
oerlikon balzers

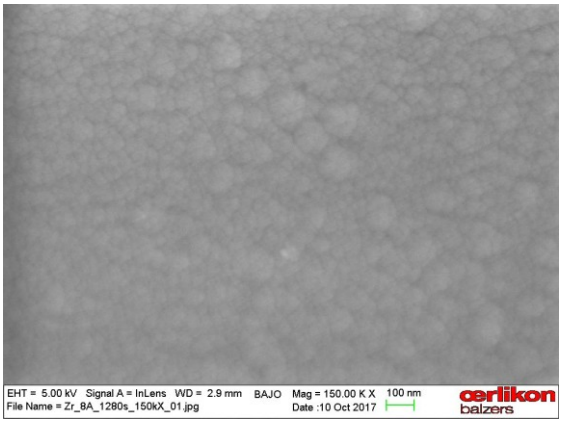
EHT = 5.00 kV Signal A = InLens WD = 2.9 mm BAJO Mag = 150.00 K X 100 nm
File Name = Zr_8A_1280s_150kX_01.jpg Date :10 Oct 2017
oerlikon balzers

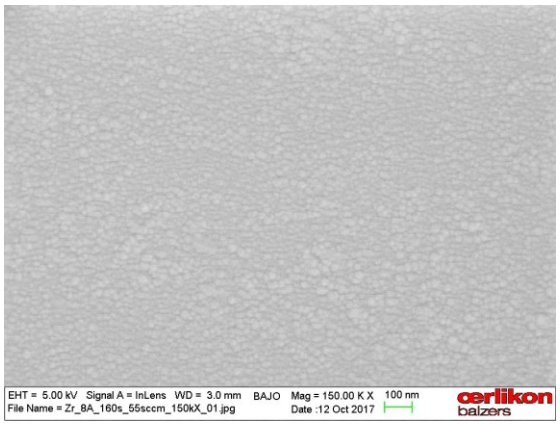
EHT = 5.00 kV Signal A = InLens WD = 3.0 mm BAJO Mag = 150.00 K X 100 nm
File Name = Zr_8A_160s_55sccm_150kX_01.jpg Date :12 Oct 2017
oerlikon balzers

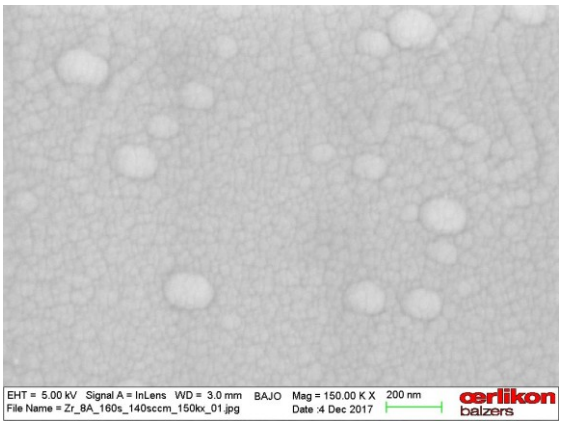
EHT = 5.00 kV Signal A = InLens WD = 3.0 mm BAJO Mag = 150.00 K X 200 nm
File Name = Zr_8A_160s_140sccm_150kx_01.jpg Date :4 Dec 2017
oerlikon balzers

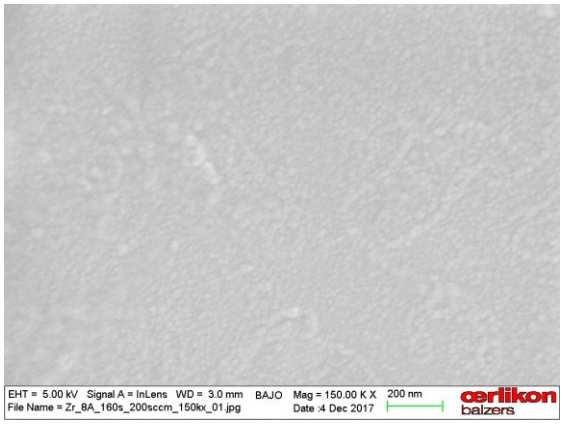
EHT = 5.00 kV Signal A = InLens WD = 3.0 mm BAJO Mag = 150.00 K X 200 nm
File Name = Zr_8A_160s_200sccm_150kx_01.jpg Date :4 Dec 2017
oerlikon balzers

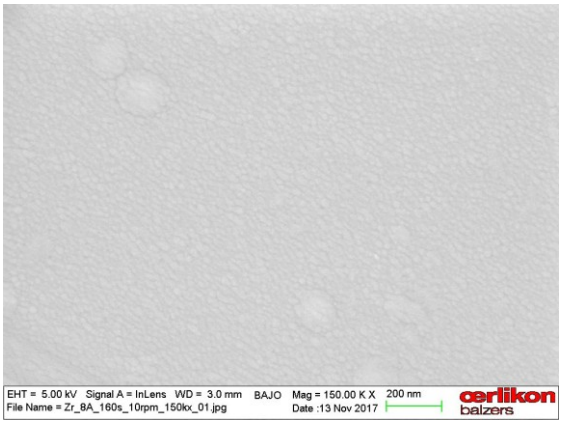
EHT = 5.00 kV Signal A = InLens WD = 3.0 mm BAJO Mag = 150.00 K X 200 nm
File Name = Zr_8A_160s_10rpm_150kx_01.jpg Date :13 Nov 2017
oerlikon balzers

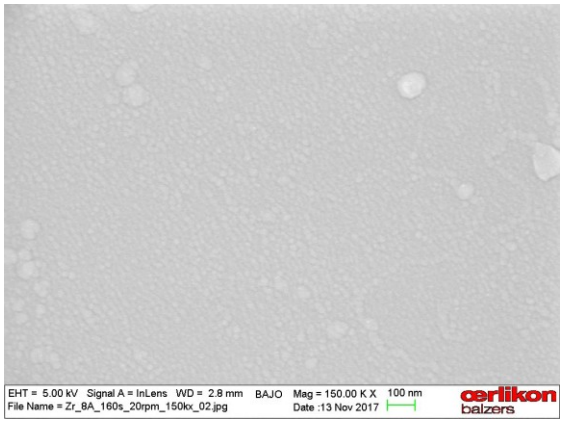
EHT = 5.00 kV Signal A = InLens WD = 2.8 mm BAJO Mag = 150.00 K X 100 nm
File Name = Zr_8A_160s_20rpm_150kx_02.jpg Date :13 Nov 2017
oerlikon balzers

APPENDIX 4: XRD RESULTS

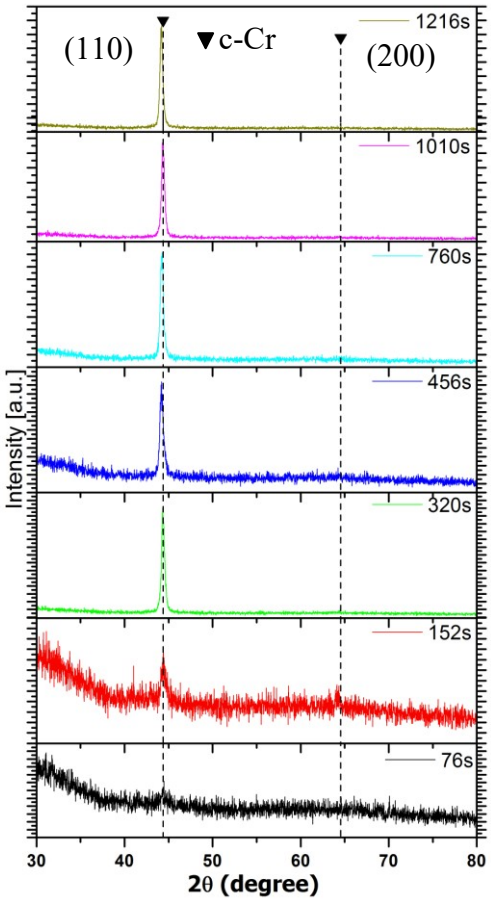

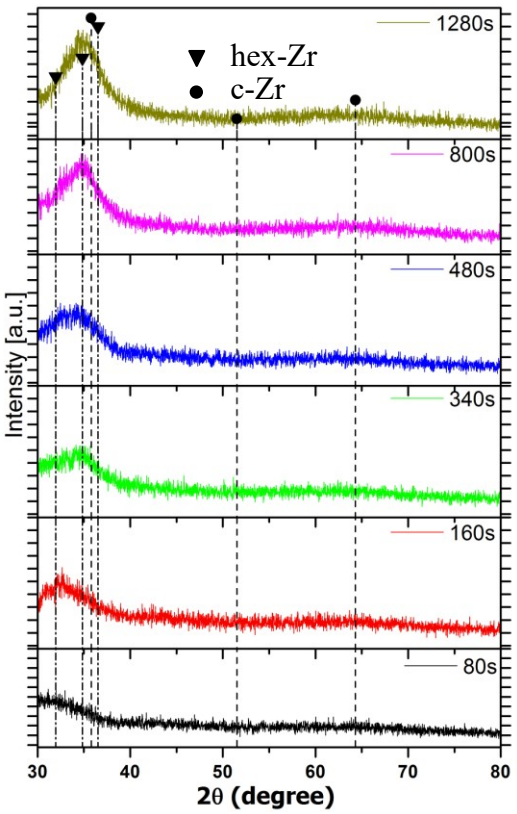

Change in the T2T pattern of Cr with the sputtering time (left). Change in the T2T Pattern of Zr with the sputtering time (right)

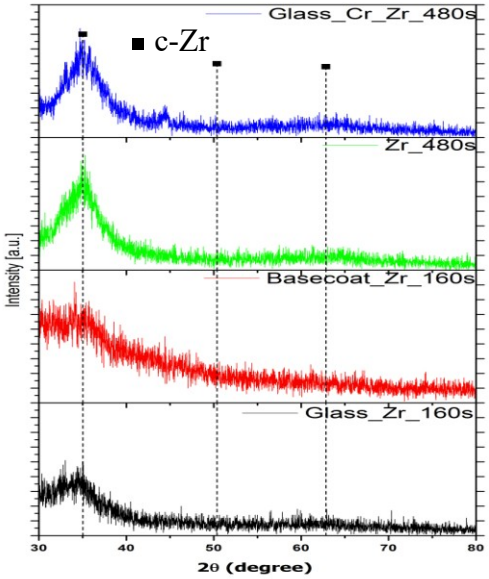

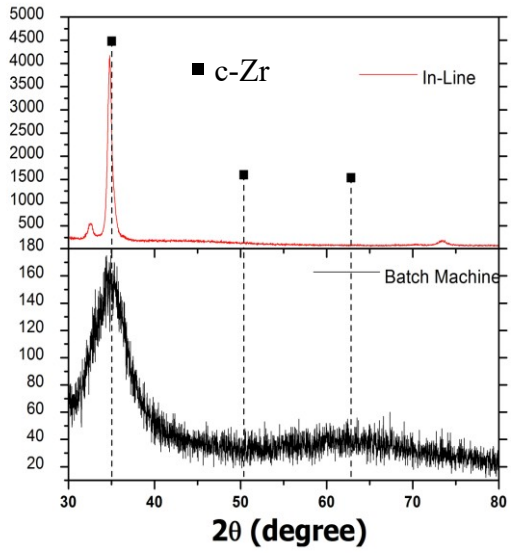

Influence of the substrate on the Zr phase (left). Right: Difference in Texture/phase between the In-line and Batch machine (right)

APPENDIX 5: XRD STRESS PLOTS RESULTS

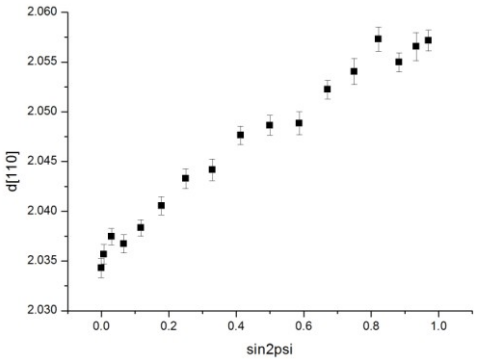

Sin2ψ plot of Cr_5A_152s

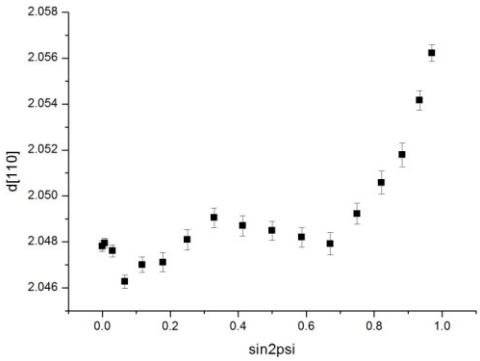

Sin2ψ plot of Cr_5A_456s

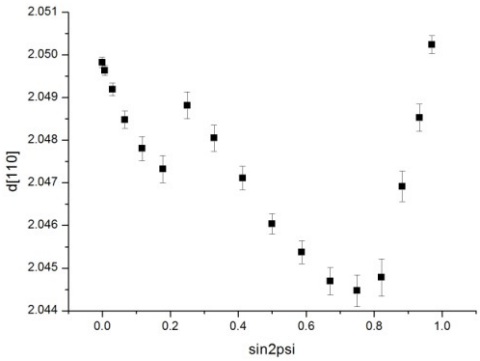

Sin2ψ plot of Cr_5A_760

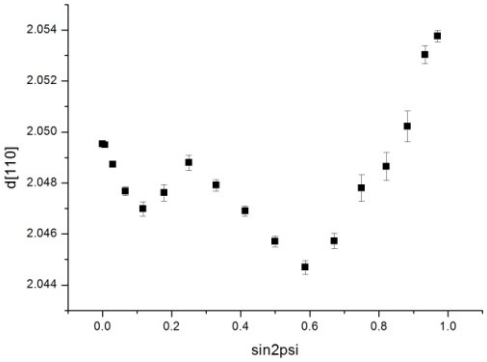

Sin2ψ plot of Cr_5A_1216

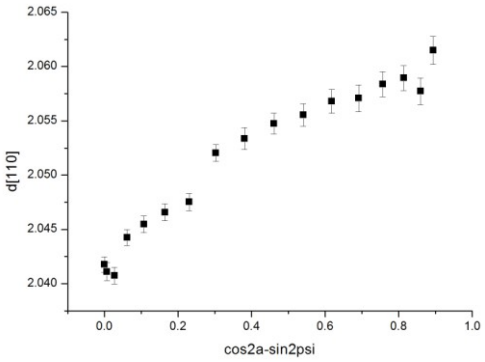

Cos2αSin2ψ plot of Cr_5A_76s

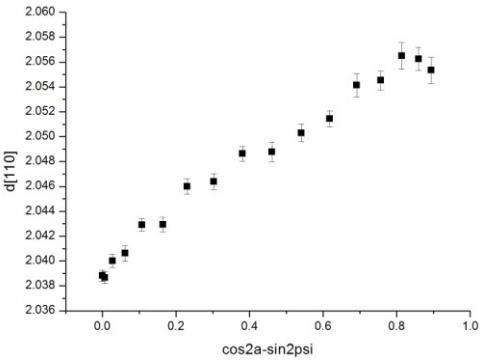

Cos2αSin2ψ plot of Cr_5A_152s

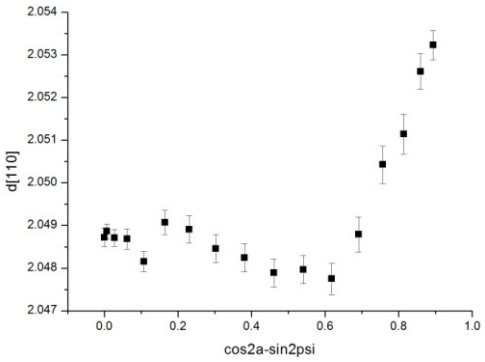

Cos2αSin2ψ plot of Cr_5A_456s

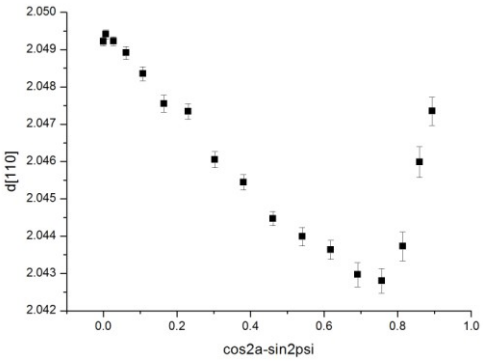

Cos2αSin2ψ plot of Cr_5A_760s

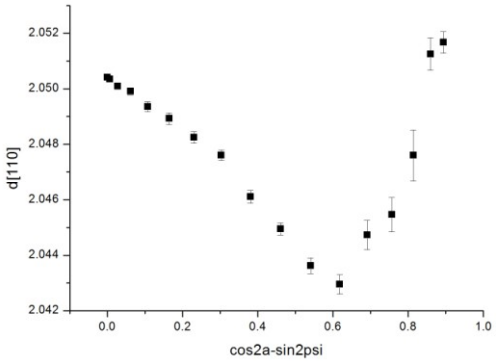

Cos2αSin2ψ plot of Cr_5A_1216s

APPENDIX 6: DEPENDENCY OF CURVATURE RADIUS ON THE FILM THICKNESS